

ANALYSING THE MOTION OF SOLAR WIND
TRANSIENTS USING STEREO/HI
OBSERVATIONS

Thesis submitted for the degree of

Doctor of Philosophy

at the University of Leicester

by

Anthony Owen Williams MSci (Hons)

Radio and Space Plasma Physics Group

Department of Physics and Astronomy

University of Leicester

February 2012

Abstract

This thesis examines a technique used to study solar wind transients with the STEREO heliospheric imagers. We perform a manual extraction of profiles of transient events from elongation-time plots and apply this technique to the profiles. The technique assumes we are studying a point like object travelling at a constant speed and extracts the speed of the object and the direction it is travelling relative to the observer. We first examine the errors involved in performing the manual extraction of the profiles and from this conclude that any errors introduced are small and can easily be taken into account.

Having examined the errors we then apply the technique to the two types of transient events, corotating interaction regions and coronal mass ejections. Corotating interaction regions have a spiral form and as such this technique should not work in determining their speed and position. However observations show that corotating interaction regions are made up of smaller scale transients which can be tracked. We were able to use this technique combined with in-situ measurements to track corotating interaction regions throughout the inner solar system.

Coronal mass ejections are generally larger one-off events which can be more easily analysed by this technique. We examine several coronal mass ejections with the technique and confirm the measurements of speed and direction with in-situ measurements at Earth. We then discuss the assumptions involved in the technique and how they might affect the STEREO observations. We conclude that this technique can be used to track all types of solar wind transients and that future work should focus on further assessment of the assumptions.

Declarations

The research undertaken during the course of this doctoral programme has led to the submission and publication of the following scientific papers:

Williams, A. O., J.A. Davies, S.E. Milan, A.P. Rouillard, C.J. Davis, C.H. Perry, and R.A. Harrison (2009), Deriving solar transient characteristics from single spacecraft STEREO/HI elongation variations: a theoretical assessment of the technique, *Annales Geophysicae*, 27, 4359-4368.

Williams, A.O., N.J.T. Edberg, S.E. Milan, M. Lester, M. Fränz, and J.A. Davies (2011), Tracking corotating interaction regions from the Sun through to the orbit of Mars using ACE, MEX, VEX, and STEREO, *Journal of Geophysical Research*, 116, A08103, doi:10.1029/2010JA015719.

Williams, A.O., S.E. Milan, and J.A. Davies (2012), Examining the evolution of transient solar wind structures using STEREO/HI, *Solar Physics*, submitted.

Acknowledgements

I would like to thank my supervisors, Professor Steve Milan and Doctor Jackie Davies, for all their help and advice over the course of my PhD. I would also like to thank everyone in RSPP for their help, advice and the morning crossword. I acknowledge STFC for funding my PhD.

I would also like to thank my friends, especially those I've made at gamesoc and more especially Ash Cox, for all the fun I've had in a Leicester. Finally I would like to thank Ashley Dodsworth for her support especially while I've been writing up.

Contents

Abstract.....	1
Declarations.....	2
Acknowledgements	3
1. Introduction	6
1.1. Motivation.....	6
1.2. Magnetism and Plasma Physics	8
1.3. The Sun	19
1.4. The solar wind.....	32
1.5. Summary	44
2. Literature Review	45
2.1. Corotating Interaction Regions	45
2.2. Coronal Mass Ejections.....	53
3. Instrumentation	64
3.1. The STEREO mission	64
3.2. Summary	90
4. Deriving solar transient characteristics from single spacecraft STEREO/HI elongation variations: a theoretical assessment of the technique.....	91
4.1. Introduction	91
4.2. Observations.....	99
4.3. Analysis of the 12 July 2007 CME	105

4.4.	Monte-Carlo simulations.....	111
4.5.	Discussion	116
4.6.	Conclusions	119
5.	Tracking corotating interaction regions from the Sun through to the orbit of Mars using ACE, MEX, VEX and STEREO	121
5.1.	Introduction	121
5.2.	The ACE, VEX and MEX instruments	122
5.3.	Method	123
5.4.	Observations.....	129
5.5.	Discussion	139
5.6.	Conclusion.....	141
6.	Examining the radial motion of transient solar wind events using STEREO/HI	143
6.1.	Introduction	143
6.2.	Method	146
6.3.	Observations.....	148
6.4.	Discussion	159
6.5.	Conclusions	162
7.	Conclusions and Future Work	163
	Bibliography	167

1. Introduction

1.1. Motivation

The Sun has long fascinated humans, from when it was worshipped as a God by ancient civilisations to its more recent worship by people looking to get a tan. The ancient civilisations recognised the Sun as the giver of life, which led to its worship and to sacrifices in the name of various gods for good harvests and other boons. As time and human understanding progressed we came to realise how sunlight interacted with various parts of our planet, from photosynthesis in plants to production of vitamin D in humans and animals. In addition we started to realise that the Sun was a lot more than just a yellow orb in the sky; the invention of the telescope in 1608 was swiftly followed by the first recorded numbers of sunspots, and various eclipses allowed the first coronal observations and the realisation that the Sun emitted more than just light.

Sunspots were recorded for a long time but it wasn't until 1859 that the link between solar activity and geomagnetic activity was made. Several flares were observed by Carrington on the Sun and a few hours after the largest flare was observed the largest geomagnetic storm on record was observed in ground-based magnetometers. This storm started further study in understanding the aurora and the solar-terrestrial connection, which has now evolved into solar-terrestrial physics and space weather studies.

In 1930 Lyot invented the coronagraph to allow observations of the solar corona at times other than eclipse. This was a big step forward, though there are still problems observing from Earth due to the scattering of light in the atmosphere. Various steps over the years have made improvements to the original design in an effort to remove, as

much as possible, the stray light produced by the atmosphere. Despite this, the biggest improvement was to get out of the atmosphere and put a coronagraph on a spacecraft.

The first attempt at putting a coronagraph on a spacecraft was in 1965 on the Solar Observatory 2 mission. This was one of a series of 8 Earth-orbiting spacecraft launched by NASA, designed primarily to observe a complete solar cycle in ultraviolet and X-ray light. The missions observed many phenomena such as coronal holes, solar flares in several wavelengths, and sunspots. Since then many spacecraft have launched with coronagraphs and other solar observing experiments. In that time we have learned much about the solar corona but until recently have never been able to observe coronal material heading directly towards Earth as spacecraft have previously stayed near to the Sun-Earth line.

The launch of the Solar TERrestrial RELations Observatory (STEREO) in 2006, into an orbit taking it away from the Sun-Earth line, allowed observation of coronal material as it moves towards the Earth. The STEREO spacecraft carries two Heliospheric Imagers (HI) which allow the imaging of coronal material throughout the inner heliosphere. Using these imagers we can study the evolution of the consequences of coronal events, such as the one seen by Carrington in 1859, as they travel from the Sun towards the Earth and other planetary bodies. The main aim of this thesis is to utilise the STEREO HI observations to gain a further understanding of solar wind transients and their evolution as they travel through the inner heliosphere and test our predictive capabilities.

In this introduction we summarise magnetism and basic space plasma physics in section 1.2, the Sun in section 1.3 and the solar wind in section 1.4.

1.2. Magnetism and Plasma Physics

The solar magnetic field is the driving force behind much of the solar activity we observe, from sunspots to coronal holes, coronal mass ejections and more. To fully understand the nature of solar magnetism and the associated plasma behaviour we should first summarise basic plasma physics. A plasma comprises charged particles which respond to electromagnetic forces and so we start with Maxwell's equations.

$$\operatorname{div} \mathbf{E} = \frac{\rho_q}{\epsilon_0} \quad 1.1.$$

$$\operatorname{div} \mathbf{B} = 0 \quad 1.2.$$

$$\operatorname{curl} \mathbf{E} = -\frac{\partial \mathbf{B}}{\partial t} \quad 1.3.$$

$$\operatorname{curl} \mathbf{B} = \mu_0 \mathbf{j} + \mu_0 \epsilon_0 \frac{\partial \mathbf{E}}{\partial t} \quad 1.4.$$

Here \mathbf{E} is the electric field, ρ_q is the charge density, ϵ_0 is the permittivity of free space, \mathbf{B} is the magnetic field, μ_0 is permeability of free space and \mathbf{j} is the current density. In equation 1.4 we can ignore the second term on the right hand side for solar applications as $\partial \mathbf{E} / \partial t \cong 0$.

As plasmas consist of charged particles we should also include the equation governing the motion of a single charged particle within an electric and magnetic field. The motion will in effect be the sum of the effects from the electric force, $q\mathbf{E}$, and the magnetic force, $q(\mathbf{v} \times \mathbf{B})$, and is called the Lorentz force, where q is the charge of a particle.

$$m \frac{d\mathbf{v}}{dt} = q(\mathbf{E} + \mathbf{v} \times \mathbf{B}) \quad 1.5.$$

1.2.1. Plasma bulk quantities

We will also need an understanding of plasma physics and will be using Maxwell's equations in some of the following descriptions of relevant plasma behaviour. First we should have a useable definition of plasma, such as the following,

“A plasma is a quasineutral gas of charged and neutral particles which exhibits collective behaviour.” (Chen, 1974)

Collective behaviour refers to the nature of plasma to respond to both localised conditions and to influences from distant regions of the plasma. It is a direct result of the strong electromagnetic forces governing the motion of the individual charged particles which in turn generate their own electric and magnetic fields which change the motion of other particles.

To fully understand quasineutrality we must first discuss Debye shielding. Debye shielding is the process where a plasma confines an applied electric potential. If we consider a positively charged ball inserted into a plasma then it would swiftly become surrounded by nearby electrons such that the electric field would be negligible at a certain distance from the ball. The distance over which this shielding occurs is the Debye Length and is given in equation 1.6.(Chen, 1974)

$$\lambda_D = \left(\frac{\epsilon_0 k_B T_e}{n e^2} \right)^{1/2} \quad 1.6.$$

Here k_B is the Boltzmann constant, T_e is the electron temperature and n is the number density of the ions and electrons in the plasma. This tells us that as the density increases in the plasma the Debye length decreases as there are more particles able to shield the electric potential. It also tells us that as the temperature and hence energy of the particles increases the Debye length also increases because the more energetic particles are able to move away from the electric potential and therefore are less able to shield it.

Using the Debye length we are now able to define quasineutrality. If the dimensions of the plasma, L , are much larger than the Debye length then we have a plasma which is quasineutral. This means that we can take the plasma density $n \cong n_i \cong n_e$ where n_i and n_e are the number densities of ions and electrons respectively. If we now look at the number of particles, N_D , shielding a region in the Debye sphere, equation 1.7, then to obtain statistically valid shielding this number must be much greater than 1. This shielding then prevents large electric forces from being generated by either an external source or internal motions of individual particles thus retaining the overall neutrality of the plasma.

$$N_D = \frac{4}{3} n \pi \lambda_D^3 \quad 1.7.$$

There is one further condition for the plasmas we are studying which is not referred to in our quoted definition. That is the condition that particles in the plasma must not collide with neutral atoms so frequently that their motion is governed by hydrodynamic forces but instead are governed by electromagnetic forces. This is not a

general condition for plasmas but in the cases examined in this thesis neutral atoms are sufficiently rare that we can consider this condition to be valid.

We can describe a plasma as a fluid if we use its bulk parameters of density, bulk velocity and pressure. For simplicity we assume a two species plasma consisting of positively charged ions and electrons. Consider a volume $d\tau$ containing electrons and one species of ion such that there are N_i ions and N_e electrons, and the plasma is quasineutral so that these are approximately equal, then the j^{th} particle of each species have a velocity which we denote \mathbf{v}_{ij} and \mathbf{v}_{ej} respectively.

Using this we can state the mass density, ρ_i , of the ions (and similarly electrons) as in equation 1.8, where m_i is the mass of an individual ion.

$$\rho_i = \frac{m_i N_i}{d\tau} \text{ and } \rho_e = \frac{m_e N_e}{d\tau} \quad 1.8.$$

As we have a similar equation for the electrons we can simply add the ion and electron mass density to obtain the overall mass density equation 1.9.

$$\rho = \frac{m_i N_i + m_e N_e}{d\tau} = \rho_i + \rho_e \quad 1.9.$$

The average ion and electron velocities, \mathbf{V}_i and \mathbf{V}_e , called the bulk velocities can be simply calculated from the sum of all ions and electrons, as in equation 1.10.

$$\mathbf{V}_i = \frac{1}{N_i} \sum_{j=1}^{N_i} \mathbf{v}_{ij} \text{ and } \mathbf{V}_e = \frac{1}{N_e} \sum_{j=1}^{N_e} \mathbf{v}_{ej} \quad 1.10.$$

However in studies of the solar wind we are generally more concerned with the bulk velocity of the plasma as a whole for which we need to use the centre of mass given by the vector \mathbf{R} . To calculate the centre of mass we also need the position vector

of each individual particle, \mathbf{r}_{ij} for ions and \mathbf{r}_{ej} for electrons. The centre of mass is then given by equation 1.11.

$$\mathbf{R} = \frac{\sum_{j=1}^{N_i} m_i \mathbf{r}_{ij} + \sum_{j=1}^{N_e} m_e \mathbf{r}_{ej}}{\sum_{j=1}^{N_i} m_i + \sum_{j=1}^{N_e} m_e} \quad 1.11.$$

Clearly the denominator of equation 1.11 is the total mass of the plasma element and as such can be replaced by $\rho d\tau$ from equation 1.9. If we then differentiate equation 1.11 with respect to time we can obtain the velocity of the centre of mass.

$$\rho d\tau \mathbf{V} = m_i \sum_{j=1}^{N_i} \mathbf{v}_{ij} + m_e \sum_{j=1}^{N_e} \mathbf{v}_{ej} \quad 1.12.$$

If we substitute the average velocities of the particles from the equations in 1.10 into equation 1.12 and utilise the mass density of ions and electrons as in equation 1.8 we obtain our final bulk velocity.

$$\rho \mathbf{V} = \rho_i \mathbf{V}_i + \rho_e \mathbf{V}_e \quad 1.13.$$

There are two further bulk plasma properties of interest to us, temperature and kinetic pressure. For this we return to the velocity of individual particles, which can be expressed as the average velocity as in the equations in 1.10 with the addition of a random perturbation, \mathbf{u}_{ij} and \mathbf{u}_{ej} . By definition the average of these random perturbations must be 0 but the average of the squared values will be non-zero. These random perturbations about the mean represent the thermal energy of the ions and electrons, which can be expressed as ion and electron temperatures. As with a gas the average kinetic energy of the particles will be $\frac{3}{2}k_B T$ and so we can obtain an expression for the ion temperature, equation 1.15, and similarly for the electron temperature.

$$\frac{3}{2}k_B T_i = \frac{1}{N_i} \sum_{j=1}^{N_i} \frac{1}{2} m_i \mathbf{u}_{ij}^2 \quad \text{and} \quad \frac{3}{2}k_B T_e = \frac{1}{N_e} \sum_{j=1}^{N_e} \frac{1}{2} m_e \mathbf{u}_{ej}^2 \quad 1.14.$$

Associated with these temperatures we have the partial pressures for ions, shown in equation 1.15, again similarly for electrons and the total pressure is the sum of the two partial pressures as shown in equation 1.16.

$$p_i = n_i k_B T_i \quad \text{and} \quad p_e = n_e k_B T_e \quad 1.15.$$

$$p = p_i + p_e \quad 1.16.$$

1.2.2. The continuity equation and the equation of motion

Here we consider the equations that govern the bulk motions and properties of a collisionless plasma. The continuity equation describes the conservation of mass of a plasma and the derivation is shown here. We first consider a volume in space, V , with surface S , with no source of plasma but which allows particles to move freely in or out of it. If we consider only the ions (the electron derivation is identical) and use the number density, n_i , and bulk velocity, \mathbf{V}_i , we have previously used then we can state the total number of ions within the volume at any given time as:

$$N_i = \int_V n_i \, d\tau \Rightarrow \frac{\partial N_i}{\partial t} = \int_V \frac{\partial n_i}{\partial t} \, d\tau \quad 1.17.$$

If we consider the movement of the ions across the surface of the volume, an element of which is denoted by $d\mathbf{s}$, then we obtain the flux integral in equation 1.18.

$$F = \oint_S n_i \mathbf{V}_i \cdot d\mathbf{s} \quad 1.18.$$

Equation 1.18 is positive if the ions are flowing out of the volume. As we have already stated that no new ions are created within the volume then equation 1.18 must equal the rate of decrease of the number of ions in the volume. Combining this with equation 1.17 and using the divergence theorem gives equation 1.19

$$\int_V \frac{\partial n_i}{\partial t} d\tau = - \oint_S n_i \mathbf{V}_i \cdot d\mathbf{s} = - \int_V \nabla \cdot (n_i \mathbf{V}_i) d\tau \quad 1.19.$$

As we are using an arbitrary volume we can remove the integral signs. If we then multiply by the ion mass, m_i , we obtain the ion mass continuity equation, 1.20.

$$\frac{\partial \rho_i}{\partial t} + \text{div} (\rho_i \mathbf{V}_i) = 0 \quad 1.20.$$

A similar equation is true for electrons and if we add these two equations together we obtain the total mass continuity equation, 1.21, with ρ as the total mass density and \mathbf{V} as the bulk velocity.

$$\frac{\partial \rho}{\partial t} + \text{div} (\rho \mathbf{V}) = 0 \quad 1.21.$$

Using Newton's second law we can consider the equation of motion for a plasma. If we use the electromagnetic, gravitational, pressure and collision forces then we can write for ions:

$$m_i n_i \frac{d\mathbf{V}_i}{dt} = en_i (\mathbf{E} + \mathbf{V}_i \times \mathbf{B}) - \nabla p_i + m_i n_i \mathbf{g} + \mathbf{P}_{ie} \quad 1.22.$$

Here \mathbf{P}_{ie} is the collision term for ions impacting with electrons and as we consider a collisionless plasma for the solar corona can be ignored. We can write a similar equation for electrons and add the two together to obtain equation 1.23:

$$n \frac{d}{dt} (m_i \mathbf{V}_i + m_e \mathbf{V}_e) = en(\mathbf{E} + (\mathbf{V}_i - \mathbf{V}_e) \times \mathbf{B}) - \nabla p + n(m_i + m_e)\mathbf{g} \quad 1.23.$$

Here we have used the approximation that $n \cong n_i \cong n_e$. Simplifying this further using equation 1.8 and substituting in for the current density, \mathbf{j} , we get equation 1.24.

$$\rho \frac{d\mathbf{V}}{dt} = \rho \mathbf{E} + \mathbf{j} \times \mathbf{B} - \nabla p + \rho \mathbf{g} \quad 1.24.$$

This equation shows us the forces acting on a plasma. The $\mathbf{j} \times \mathbf{B}$ term is the force on the plasma from the movement of the ions and electrons in a magnetic field. As we have already shown that electric fields are shielded out quickly in a plasma we can clearly see that the $\rho \mathbf{E}$ term is much smaller than the $\mathbf{j} \times \mathbf{B}$ term and so for practical purposes can be neglected, which we do from now on.

Using equation 1.24 we can find some measure of the equilibrium state of plasma. If we first neglect the gravitational force and consider the steady state of equation 1.24, that is $\partial/\partial t = 0$ then we obtain:

$$\nabla p = \mathbf{j} \times \mathbf{B} \quad 1.25.$$

This tells us that there is a pressure balance between the kinetic temperature and the Lorentz force and if we substitute equation 1.4 assuming $\frac{\partial \mathbf{E}}{\partial t} = 0$ into equation 1.25 then we get equation 1.26.

$$\nabla p = \frac{1}{\mu_0} (\text{curl } \mathbf{B}) \times \mathbf{B} = \frac{1}{\mu_0} \left[(\mathbf{B} \cdot \nabla) \mathbf{B} - \frac{1}{2} \nabla B^2 \right] \quad 1.26.$$

This gives us an expression for the magnetic field pressure and magnetic tension forces. The $\nabla \frac{B^2}{2\mu_0}$ term is the force due to the gradients in the pressure, $\frac{B^2}{2\mu_0}$, on the plasma from the magnetic field and is the dominant force in solar plasma physics. The $\frac{1}{\mu_0} (\mathbf{B} \cdot \nabla) \mathbf{B}$ term is the stress associated with tension from the magnetic field lines. This term is normally very small as it is linked to the curvature of the field lines which for most coronal physics is very low. However in areas of the solar atmosphere it can be very large.

1.2.3. Hydromagnetic equilibrium and plasma β

As we have already stated the magnetic tension term in equation 1.26 can be neglected in most circumstances and so we can take the ratio of the particle pressure, ∇p , and the magnetic pressure. This enables us to quantify the relative contributions of the plasma and magnetic field pressures. This ratio is called the plasma β and is shown in equation 1.27.

$$\beta = \frac{p}{B^2/2\mu_0} = \frac{\text{particle pressure}}{\text{magnetic field pressure}} \quad 1.27.$$

Most solar plasmas have a high value of beta, that is to say their motion is dominated by the particle pressure. Certainly in the corona, where temperatures are very high we can say that the particle pressure is dominant. However nearer the solar surface

the plasma is confined by the strong solar magnetic field and so the plasma beta here must be less than 1.

1.2.4. Frozen in flux approximation

Of particular interest to studies of the solar wind and its transients is the concept of frozen-in flux, or Alfvén's theorem, which we shall derive here. For this we require Ohm's law in the form presented in equation 1.28 where σ is the electric conductivity.

$$\mathbf{j} = \sigma(\mathbf{E} + \mathbf{V} \times \mathbf{B}) \quad 1.28.$$

If we now return to Maxwell's equations and substitute in expressions for \mathbf{j} and \mathbf{E} into equation 1.28, then we can obtain the induction equation, 1.29, where $\eta = 1/\sigma\mu_0$.

$$\frac{\partial \mathbf{B}}{\partial t} = \nabla \times (\mathbf{V} \times \mathbf{B}) - \nabla \times (\eta \nabla \times \mathbf{B}) \quad 1.29.$$

In this equation the first term on the right hand side describes the effect of the motion of the plasma on the magnetic field and the second term describes the decay of the field due to a finite electrical resistance. If we now use l as the characteristic length of the system and replace the curl operators with l/\mathbf{e} and also replace the vectors with their magnitudes we may compare the two terms on the right hand side of the equation and obtain the magnetic Reynolds number, equation 1.30.

$$R_m = \frac{Vl}{\eta} \quad 1.30.$$

In solar physics the value of R_m is often much greater than one and so we neglect the second term in equation 1.29. This simplified version of equation 1.29 is important in the concept of lines of flux being frozen in to plasma, although we must first add a little more to make this clear. If we consider a moving surface S and the flux through it as in equation 1.31:

$$\Phi(t) = \int_{S(t)} \mathbf{B}(\mathbf{r}, t) \cdot d\mathbf{A} \quad 1.31.$$

From this we can see that $\Phi(t)$ will change in time according to both the change of \mathbf{B} with time and the change of the surface S with time. Using our simplified version of equation 1.29 and substituting into the integral for the change of \mathbf{B} with time we obtain equation 1.32, where L is the boundary of S .

$$\int_S \frac{\partial \mathbf{B}}{\partial t} \cdot d\mathbf{A} = \int_S \nabla \times (\mathbf{v} \times \mathbf{B}) \cdot d\mathbf{A} = \int_L \mathbf{v} \times \mathbf{B} \cdot d\mathbf{l} \quad 1.32.$$

If we now consider the movement of the surface with velocity \mathbf{v} at a time of $t+dt$ then there is a possibility for a change in area which is given as $\mathbf{v}dt \times d\mathbf{l}$ and the flux through this area divided by dt is then given in equation 1.33.

$$-\int_L (d\mathbf{l} \times \mathbf{v}) \cdot \mathbf{B} = -\int_L d\mathbf{l} \cdot (\mathbf{v} \times \mathbf{B}) \quad 1.33.$$

This is clearly the negative of the result of equation 1.32. Therefore it is clear that the flux through any moving surface is constant providing we can neglect resistivity. From this we can go a step further and show that individual lines of force are dragged by the matter, that is to say individual lines of force can have their direction

changed and become twisted. First we consider a line of force, L , at a time t which is enclosed in a thin flux tube, at this instant the flux through any part of the surface of the flux tube is zero. Now we follow the plasma in this tube to a later time $t+dt$ and make the assumption that the magnetic field is no longer parallel to the tube of plasma, then in this instant the flux through the surface is non zero at some point along the tube. As we have just shown that the flux through the surface is conserved this cannot happen and so the field must be parallel to the plasma.

These results are important for the solar wind and the transient features studied in this thesis as they describe the nature of the magnetic field within the solar wind. The direction of the magnetic field of transient features and the solar wind has implications for the interaction of the solar wind with planetary magnetospheres.

1.3. The Sun

Over the years and using a variety of tools and methods we have been able to discern the internal structure of the Sun. We are primarily interested in coronal activity but as the Sun is the source of the corona we should have some understanding of the solar internal structure as well.

1.3.1. Internal Structure

At the centre of the Sun sits the core, where elements undergo nuclear fusion. The majority of the fusion processes occurring are hydrogen into helium although other heavier elements also undergo some fusion as they are produced. The fusion reaction from proton to proton collisions releases the majority of the energy at the core of the Sun. The proton-proton (p-p) chain produces approximately 98.8% of the Sun's energy while the majority of the remaining 1.2% is produced by the fusion of carbon, nitrogen and oxygen in the CNO cycle. In both the p-p chain and the CNO cycle the end product is helium nuclei and for each particle of helium produced approximately 26 MeV of energy is released (Stix, 1989).

From the core the energy is radiated out as gamma rays. However it does not take long before it is absorbed by surrounding material and re-radiated as x-rays or is scattered by an electron. The radiation after absorption can go in any direction and so some will be directed back towards the core, while some will progress further from the core towards the surface. Due to the density of the Sun, this process of absorption and scattering happens continuously with any given photon only travelling a few millimetres before encountering an obstacle. Despite the random nature of this process there is a net energy outflow through many small steps by photons. As the radiation progresses further outward, the solar material becomes cooler and so the wavelength of the photons gets longer, from gamma rays at the core to visible light nearer the surface. This inner region is known as the radiative zone and is the primary method of heat transport for the inner 70% of the Sun.

Outside of the radiative zone the primary method of heat transport becomes convection. This is due to a drop off in the density and temperature of the outer solar material which occurs because the pressure balance of thermal energy and gravity cannot support heavier particles. This creates a much larger temperature gradient than in the radiative zone and so as a hot parcel of material rises in the convective zone and begins to cool, it is still hotter than the surrounding material and so continues to rise. This does not occur in the radiative zone because once a hot parcel begins to rise, it cools quickly and soon reaches the same temperature as the surrounding material. In this outer region, known as the convective zone, heat transport occurs much more quickly, and eventually releases the energy at the outer edge of the Sun to the photosphere.

1.3.2. The photosphere

The photosphere is the visible surface of the Sun and where the energy generated deep in the core of the Sun is released into space and is where the surface is optically opaque. After the journey from the core to the surface the energy finally emerges with an average blackbody temperature of 5800 °K. As this layer sits on top of the convective zone the convective cells themselves become visible as granules on the photosphere. This granulation gives the photosphere the appearance of perpetually boiling. Looking more closely at granules, as in Figure 1.1, we can see that the centre of a granule is much brighter indicating warmer material and the edges are darker indicating cooler material falling back into the Sun.

Another phenomenon, also illustrated in Figure 1.1, is that of sunspots. The sunspot appears as a dark spot surrounded by striated marks. The dark spot in the middle is known as the umbra and is approximately 2000 °K cooler than the rest of the photosphere; the striations around it are the penumbra. Sunspots also possess a strong magnetic field which could explain why it is cooler than the surrounding photosphere. It is postulated that the stronger magnetic field suppresses convection below the sunspot and so there is less heat transported to the surface, thus reducing the temperature of the sunspot. Sunspots are a key indicator of solar magnetic activity as will be discussed below.

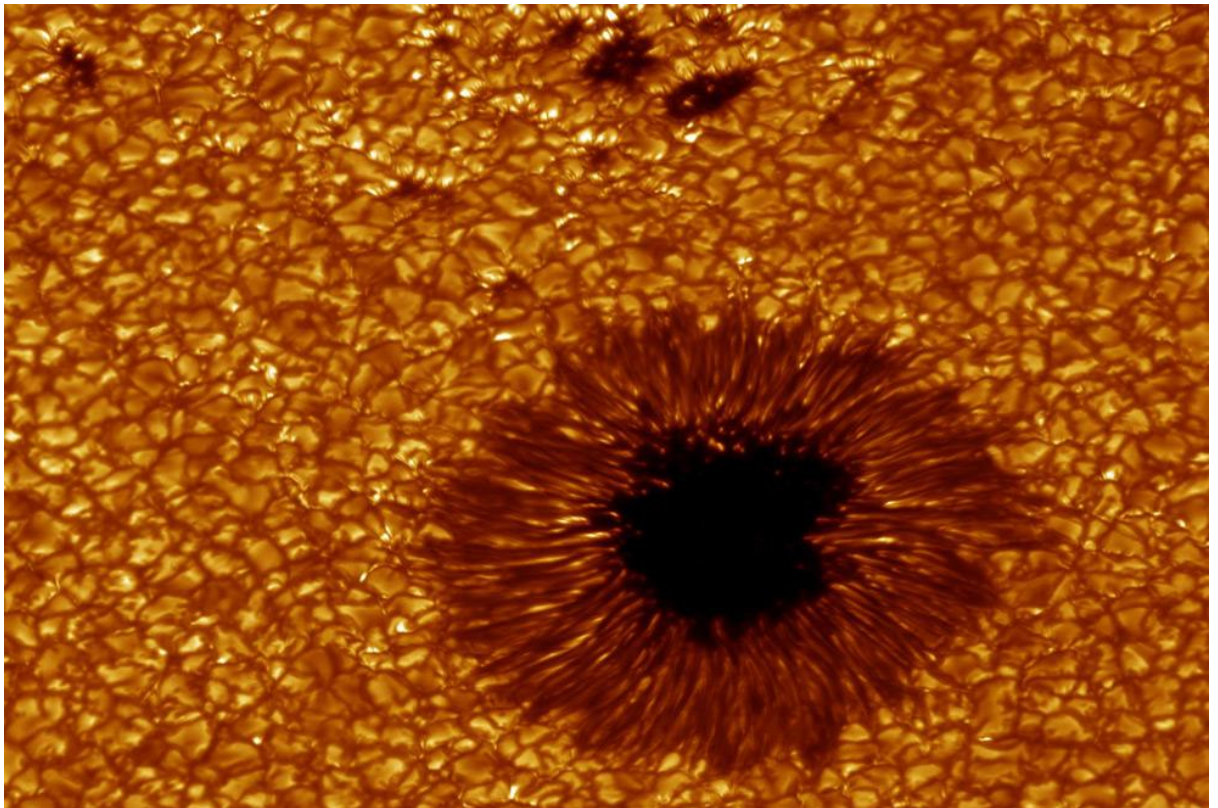


Figure 1.1: The photosphere as seen by the Swedish 1 m solar telescope operated by the Royal Swedish Academy of Sciences taken by Göran Scharmer and Kai Langhans of the Institute of Solar Physics. This image is from the 4th August 2003 and shows a sunspot along with the granulation of the photosphere.

1.3.3. The Chromosphere

The chromosphere could be considered as the start of the solar atmosphere and is a very narrow region extending to just a few thousand kilometres above the photosphere. The name comes from the colourful flashes which were observed during eclipses and the deep red colour in visible light. In this region, unlike below the surface, the temperature of the solar material begins to rise with increasing altitude ranging from 4500 °K to approximately 20,000 °K. This region is also home to a variety of visible phenomenon. The largest are known as prominences and the smallest as spicules.

Prominences are large arcs of solar material which can extend over large distances on the Sun and reach quite far, typically hundreds of thousands of kilometres above the solar surface. Here the material is held in place by the solar magnetic field allowing for a structure to remain stable for many hours or days at a time. While the overall structure may remain stable the prominence will appear to rain material down on to the surface of the Sun. An example of a prominence with the Earth superimposed for scale is shown in Figure 1.2.

Spicules are another phenomenon associated with the chromosphere and are small jet like bursts with a short lifetime of typically a few minutes. Spicules typically reach a height of about 5000 km above the surface of the Sun with a width of approximately 500 km. These spicules have a temperature of approximately 10^4 K and have been measured as moving upwards with a typical velocity of 25 km s^{-1} . The reason for this upward transport of material in spicules is currently unclear and the return flow of

material from spicules is also poorly understood. An example of a spicule is shown in Figure 1.3.

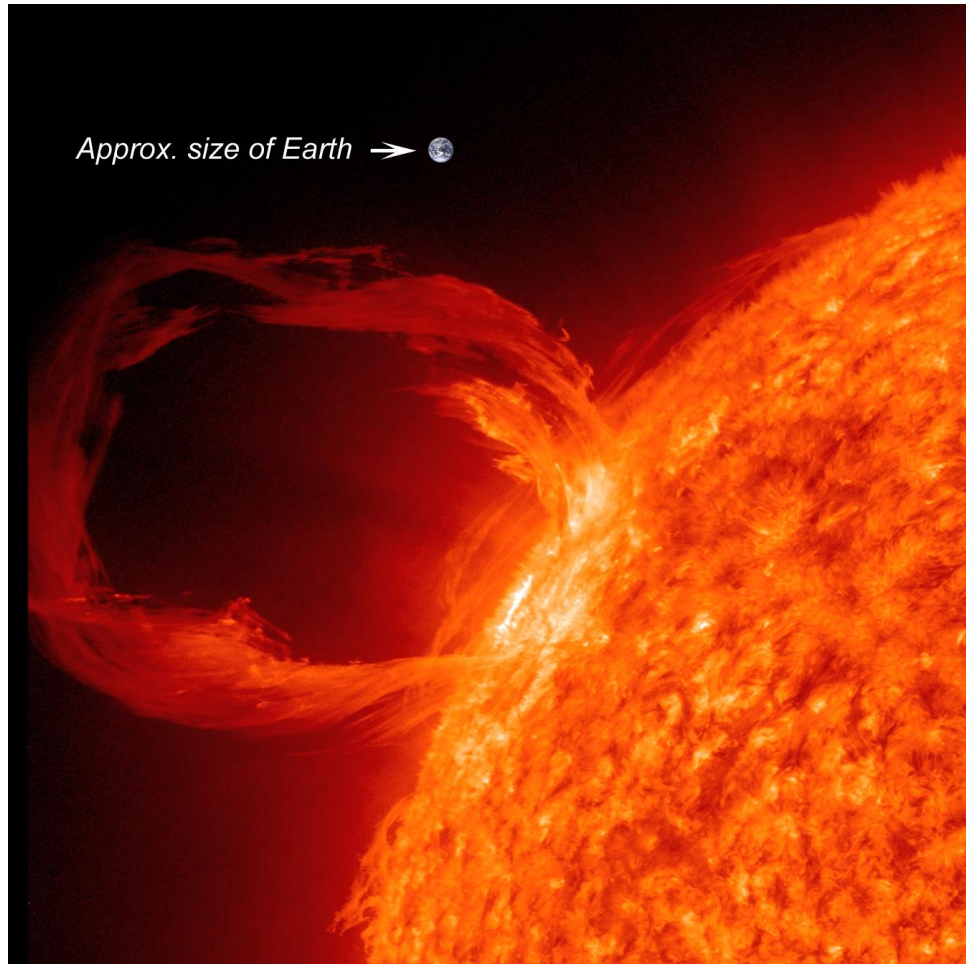


Figure 1.2: An erupting prominence above the surface of the Sun with the approximate size of the Earth shown for reference. (Credit: NASA SDO)

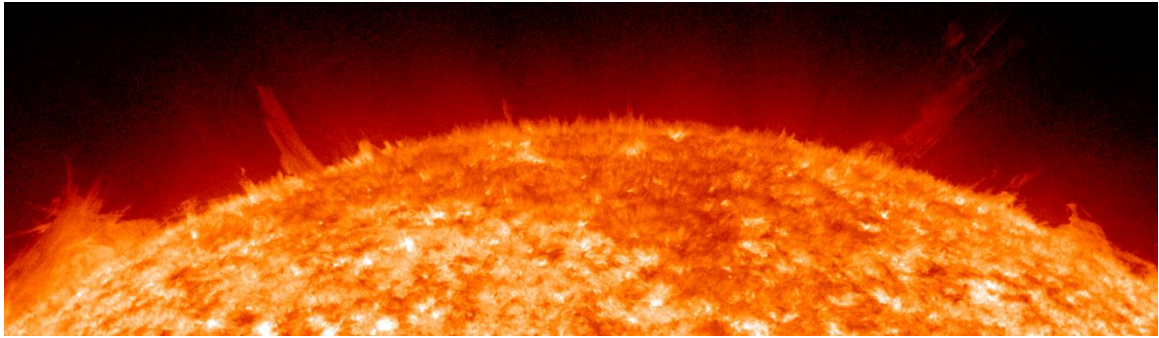


Figure 1.3: Spicules above the solar surface. (Credit: NASA SDO)

1.3.4. The Corona

The outermost layer of the solar atmosphere is the corona, which is separated from the chromosphere by a very narrow transition region. In the transition region the temperature increases by a factor of 100, although the height above the solar surface at which this happens is not constant and varies depending on local conditions. As the temperature begins to level out at approximately 10^6 K we move from the transition region to the solar corona. The exact reason for this increase in temperature of the corona is not yet clear.

The solar corona, as seen in white light observations, consists of two parts; the K corona and the F corona. The K corona is seen closer to the Sun and takes its name from the German “Kontinuum”. It is so called because it has a continuous spectrum similar to that of the photosphere but without Fraunhofer lines. This lack of clear absorption lines is due to the thermal broadening of the lines due to the very high temperatures in the corona, instead producing a broad dip in the spectrum in place of the expected dark lines. One further feature of the K corona is the highly polarised nature of the light observed. This polarisation indicates that the light is due to Thomson

scattering by free electrons. Thomson scattering plays an important role in STEREO/HI observations, as such it will be discussed in more detail later.

Further from the Sun, after two or three solar radii, the F corona dominates the white light observations of the corona. The F corona is so named after the Fraunhofer lines seen in its spectrum. Despite the very hot nature of the corona these lines are visible and are not affected by thermal broadening as the light is seen due to the scattering of sunlight from dust particles. Further, the continuous spectrum is again very similar to that of the photosphere and the light observed is weakly polarised. From this we can deduce that the light is scattered from dust particles.

The corona as a whole is much less visible than the photosphere and is normally only seen during eclipses or with the use of a coronagraph as detailed in section 1.1. This is due to the tenuous nature of the corona where the electron density at the base of the corona is approximately 10^9 cm^{-3} compared to 10^{17} cm^{-3} in the photosphere. In addition the density decreases with increasing distance from the Sun and so the intensity also decreases. The density and temperature variation through the chromosphere and into the lower corona is shown in Figure 1.4.

The corona is rather inhomogeneous and displays a great deal of activity and structure much like the layers below it. Much of this inhomogeneity is a result of the solar magnetic field and the plasma beta. The solar magnetic field is generated below the photosphere and penetrates upwards through the solar surface and in active regions. Here the flux is frozen into the plasma and as the plasma moves around the flux lines get twisted resulting in many of the phenomenon we see in the corona. A depiction of one model of the solar magnetic field in the corona for a quiet solar minimum scenario

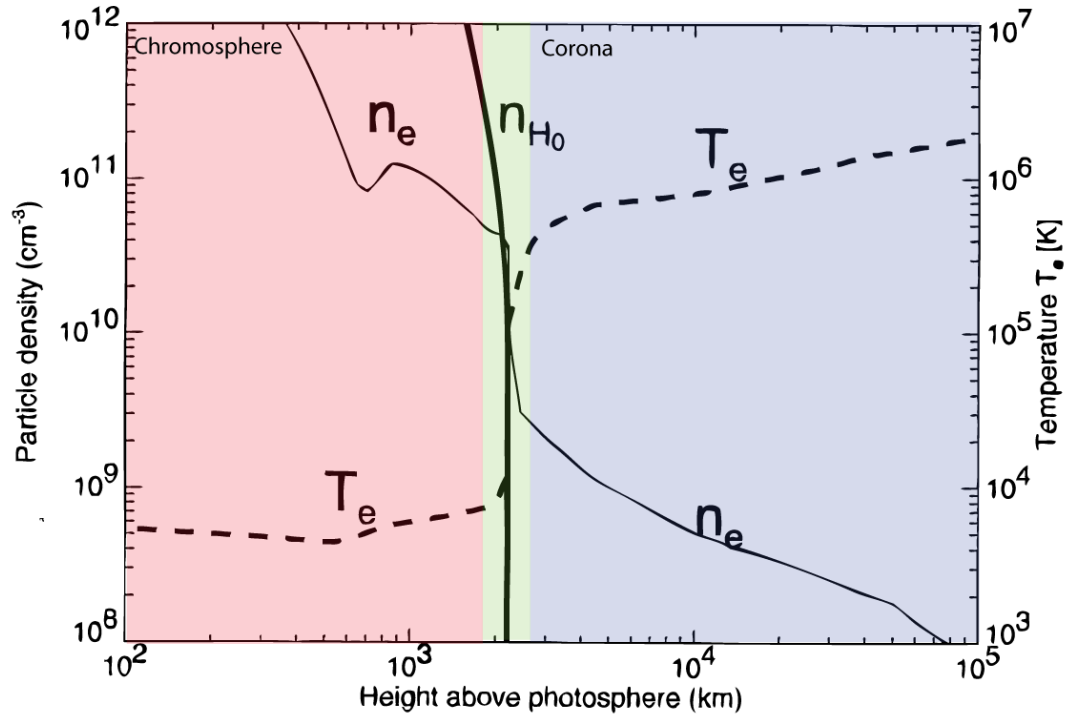


Figure 1.4: Electron density and temperature model of the chromosphere (Fontenla et al. 1990) and lower corona (Gabriel, 1976). Here, n_{H_0} indicates the neutral hydrogen density. Taken from “Physics of the Solar Corona”, Aschwanden, Figure 1.19. The coloured regions indicate different regions of the solar atmosphere. The green region is the transition region.

is shown in Figure 1.5. Figure 1.5 shows the lines of force in a multipole current sheet model. In the figure we can see the regions of closed field lines, shaded in grey, and theregions of open field lines around the main north and south magnetic poles. During other periods in the solar cycle the solar magnetic field is much more complex. The closed field lines shaded in grey are also generally associated with slow solar wind streams although the exact mechanisms which result in plasma escaping closed magnetic field lines are currently not well understood.

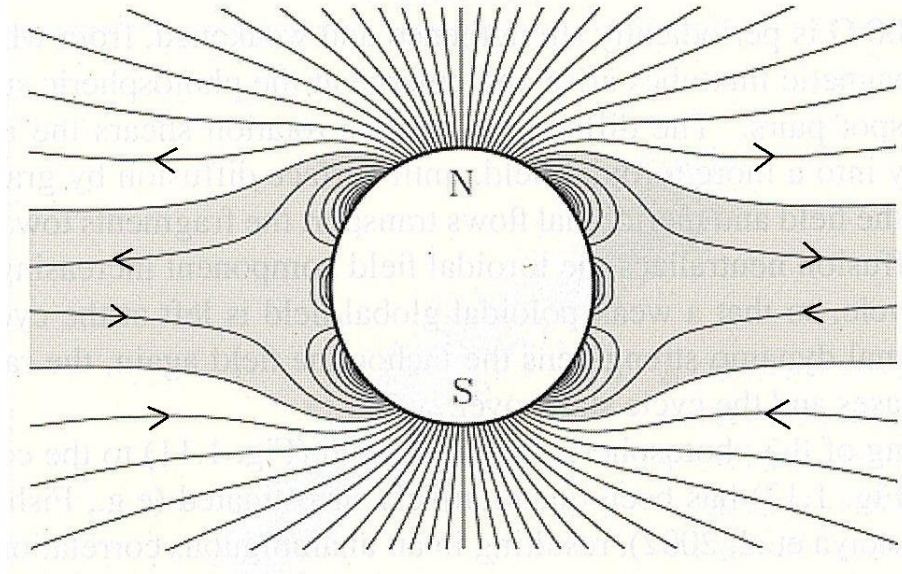


Figure 1.5: Depiction of the lines of magnetic force in the semi-empirical multipole-current sheet coronal model. Taken from Aschwanden (2005).

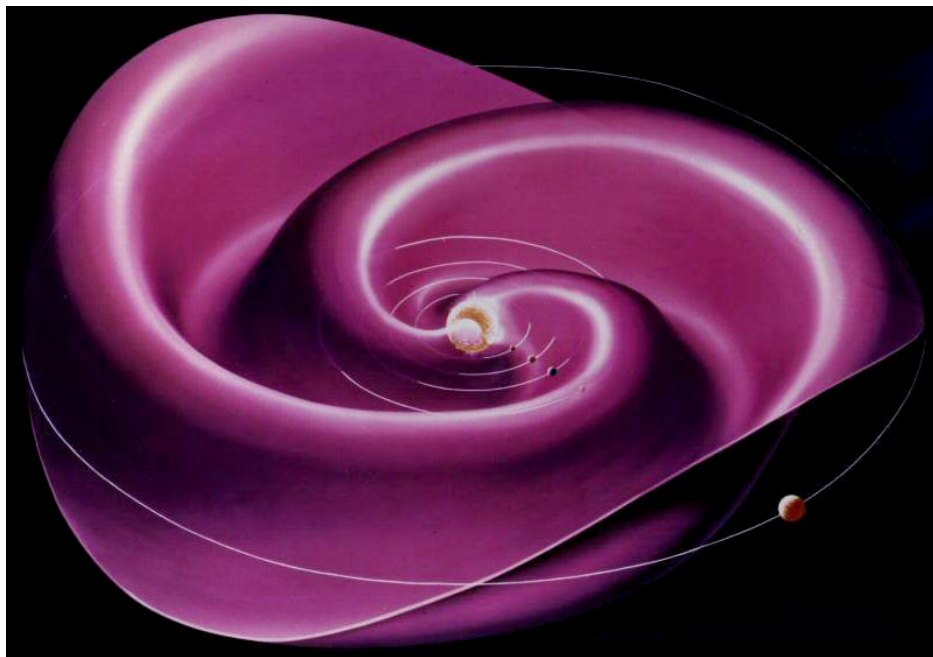


Figure 1.6: The form of the heliospheric current sheet (in purple) with the Sun at the centre of the image.

As we can see from Figure 1.5 there exists a region where magnetic field lines will have opposite polarities resulting in a current sheet known as the heliospheric current

sheet. Due to solar rotation and the offset of the solar magnetic and rotational axes the heliospheric current sheet becomes warped and results in the wave-like form seen in Figure 1.6.

One primary feature of the corona is the appearance of coronal holes. These coronal holes are visible as dark patches in the corona and which are normally confined to the polar regions of the Sun although at times they are visible at all latitudes. These coronal holes are dominated by open magnetic field lines which have one end rooted in the Sun and the other is transported by the solar wind into the heliosphere. Such open field lines allow coronal plasma to stream outwards to form fast solar wind streams. This results in coronal holes having a lower density than the surrounding corona and hence appearing darker. Although coronal holes are usually seen around the polar regions, at all stages of the solar cycle they are sometimes seen nearer the equator. However the mechanism which causes coronal holes to appear near the equator is not currently well understood. Coronal holes play a role in the formation of the corotating interaction regions and their role in that is discussed later (in section 2.1.1.).

1.3.5. The solar cycle

A full solar cycle lasts for approximately twenty-two years although this is normally split into two eleven year cycles. During a single eleven year cycle solar activity first rises and then falls and a good measure of this is the number of sunspots visible on the surface. By the end of each eleven year cycle the magnetic poles of the Sun have switched places and so after two complete eleven year cycles the Sun has returned to

the same magnetic state it started with and so the twenty-two year cycle is completed. The temporal variation of sunspot number for the most recent eleven year solar cycle is shown in Figure 1.7.

Most sunspots appear in pairs with one leading the other. These two spots will have opposing magnetic polarities and the order in which these appear will be the same for an entire eleven year cycle. This order will only be the case for one hemisphere and in the other hemisphere the order will be reversed. In the next solar cycle this order is then reversed. The solar cycle also has another effect on sunspots. Over the course of a solar cycle the latitudinal location of sunspots changes. Early in the cycle they appear at higher latitudes, around 30° - 35° , and move towards the equator as the cycle progresses. Both the change in magnetic polarity and the latitudinal migration of the sunspots is shown in Figure 1.8.

Coronal holes are also affected by the solar cycle. During the maximum of the cycle coronal holes are usually limited to the polar regions due to the strong fields penetrating the surface near sunspots. However at the minimum of the cycle coronal holes are more likely to be seen nearer the equator as the magnetic fields penetrating the surface are both weaker and fewer in number.

Cycle 23/24 Effective Smoothed Sunspot Number

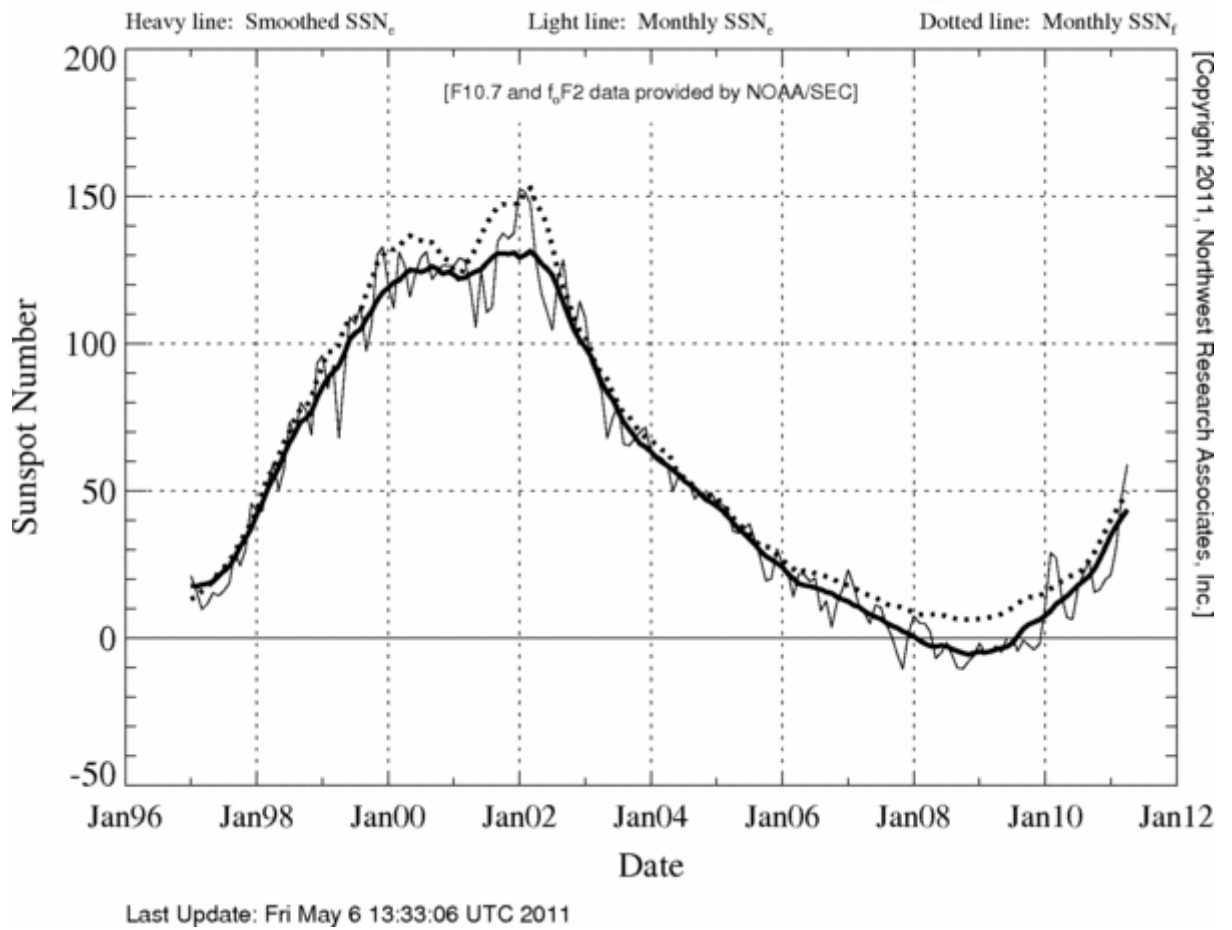


Figure 1.7: The sunspot number for the last solar cycle(23) and the beginning of the current solar cycle(24). The negative sunspot number is a result of using effective sunspot number based on radio fluxes rather than optical observations of sunspots. [Credit: Northwest Research Associates]

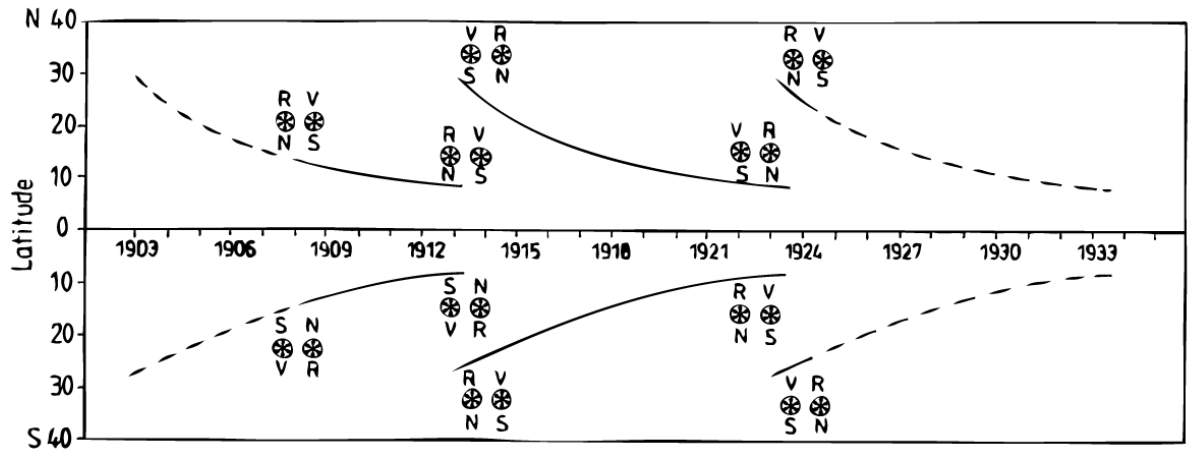


Figure 1.8: The “butterfly” diagram of sunspot polarity and latitudinal migration. N indicates northward polarity and S indicates southward polarity. The R and V indicate the red and violet colouring from the Zeeman triplet. The curves indicate the latitudinal movement of the sunspots. Taken from “The Sun: An introduction”, Stix, Fig 8.41.

1.4. The solar wind

We know that the solar atmosphere is dynamic and is constantly streaming out into space forming the solar wind. The cause of the formation of the solar wind was first suggested by Parker (1958). As we have already seen the high temperature of the corona produces a large outwards pressure gradient, sufficient to overcome the gravitational force and so particles are able to move away from the Sun. A mathematical derivation now follows. First we assume that the plasma of the solar atmosphere is completely neutral and that ions and electrons flow together. This allows us to state $\mathbf{V} = \mathbf{V}_e = \mathbf{V}_i$ and $n = n_e = n_i$ and so from this we can see there is no current flow. Using these assumptions we can then reduce the equation of motion, 1.24 to a simpler form, equation 1.34.

$$\rho \frac{d\mathbf{V}}{dt} = -\nabla p + \rho \mathbf{g} \quad 1.34.$$

As we are going to be considering an extended atmosphere where gravity will not be constant we should state that the acceleration due to gravity is given by:

$$\mathbf{g} = -\frac{GM_{\odot}}{r^2} \hat{\mathbf{r}} \quad 1.35.$$

Here G is the gravitational constant, M_{\odot} is the mass of the Sun, $\hat{\mathbf{r}}$ is the radial unit vector and r is the magnitude of the radial vector. If we assume the temperature is constant, the isothermal solution, and the same for ions and electrons from equations 1.15 and 1.16 we get the total pressure. We can also substitute the number density for the mass density and mean particle mass $\langle m \rangle$ and obtain equation 1.36.

$$p = \frac{\rho k_B T}{\langle m \rangle} \quad 1.36.$$

We now test to see if a hydrostatic solution of the solar atmosphere is possible such that the gravitational force downward is balanced by the pressure force upward. If this is the case the gravitational force falls with distance and so too must the pressure force, hence the mass density must also fall. So assuming that the atmosphere is in static equilibrium we have the conditions that $\frac{\partial}{\partial t} = 0$ and $\mathbf{V} = \mathbf{0}$. From this we can see that the continuity equation, 1.21, is satisfied and the equation of motion reduces to equation 1.37.

$$\nabla p = \rho \mathbf{g} \quad 1.37.$$

Assuming that the solar atmosphere is spherically symmetric we can write the pressure as $p = p(r)$ and so reduce the ∇p term to an ordinary differential. Substituting

this into equation 1.37 along with our expressions for gravity and mass density from equations 1.35 and 1.36 and finally integrating we obtain equation 1.38.

$$\int_{p_0}^{p(r)} \frac{dp}{p} = -\frac{GM_{\odot}\langle m \rangle}{k_B T} \int_{R_{\odot}}^r \frac{dr}{r^2}. \quad 1.38.$$

Here p_0 is the pressure at the surface of the Sun which has the radius R_{\odot} . This integral can then be solved with the given limits and rearranged to obtain an expression for $p(r)$, equation 1.39.

$$p(r) = p_0 \exp\left(-\frac{GM_{\odot}\langle m \rangle}{k_B T} \left[\frac{1}{R_{\odot}} - \frac{1}{r}\right]\right). \quad 1.39.$$

If we now look at the pressure as r goes to infinity we can neglect the $1/r$ term in equation 1.39 and calculate an approximate value for the pressure. Using the approximate values given in section 1.3.4 for the number density and temperature we can estimate p_0 to be approximately 0.0275 N m^{-2} and so from equation 1.42, $p_{\infty} \approx 8.3 \times 10^{-5} \text{ N m}^{-2}$. For hydrostatic equilibrium to be achieved we must balance this outward pressure with the pressure of the interstellar medium. This can be estimated in the same way as p_0 but with a number density of approximately 3 cm^{-3} and a temperature of 3000 K which gives a pressure of approximately $10^{-13} \text{ N m}^{-2}$. This is clearly much lower than the estimate of pressure from the Sun and so we can see that hydrostatic equilibrium is not valid.

Having shown that hydrostatic equilibrium is not valid we can now remove the assumption that $\mathbf{V} = \mathbf{0}$ and instead allow it to vary with altitude radially. For a spherical polar coordinate system with only a radial variation of a vector, \mathbf{A} , we can write the divergence of the vector as:

$$\nabla \cdot \mathbf{A} \equiv \frac{1}{r^2} \frac{\partial}{\partial r} (r^2 A) \quad 1.40.$$

Using this identity and the same time independence in the continuity equation, 1.21, we obtain the following equation 1.41.

$$\frac{\partial}{\partial r} (r^2 \rho V) = 0 \quad 1.41.$$

Hence we can see that the quantity $r^2 \rho V$ is constant where ρV represents mass flux across a surface of unit area. As we are considering a spherically symmetric system, the mass flow across a spherical shell at radius r is given by $4\pi r^2 \rho V$ which must be constant from equation 1.41. Therefore as the distance from the Sun increases the quantity ρV must decrease as $1/r^2$. If we now return to the equation of motion, equation 1.24, including the velocity term but once again dropping the $\mathbf{j} \times \mathbf{B}$ term we have equation 1.42.

$$\rho \frac{dV}{dt} = -\frac{GM_{\odot} \rho}{r^2} - \frac{dp}{dr} \quad 1.42.$$

Here though we are considering a time independent solution and so we must convert the d/dt term into a more useful term. To do so we consider a plasma parcel as it flows out from the Sun then we can convert dV/dt using the relation shown in equation 1.43.

$$\frac{dV}{dt} = \frac{V(r + dr) - V(r)}{dr/V} = V \frac{dV(r)}{dr} \quad 1.43.$$

Now substituting equation 1.36 and the relation in equation 1.43 into equation 1.42 then we can update the equation of motion.

$$V \frac{dV}{dr} = -\frac{GM_{\odot}}{r^2} - \frac{k_b T}{\langle m \rangle \rho} \frac{d\rho}{dr} \quad 1.44.$$

To solve this we need to use the continuity equation as in equation 1.41 to obtain an expression for $\frac{1}{\rho} \frac{d\rho}{dr}$ as shown in equation 1.45.

$$\frac{1}{\rho} \frac{d\rho}{dr} = -\left(\frac{2}{r} + \frac{1}{V} \frac{dV}{dr}\right) \quad 1.45.$$

Substituting this into equation 1.44 and rearranging finally gives us the equation which describes the change of solar wind velocity with radial distance from the Sun.

$$\frac{dV}{dr} = \frac{V \left(\frac{2k_B T}{\langle m \rangle} - \frac{GM_{\odot}}{r} \right)}{\left(V^2 - \frac{k_B T}{\langle m \rangle} \right)} \quad 1.46.$$

From here we can produce an analytical solution for the solar wind but first it is useful to examine some of the possible solutions through careful selection of starting points with respect to a critical value of r and V . The numerator of the right hand side of equation 1.46 will go to zero at $r=r_c$ given by:

$$r_c = \frac{GM_{\odot} \langle m \rangle}{2k_B T} \quad 1.47.$$

This indicates that for values of r less than r_c the gravitational term of the numerator dominates and so the plasma is gravitationally bound to the Sun. At values of r greater than r_c the pressure resulting from the high temperature of the corona tells us that gravity can no longer contain the plasma and so it is free to escape. In a similar manner there is a value of V for which the denominator of the right hand side of equation 1.46 goes to zero, which is also equal to the speed of sound in an isothermal gas, given by:

$$V_c = \sqrt{\frac{k_B T}{\langle m \rangle}} = C_s \quad 1.48.$$

For $V = C_s$, $dV/dr \rightarrow \infty$ except at $r = r_c$ and so we can use this to split the solution of equation 1.46 into 4 quadrants, split by the critical values of r and V . Now we can examine various possible solutions as shown in Figure 1.9.

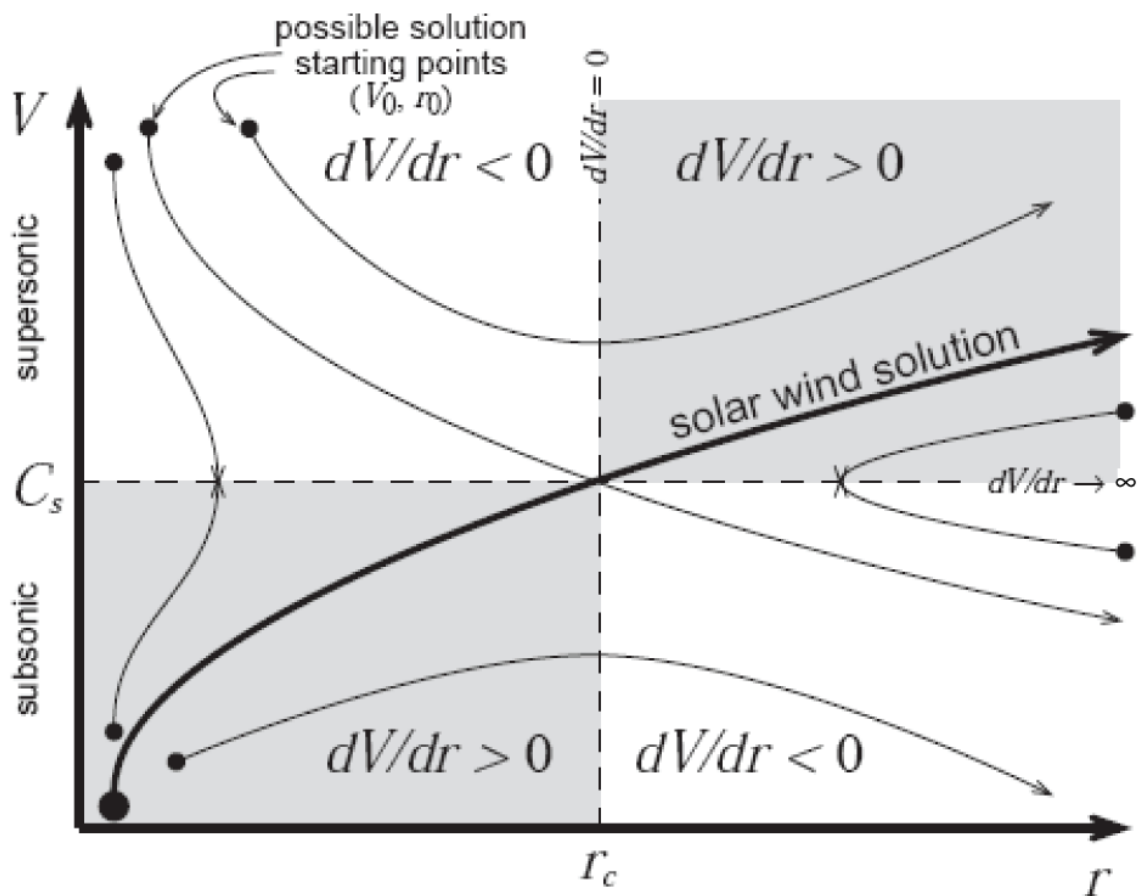


Figure 1.9: The possible solutions to the equation 1.49. The bold curve is the solar wind solution.

While there are several possible solutions to equation 1.46, the solution which satisfies the boundary conditions is shown as the bold line in Figure 1.9 which represents low initial velocities near the surface of the Sun growing to larger but still

finite solutions further from the Sun. It should be noted that the point at which r is larger than r_c is also the point at which the flow goes from being subsonic to supersonic.

To solve equation 1.46 analytically we separate the variables V and r and in doing so can substitute our expressions for r_c and C_s from equations 1.47 and 1.48 respectively. This leads to the integral in equation 1.49.

$$\int (V^2 - C_s^2) \frac{dV}{V} = \int 2C_s^2 \left(1 - \frac{r_c}{r}\right) \frac{dr}{r} \quad 1.49.$$

The solution to this integral is then:

$$\frac{1}{2}V^2 - C_s^2 \ln V = 2C_s^2 \left(\ln r + \frac{r_c}{r}\right) + K \quad 1.50.$$

Here K is the constant of integration which we can obtain by using the values known to us, that is at $r=r_c$, $V=C_s$.

$$K = -C_s^2 \left(\frac{3}{2} + \ln C_s + 2 \ln r_c\right) \quad 1.51.$$

This solution can then be substituted back into equation 1.50 to obtain the final isothermal solar wind solution.

$$\frac{V^2}{C_s^2} - 2 \ln \frac{V}{C_s} = 4 \ln \frac{r}{r_c} + 4 \frac{r}{r_c} - 3 \quad 1.52.$$

As both r_c and C_s are dependent on T so too is the solar wind velocity profile, as can be seen in Figure 1.10. We can also use this to make a statement about the density of the solar wind because we know from the continuity equation that ρV must fall with increasing r , we also know that V increases with r , hence we can say that ρ must fall rapidly.

This solar wind is the background against which we study larger transient events. As Figure 1.10 shows the solar wind speed is almost constant at 1 AU. We also expect the solar wind density at 1 AU to be small, and this is observed by spacecraft measurements.

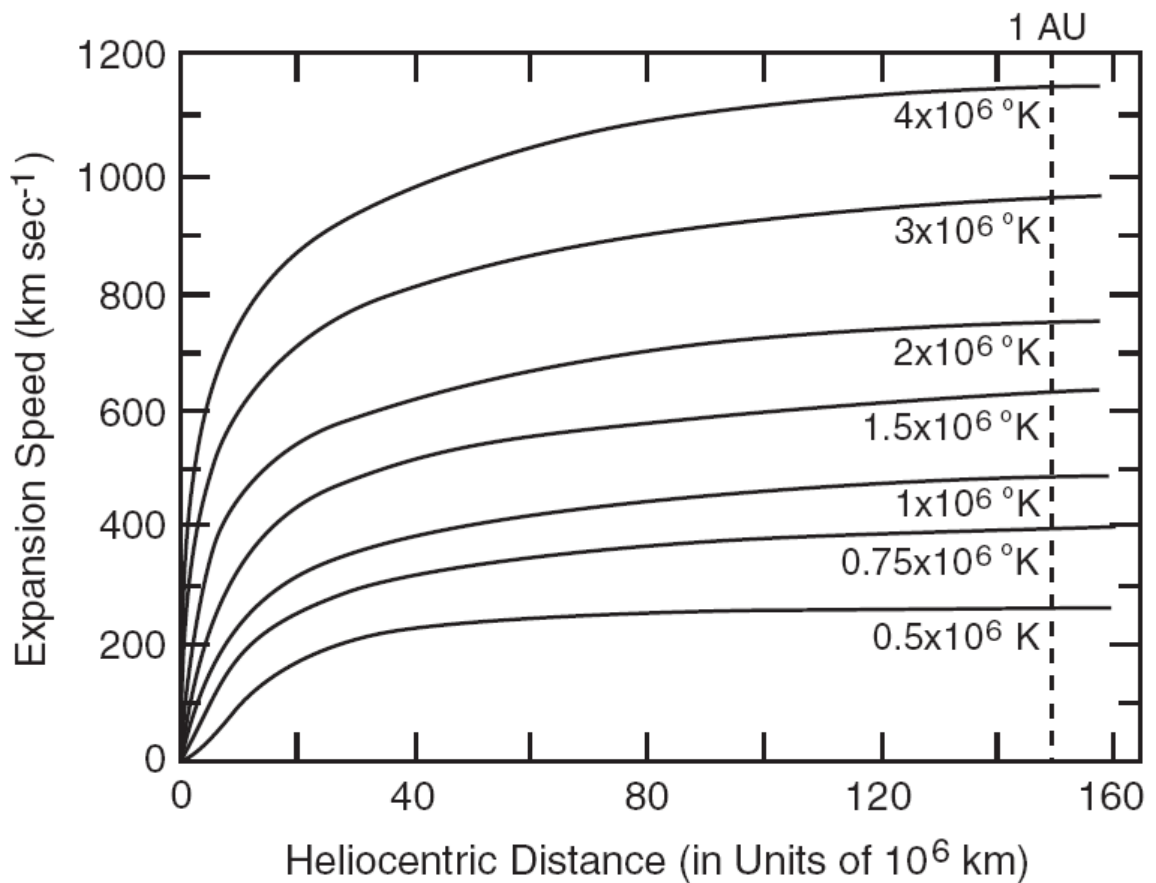


Figure 1.10: Theoretically derived speed of the solar wind from an isothermal model, assuming several coronal temperatures. Taken from “Solar wind and Interplanetary Magnetic Field: A Tutorial”, C.T. Russell, Space Weather monograph.

1.4.1. The interplanetary magnetic field

We know the Sun has a magnetic field and in the previous derivation of the solar wind this was neglected. We have also previously shown how magnetic field lines get frozen into solar coronal plasma. So it should be clear that the solar wind carries part of the solar magnetic field into the heliosphere and this is what is called the interplanetary magnetic field.

If there were no solar wind then the magnetic field of the Sun would be approximately dipolar at solar minimum. However we know there is a plasma outflow and that the magnetic field lines are frozen in to the plasma outflow so we can imagine our dipolar magnetic field lines becoming stretched out. After some time the outflow drags the field lines such that they point radially. This can be either towards or away from the Sun depending on the direction of the magnetic field at the solar surface. It is therefore clear that close to the magnetic equator the field lines will point in opposite directions resulting in a current sheet separating them as required by Ampère's Law.

There is one further process we must consider in our picture of the interplanetary magnetic field; that is the solar rotation. The Sun rotates approximately once every 25 days near the equator, although the rotation is variable with latitude. This rotation does not have an effect on the solar wind as the outflow is radial but the interplanetary magnetic field is frozen to the solar wind and also to the solar surface. Therefore as the Sun rotates and the solar wind plasma flows outward, the resulting magnetic field line becomes curved into a spiral. Figure 1.11 demonstrates this process.

Nearer the poles where the interplanetary magnetic field is already quite radial the solar wind has a less dramatic effect. Instead it is more likely the case that the plasma outflow will follow the field lines. A visual effect of this is the large coronal holes seen near the poles of the Sun which indicate the more open nature of the field lines and the rapid movement of plasma from the region. This high speed stream has been measured by the Ulysses spacecraft and is shown in Figure 1.12.

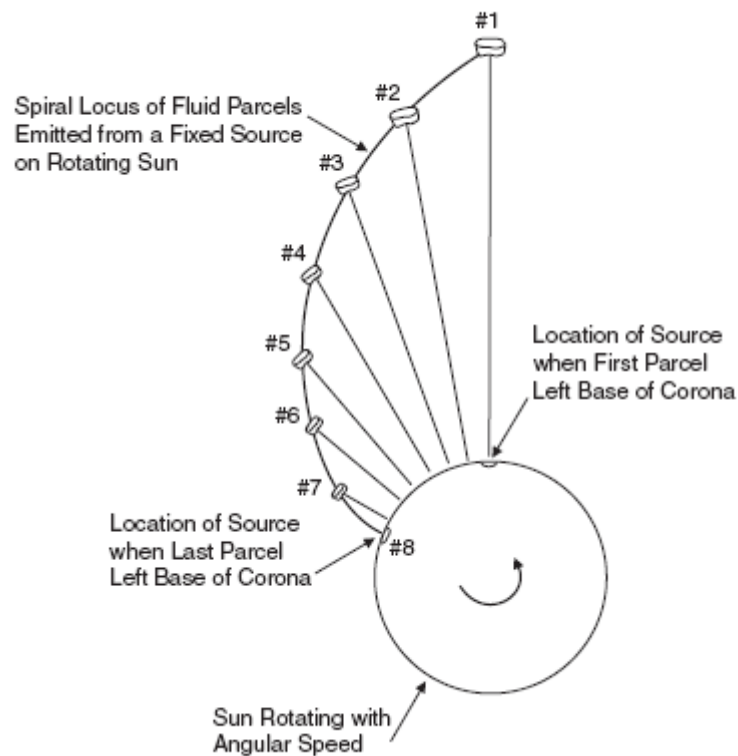


Figure 1.11: The creation of the spiral magnetic field pattern of the interplanetary magnetic field by the Sun. Taken from “Solar wind and Interplanetary Magnetic Field: A Tutorial”, C.T. Russell, Space Weather monograph.

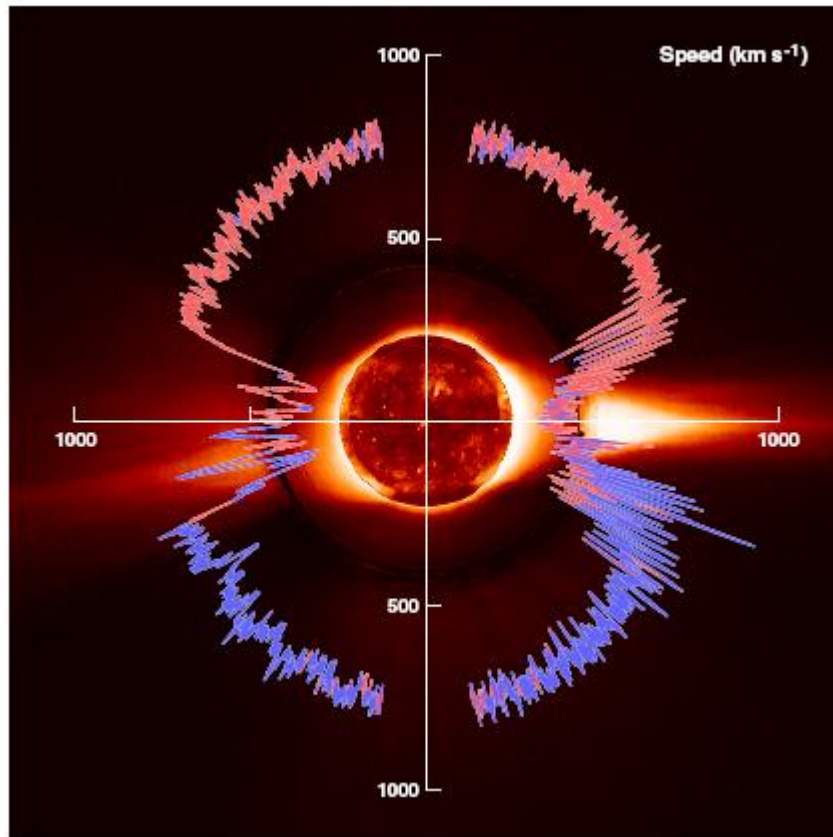


Figure 1.12: Ulysses observations of the solar wind speed and magnetic polarity as a function of solar latitude. The red and blue colouring indicates the direction of the magnetic field. Taken from “Solar wind and Interplanetary Magnetic Field: A Tutorial”, C.T. Russell, Space Weather monograph.

1.4.2. Solar wind transients

The solar wind is rarely quiet and there are frequent transient events in the form of coronal mass ejections (CMEs) and corotating interaction regions (CIRs). Both transient events will be discussed in more detail in the next chapter so here is only a brief description of the two types of events.

CIRs form when a high speed solar wind stream, from an equatorial coronal hole for example, follows a low speed solar wind stream as the Sun rotates. As the two streams move across the solar surface the plasma from the high speed stream cannot mix with the plasma from the low speed stream and so a compression is formed at the boundary resulting in a pile up of plasma and magnetic field lines. As a result CIRs follow the spiral of the solar wind interplanetary magnetic field and can also persist for several solar rotations depending on the longevity of the source regions.

CMEs are much more direct events typically following a more radial path and usually taking the appearance of a large arc although this is not necessarily the case for all CMEs. CMEs can occur at all times of the solar cycle but are much more frequent during solar maximum. Their formation is usually the result of a release of a build up of energy at the solar surface. This release can be a sudden event or a more gradual release and the reason for this difference in release is not yet clear. Once released the CME will travel outwards radially often at speeds higher than the background solar wind. A CME will usually have a much higher density than the solar wind and also have a strong distinct magnetic field, although there are many characteristics which can be used to identify a CME in in-situ observations. These characteristics will be discussed in more detail in the next chapter.

1.5. Summary

In summary the solar wind and solar wind transients, governed as they are by plasma physics, are an important feature of the active solar surface. The links between the deep interior, the surface and corona is complex and drives some fascinating features which are still not fully understood. The propagation of these features through the heliosphere and their interaction with planetary magnetospheres is still an area of intense research. The passage of the transients through the inner heliosphere towards Earth are studied in this thesis. More detail regarding CMEs and CIRs can be found in the next chapter.

2. Literature Review

The solar wind has two broad classes of transient events superimposed on the steady solar wind flow. These are Corotating Interaction Regions and Coronal Mass Ejections and they are seen to lesser and greater extents at different times of the solar cycle. This chapter will present the main characteristics and formation of these two disturbances.

2.1. Corotating Interaction Regions

Corotating interaction regions (CIRs) are extended regions consisting of a pile up of plasma and magnetic field which persist for a considerable time, normally multiple solar rotations. Here we will examine previous work on CIRs and look in greater detail at their formation and impact on planetary atmospheres.

2.1.1. Formation of a corotating interaction region

A CIR is formed from the collision of a high speed solar wind stream and a preceding slow solar wind stream. These streams come into contact as a result of the rotation of the Sun and near-radial outflow when the source regions for the flows are longitudinally separated (Pizzo, 1978). The basic picture of this in the equatorial plane is shown in Figure 2.1. This picture depicts a slow speed solar wind stream which will have its source in the corona. The high speed solar wind stream has its source in near

equatorial coronal holes (Hundhausen, 1972; Krieger, Timothy and Roelof, 1973) and as previously explained the open magnetic field lines indicate regions of quick outward streaming of coronal material.

The basic picture as shown in Figure 2.1 shows how the interaction of the fast and slow solar wind streams create a compression region as the two plasma streams and their associated magnetic fields are unable to mix due to the frozen in flux approximation. In this compression region both the solar wind density and pressure will increase as the material is forced together. Following this compressed region we see a rarefaction region where the fast flow is moving away from the trailing slow flow creating a reduction in solar wind density (Hundhausen, 1972; Parker, 1963; Gosling and Pizzo, 1999).

At larger radial distances the fast stream continues to impinge on the slow stream and eventually forms a pair of shocks, one in each stream(Lee, 2000). These shocks usually form at radial distances greater than 3 AU(Lee, 2000) and so are not regularly observed at Earth orbit.

STREAM INTERACTION SCHEMATIC
(INERTIAL FRAME)

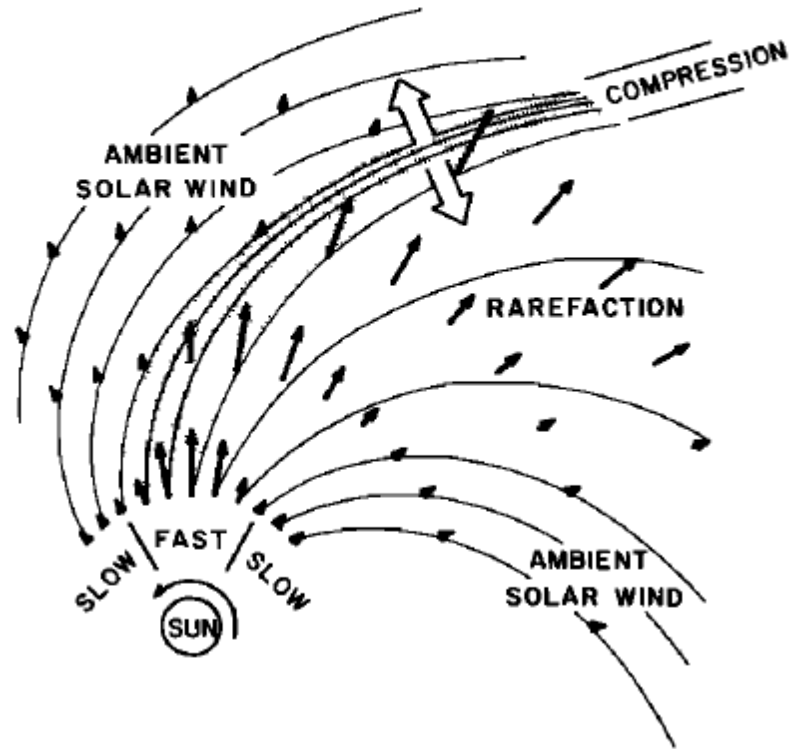


Figure 2.1: Schematic of the formation of a CIR in the ecliptic plane. The radial flows of the fast solar wind catch up with the slower solar wind preceding it and create a compression region. (Pizzo, 1978).

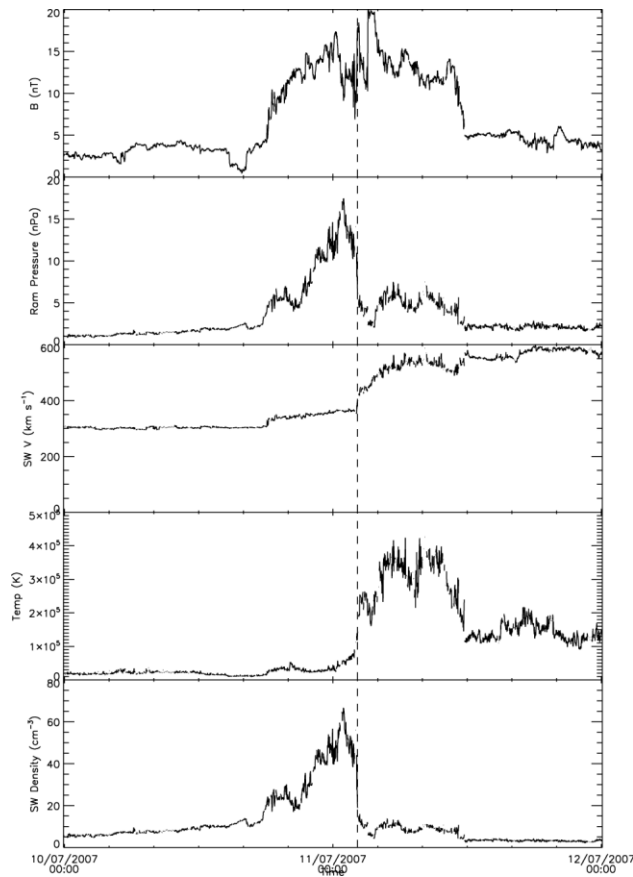


Figure 2.2: An example of a CIR from the ACE spacecraft. The plots (from top) show magnetic field magnitude, total ram pressure, bulk velocity, temperature and density. The vertical dashed line shows the interface between the CIR and the fast solar wind stream.

2.1.2. Observations of CIRs

Figure 2.2 shows an example of in situ observations of a CIR at 1 AU from the ACE spacecraft. From Figure 2.2 we can see that before the stream arrives at the spacecraft the pressure, density, speed and temperature are quite low and are what we would expect from a slow solar wind stream. The interaction region itself is best defined by the pressure gradients on either side of the peak pressure. The peak in pressure within the interaction region exerts a pressure on the slow solar wind ahead and the fast solar wind behind. Over time the pressure gradients that develop steepen and eventually form

shocks. As we pass through the interaction region itself we also see a peak in density which, along with the increased magnetic field magnitude, contributes to the peak in pressure. At the interface between the interaction region and the fast solar wind stream we see a very sudden rise in flow speed and corresponding rise in the temperature. Throughout the interaction region and the just after the interface between the interaction region and fast solar wind stream we see a significant increase in magnetic field magnitude. This is a result of the compression of the magnetic fields within the two solar wind streams. Not shown here but also seen is a change in the flow angle of the solar wind across the interface. The slow solar wind stream prior to the interaction region is deflected westward and the fast solar wind stream following the interaction region is deflected eastward(Gosling and Pizzo, 1999).

Further space missions have allowed for additional in-situ observations of CIRs (e.g. Sanderson et al., 1998; Mason et al., 2009; Simunac et al., 2009; Tappin and Howard, 2009; Rouillard et al., 2009a, 2010b). These observations have allowed for the comparison of CIRs - and by extension the Sun between solar cycles (Mason et al., 2009). Observations have furthered our understanding of how small scale structures make up a CIR (Rouillard et al., 2009a, 2010b) and allowed a better understanding of how these structures impact the near-Earth environment (Sanderson et al., 1998) and how their arrival at the near-Earth environment might better be predicted (Simunac et al., 2009). In addition to the observations at (or very near to) 1 AU some spacecraft have made in-situ observations of CIRs and their impact at Venus (Dorrian et al., 2010; Whittaker et al., 2010), Mars (Edberg et al., 2010), Jupiter (Hanlon et al., 2004) and Saturn (Bunce et al., 2005; Jackman et al., 2005).

In addition to in-situ observations more recent space missions such as the Solar Mass Ejection Imager (SMEI) on the Coriolis spacecraft and especially the STEREO

mission have allowed remote imaging of the solar wind and its transients. These missions have allowed a detailed look at CIRs during their formation and as they progress through the heliosphere. They have been especially helpful in determining the evolution with time, something not previously possible with single point in-situ observations. The first observations of a CIR with the STEREO spacecraft (Rouillard et al., 2008; Sheeley et al., 2008b) revealed some of the fine structure within a CIR. Further observations have allowed for a greater study of the small transients which become entrained in CIRs (Rouillard et al., 2010a; Sheeley and Rouillard, 2010). In addition we can use the white light observations to complement in-situ observations and gain a greater understanding of our in-situ observations (Rouillard et al., 2010c; Sheeley et al., 2008a).

2.1.3. CIR impact on planetary exospheres

Although in general the densities and pressures associated with a CIR are smaller than those of a CME they can still have an impact on planetary magnetospheres and exospheres. However from a geomagnetic point of view the important part of CIRs is the intense magnetic fields associated with them which can couple to a planetary magnetosphere through reconnection. One measure of the resulting geomagnetic activity is the D_{st} (storm disturbance) index which is based on the average value of the horizontal component of the Earth's magnetic field measured by near-equatorial geomagnetic observatories. Geomagnetic storms can be seen in this index by a rise in the value followed by a decrease to large negative values before eventually returning to a value near zero (Gonzalez et al., 1994 and references therein). The initial increase is

associated with enhanced magnetopause currents as the magnetosphere is compressed by the forward pressure wave leading the CIR, the following decrease is due to the enhancement of the ring current due to the injection of plasma from the magnetotail into the inner magnetosphere. A CIR along with the D_{st} index from 1974 are shown in Figure 2.3.

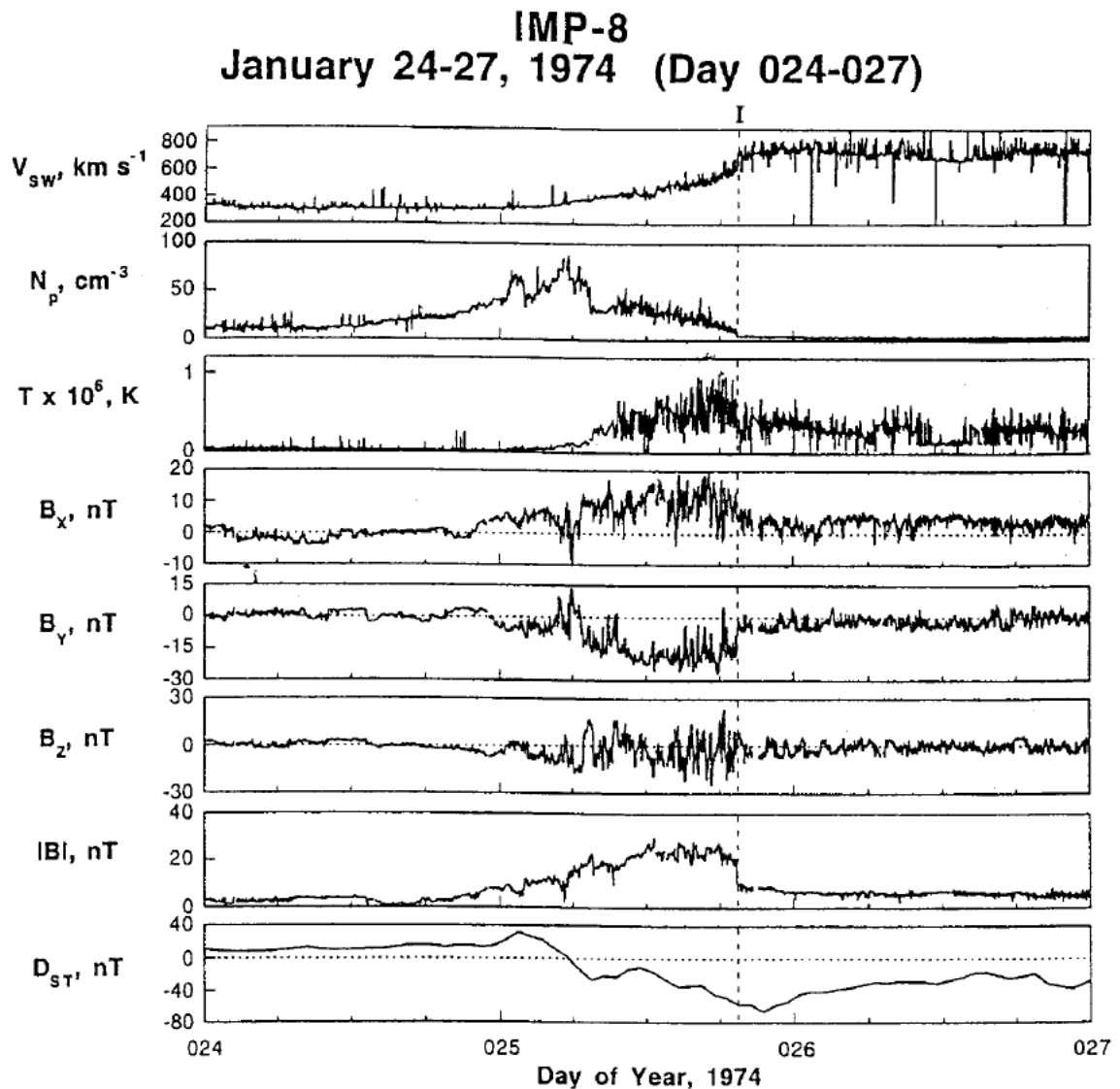


Figure 2.3: A CIR from January 24-27 1974 and associated geomagnetic activity. The interface between the reverse propagating pressure wave and the fast solar wind stream is indicated here by the vertical dashed line marked I. The solar wind properties here were measured by the IMP-8 spacecraft. (Gonzalez, Tsurutani and De Gonzalez, 1999)

Figure 2.3 shows features of a CIR as in Figure 2.2 and additionally shows the magnetic field components and magnitude. From those we can see that magnetic field magnitude up to the interface is significantly larger than the field magnitude in the separate slow and fast solar wind streams. Here we can also see that the initial phase of the storm (the rise in D_{st} index) is associated with the increase in plasma density. However as a shock has not always developed at 1 AU this is not a sudden onset but a more gradual onset (compared to a CME as will be seen later). The large magnetic field magnitude is associated with the main phase of a geomagnetic storm. As the main phase is associated with a large southward B_z which is typically quite variable within a CIR the main phase is typically much less intense than for a CME (Gonzalez, Tsurutani and De Gonzalez, 1999). This is typical of many CIR driven storms and is best illustrated by Table 2.1 adapted from Gonzalez et al. (1999).

Storm Intensity	Definition	Percentage of CIRs causing a storm of this intensity
Intense	$D_{st} < -100$ nT	0%
Moderate	$-100 \text{ nT} \leq D_{st} \leq -50$ nT	29%
Small	$-50 \text{ nT} \leq D_{st} \leq -30$ nT	29%
Negligible storm activity	$-30 \text{ nT} \leq D_{st}$	41%

Table 2.1: Geoeffectiveness of CIRs from IMP-8 for days 1-241, 1974 using high speed streams with velocities greater than 600 km s^{-1} (Gonzalez, Tsurutani and De Gonzalez, 1999).

As we can see almost half of all CIRs do not produce any significant storm activity while those that do only produce small or moderate geomagnetic storms. Gonzalez et al., (1999) also states that similar results were obtained for the 1973 and 1975 data sets.

Looking at other planets we see that CIRs will have a variety of effects. This is dependent on the planet's own magnetosphere (or lack of) and the development of the CIR when it reaches those planets. For example the lack of a magnetosphere at Mars and the more developed CIR results in the loss of atmosphere as the pressure pulse from a CIR sweeps over the planet (Edberg et al., 2010; Lundin et al., 2008), while at Saturn CIRs have been observed to inject hot plasma into the magnetotail (Bunce et al., 2005). As this thesis is mostly concerned with CIRs in the near-Earth environment these interactions will not be discussed any further.

2.2. Coronal Mass Ejections

The term coronal mass ejection (CME) is used to describe large transient eruptions of mass from the solar corona into the heliosphere. This section describes the initiation and typical observable features of CMEs followed by a brief discussion of their impact on the near-Earth environment.

2.2.1. Initiation of CMEs

The precise physics of the initiation of CMEs are still not fully understood but we do have some knowledge of how CMEs are released into the solar wind. Initially it was thought that solar flares were the primary mechanism for the initiation of CMEs (e.g. Chapman, 1950; Gosling, 1997; Hale, 1931). However, early observations revealed that CMEs were more commonly seen in association with prominences erupting from the surface (Gosling et al., 1974). Despite this there were still some CMEs seen in association with solar flares. Additionally some CMEs are associated with emerging and shearing magnetic flux (Feynman, 1997).

Parameter	Value
Kinetic energy (CME, prominence and shock)	10^{25} J
Heating and radiation	10^{25} J
Work done against gravity	10^{24} J
Volume involved at initiation	10^{24} m ³
Energy density	10 J m ⁻³

Table 2.2: Energy requirements for a moderately large CME as estimated in Forbes (2000).

Most theories for CME initiation start with an existing magnetic field structure which is usually a prominence. This magnetic structure will have footpoints linked to active regions in the photosphere. The active regions will themselves move around on the photosphere and this eventually results in shearing or stressing of the magnetic fields. As the active regions move around and the magnetic field gets stressed energy is transferred to the magnetic field increasing the magnetic field energy density. This

drives the eruption as can be seen when we look at the energy requirements for a moderately large CME (Table 2.2) and the estimates for coronal energy sources (Table 2.3) (Forbes, 2000).

Form of energy	Observed average values	Energy density (J m^{-3})
Kinetic ($(m_p n V^2)/2$)	$n = 10^{15} \text{ m}^{-3}$, $V = 1000 \text{ m s}^{-1}$	10^{-6}
Thermal (nkT)	$T = 10^6 \text{ K}$	0.01
Gravitational ($m_p n g h$)	$h = 10^8 \text{ m}$	0.05
Magnetic ($B^2/2\mu_0$)	$B = 0.01 \text{ T}$	40

Table 2.3: Estimates of coronal energy sources from Forbes (2000).

As Forbes (2000) shows, only the magnetic energy density is able to initiate an eruption. The currents associated with the magnetic energy must either be force-free, i.e. the current is approximately parallel to the magnetic field, or confined to current sheets as the magnetic energy density greatly exceeds that of the thermal and gravitational energy densities. As a result storage models are divided into those which focus on force-free currents and those which focus on current sheets. An example of two of these models is shown in Figure 2.4. These models give possible methods for the storage of energy prior to a release mechanism.

Like the storage models there are several proposed models for the release mechanism. These models can be classified into four categories; those which use force-free models and ideal Magnetohydrodynamic (MHD) processes, those which use

resistive MHD models such as magnetic reconnection, those which use hybrid models where ideal MHD processes initiate the eruption but it is then sustained by magnetic reconnection, and finally a class of models which uses small deviations from a force-free model to initiate the eruption (Forbes, 2000).

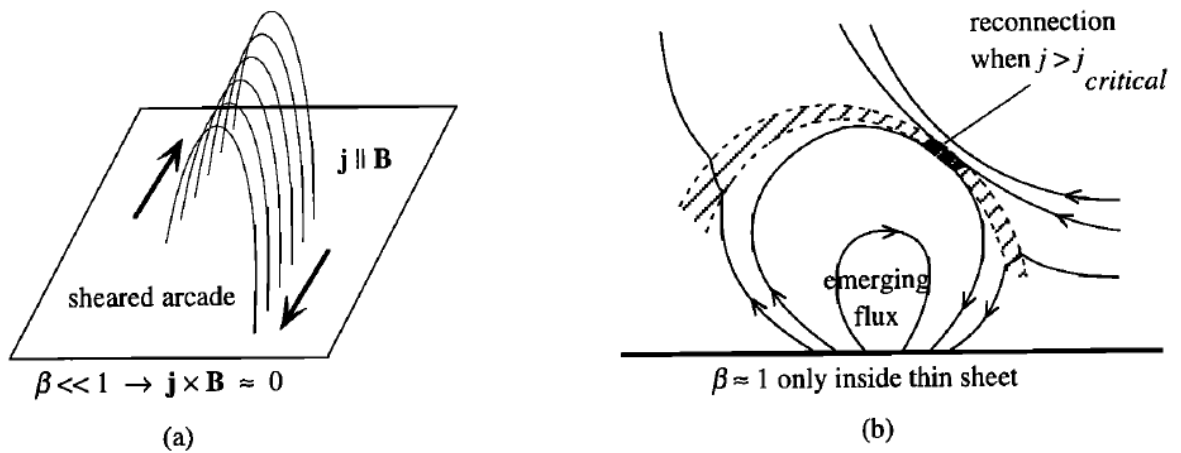


Figure 2.4: Examples of coronal configurations, (a) is a force-free field and (b) is a field containing a thin current sheet (Forbes, 2000).

While this thesis does not study the processes of CME initiation a basic understanding of CME initiation is useful for the appreciation of CME propagation and evolution which is of interest for this thesis.

2.2.2. Observations of CMEs

Like CIRs we can split observations of CMEs into remote imaging and in-situ observations and each can tell us different things about CMEs. Here we will start with remote imaging observations and what they tell us about CMEs.

Many remote imaging observations are from coronagraphs in ground based observatories and several spacecraft over the years. Coronagraphs are very helpful for informing us of the evolution of CMEs close to the Sun and an example of a coronagraph observation from the Large Angle Spectrometric Coronagraph (LASCO) on the Solar and Heliospheric Observatory (SOHO) spacecraft is shown in Figure 2.5.

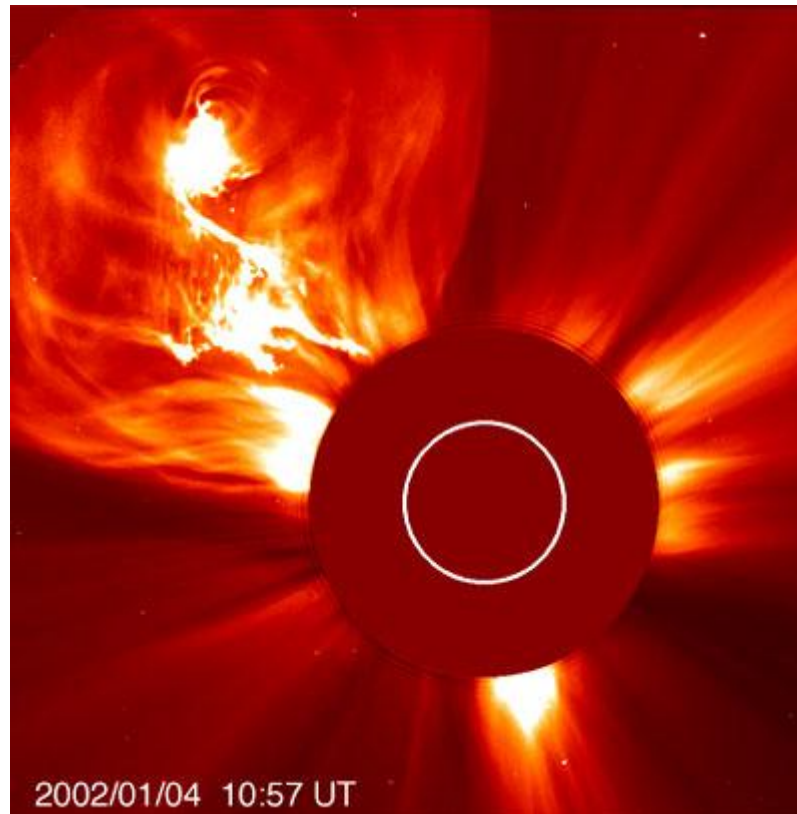


Figure 2.5: An example of a complex CME exploding off to the north-west of the Sun as seen by SOHO/LASCO. The white disc indicates the solar photosphere surface and the dark disc is the occulter which allows for the transients to be seen.

From coronagraphs we have learned that CMEs are limited in angular extent both longitudinally and latitudinally (Hundhausen, 1993) as a direct result of their initiation. From limited initial positions CMEs have been seen to expand at various rates and this expansion has been measured for a variety of CMEs (e.g. Cremades and Bothmer, 2004; Michalek, Gopalswamy and Yashiro, 2009; Savani et al., 2009). It has

been noted that CMEs have different expansion rates dependent on whether the CME is associated with a flare (Cremades and Bothmer, 2004) or a prominence eruption (Savani et al., 2009).

Other coronagraph observations have informed us about the speeds and accelerations of CMEs and similar to the expansion rate this appears to be dependent on the nature of the initiation (Andrews and Howard, 2001). The speed of CMEs has been observed to vary a great deal from speeds as low as 20 km s^{-1} to more than 900 km s^{-1} (Howard et al., 1997; Sheeley et al., 1999). CMEs associated with prominence eruptions are typically seen to accelerate from a low speed initially up to a speed similar to that of the slow solar wind streams (Andrews and Howard, 2001), while those associated with a flare are more impulsive and accelerate very quickly close to the Sun, typically reaching much higher speeds and giving the appearance of a constant speed in the field of view of most coronagraphs (Andrews and Howard, 2001). The first images from STEREO/HI also supported the appearance of CMEs maintaining their constant speed, approximately 600 km s^{-1} in this case, for around 15 hours (Harrison et al., 2008).

Another result which has been obtained from coronagraph observations is a rate for the occurrence of CMEs. This is variable with the solar cycle with the rate going as low as 0.8 CMEs per day at solar minimum when observed by SOHO/LASCO (Howard et al., 1997), while at solar maximum this rate goes up to around 3.5 CMEs per day (Gosling, 1997). There is a great deal of variability in these numbers between solar cycles and also between observations from different instruments. However despite this we can say that at solar minimum there are typically less than 1 event per day and at solar maximum there are around 3-4 events per day.

In-situ observations can tell us a great deal about the composition of CMEs and when combined with image observations can inform us about the structure of the magnetic fields within a CME. We will start with the composition from in-situ particle observations of CMEs. In-situ CME observations are generally different for each CME and there is no single feature of in-situ observations which can be used to identify a CME (Neugebauer and Goldstein, 1997). If you can observe several of these features then it is very probable that one is observing a CME passage. Neugebauer and Goldstein (1997) list nine features which we will summarise here. First they note that ion temperatures are unusually low for a given solar wind speed which they suggest is because the CME plasma pushes aside the solar wind and occupies a much larger volume than it would if it were channelled like the solar wind (Neugebauer and Goldstein, 1997). The second feature is an unusual anisotropy of the proton temperature with the parallel temperature being higher than the perpendicular temperature. Thirdly they list a higher helium abundance than is usual for the solar wind. They note that this is “patchy” and not always observed within the CME cloud but sometimes preceding it. They also note that there are no established theoretical foundations for why this occurs. Fourth, they list anomalies of abundances of other ion species for which they refer to Galvin (1997). Fifth, they list the bidirectional streaming of suprathermal electrons and energetic ions which they state is indicative of a closed magnetic configuration with both footpoints of the field still attached to the Sun. Sixth, they list strong magnetic fields which will be examined in more detail later. Seventh, the rotations of the magnetic field within the CME can be modelled as flux ropes or magnetic clouds, again this will be covered in more detail later. Eighth, a decreased flux of low energy cosmic rays as the increased density and magnetic field within the CME shields out the low

energy cosmic rays. Finally there are unusual ionization states of heavy ions within the CME indicative of a plasma source in a hot coronal loop or cold prominence material.

For the first of these conditions, the low ion temperatures Neugebauer and Goldstein (1997) also give a thermal index which has been used by other authors such as Richardson and Cane (1995) to identify CMEs over a long period of time. Figure 2.6 below shows an example of a CME depicting many of the features they identify. Now we will move on to a discussion of the magnetic flux ropes and clouds which are a common feature present in CMEs. A magnetic flux rope is a cylindrical body of magnetised plasma containing twisted fields (Marubashi, 1997). They usually occupy a space just behind the main front and appear as a void in images, i.e. a strong magnetic field with a high magnetic pressure leads to a low plasma density. In-situ observations usually show a strong magnetic field magnitude with at least one of the components showing a smooth turning from negative to positive or vice-versa. This is illustrated in Figure 2.7 below.

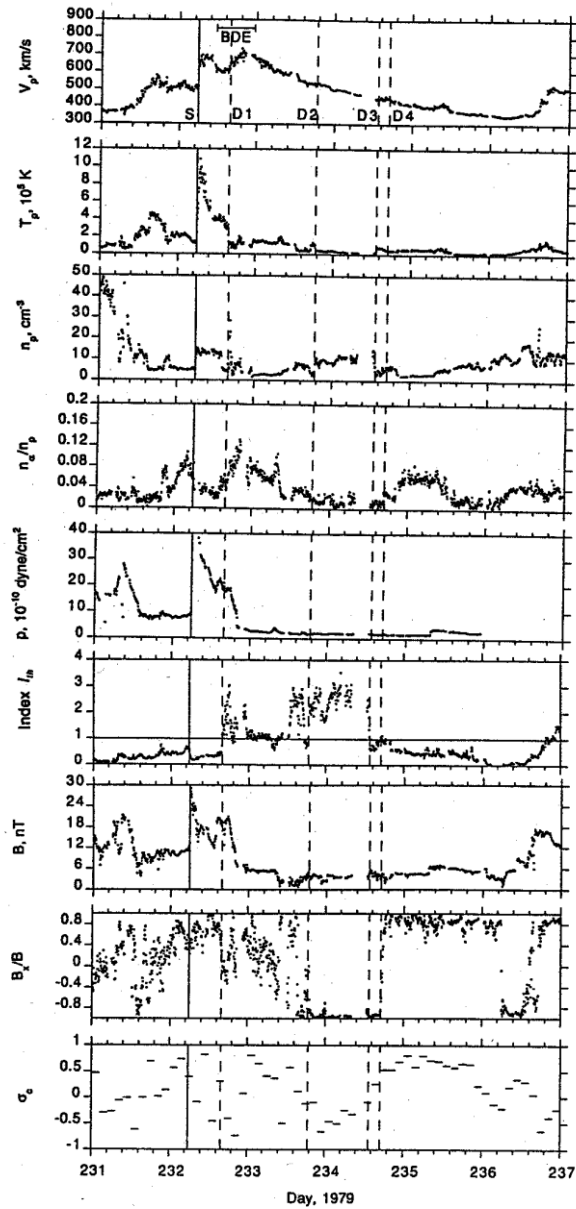


Figure 2.6: An example of in-situ data for a CME. From top to bottom the panels are proton speed, proton temperature, proton density, the ratio of alpha-particle to proton densities, total pressure (gas and magnetic), the thermal index as described in the text (also see Richardson and Cane (1995)), the magnitude of the magnetic field, the ratio of the radial magnetic field to the magnitude of the magnetic field and the normalized helicity (see Neugebauer and Goldstein (1997) and Zurbuchen and Richardson (2006)). The solid vertical line indicates the start of the event and 4 discontinuities are marked by D1-D4 with a dashed vertical line. Figure from Neugebauer and Goldstein (1997).

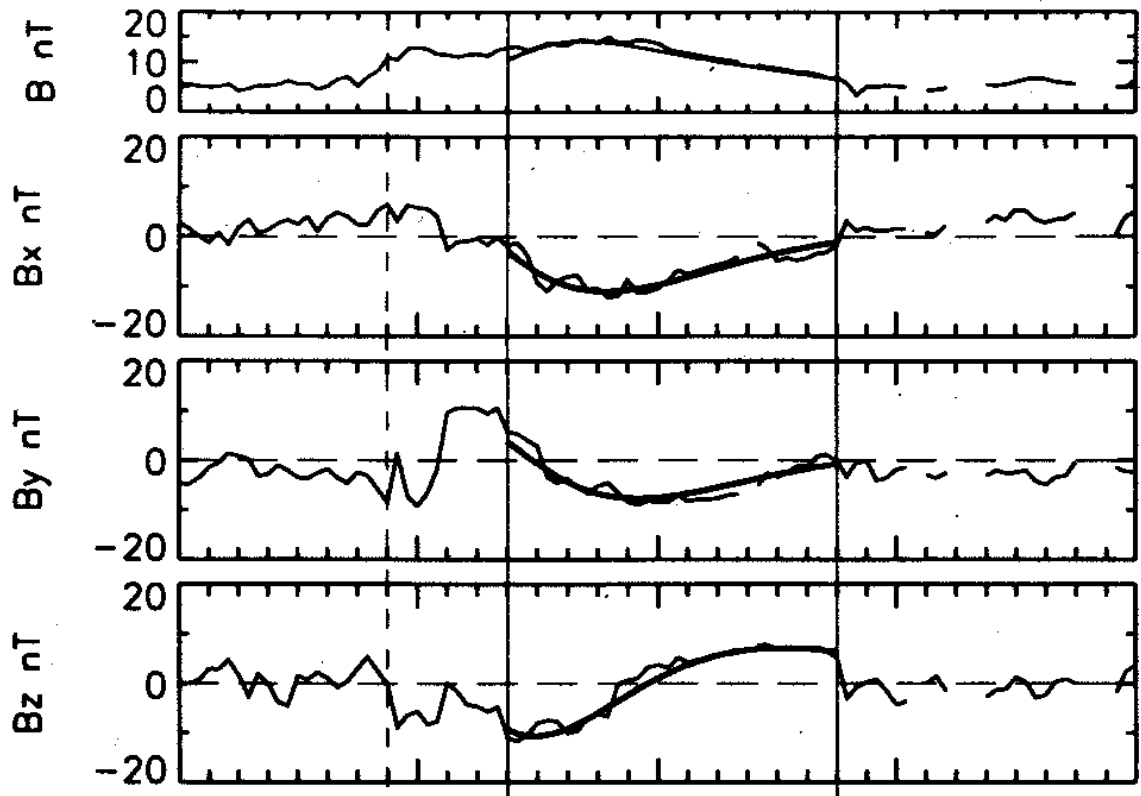


Figure 2.7: The magnetic field vectors and magnitude (top panel) for a flux rope from February 10-13 1969. The solid vertical lines indicate the extent of the flux rope and the thick curves show the results from a non-linear least squares fit. Taken from Marubashi (1997).

There is one further aspect of CMEs to be discussed and that is their impact on planetary magnetospheres. Unlike CIRs, as described earlier, the presence of a magnetic cloud or magnetic flux rope along with the higher speeds and densities present often results in a shock ahead of the CME which often leads to a larger impact on the Earth's magnetosphere. This is due to a long duration of strong magnetic field in one direction which results in a lot of magnetic coupling between the CME and the magnetosphere if it is in the right direction, i.e. southwards at Earth.

2.2.3. CME impact on planetary exospheres

As previously mentioned fast CMEs tend to produce strong shocks which have a much more significant impact on the Earth's magnetosphere and exosphere than a CIR. CMEs tend to produce major storm (D_{st} of less than -100 nT) which are generally accompanied by enhanced auroral activity and associated atmospheric and ionospheric effects (Luhmann, 1997). Unlike a CIR, which produces a recurrent storm approximately every 27 days, a CME is transient in nature and thus far we have very little ability to predict the occurrence and arrival of Earth-directed CMEs. However the arrival of the STEREO spacecraft have enabled some ability to predict the arrival of a CME which has already left the Sun.

3. Instrumentation

This chapter focuses on the details of the instruments used in this study. The primary focus is on NASA's twin Solar TERrestrial RELations Observatory (STEREO) spacecraft, and in particular the imaging instruments on board these spacecraft. Also described are the multiple in-situ instruments that have been used in this study, including those on the STEREO spacecraft as well as others.

3.1. The STEREO mission

3.1.1. Introduction

As discussed in chapter 2 physicists have long studied Coronal Mass Ejections (CMEs) and their influence on the near-Earth environment. Their arrival at Earth is often the cause of major geomagnetic storms that can have an adverse effect on spacecraft operating in the near-Earth environment and Earth-based systems. Society's increased reliance on spacecraft has also lead to an increased vulnerability to these storms. However, we are still unable to predict reliably when CMEs will occur.

STEREO was launched on 26 October 2006 at 00:52 UT from Cape Canaveral on a Delta II rocket. At the time of launch CMEs had been studied from their initial lift-off at the Sun through to a region near the Sun, 10-15% of their way to 1 AU, while some spacecraft have been able to measure their passing in-situ near Earth and others still have been able to examine their effects on the near-Earth environment. However there

has not been a mission which has studied CMEs continuously from the Sun to the Earth. STEREO is a mission designed to fill this gap and allow CMEs to be followed from initiation to their impact on the Earth, and from two spacecraft thus allowing a stereoscopic view.

The specific science goals of the STEREO mission are documented by Kaiser et al. (2008) as:

- Understanding the causes and mechanisms of CME initiation.
- Characterizing the propagation of CMEs through the heliosphere.
- Discovering the mechanisms and sites of solar energetic particle acceleration in the low corona and interplanetary medium.
- Developing a three-dimensional, time-dependent model of the magnetic topology, temperature, density and velocity structure of the solar wind.

To better investigate these science goals they were split into a set of measurement requirements by Kaiser et al. (2008) repeated here in Table 3.1.

The stated minimum success criterion for the STEREO mission was to make the measurements in table 1 for a period of 150 days after achieving heliocentric orbit, followed by at least one of the spacecraft continuing to make the full suite of measurements for the remainder of the two year prime mission. The 150 day interval required for minimum success was achieved on June 21, 2008, with full success achieved on January 23, 2009.

Scientific Objective	Measurement Requirement
Understanding the causes and mechanisms of CME initiation	<p>A Determine CME initiation time to within 10 minutes</p> <p>B Determine location of initiation to within five degrees of solar latitude and longitude</p>
Characterizing the propagation of CMEs through the heliosphere	<p>C Determine the evolution of CME mass distribution and the longitudinal extent to within five degrees as it propagates</p> <p>D Determine the CME and MHD shock speeds to within 10% as it propagates</p> <p>E Determine the direction of the CME and MHD shock propagation to within five degrees</p>
Discovering the mechanisms and sites of solar energetic particle acceleration in the low corona and interplanetary medium	<p>F Develop distribution functions to an accuracy of 10% for electrons and/or ions with energies typical of solar energetic particle populations</p> <p>G Locate regions of particle acceleration in the low corona to within 300,000 km in radius and in interplanetary space to within 20 degrees in longitude</p>

Developing a three-dimensional, time-dependent model of the magnetic topology, temperature, density and velocity structure of the ambient solar wind	H Obtain a time series of the solar wind temperature to within 10% accuracy at two points separated in solar longitude
	I Obtain a time series of solar wind density to within 10% accuracy at two points separated in solar longitude
	J Obtain a time series of solar wind speed to within 10% accuracy at two points separated in solar longitude
	K Measure global magnetic field topology near the ecliptic by determining the magnetic field direction to within 10 degrees

Table 3.1: STEREO Level 1 science requirements (Kaiser et al., 2008).

Each of the level 1 science measurements listed in Table 3.1 can be made by several combinations of instruments on the STEREO spacecraft so that the loss of any single instrument does not prevent any of the science requirements from being achieved. Although the daily rate of CMEs varies with the solar cycle, from approximately 0.5 per day at solar minimum to several per day at solar maximum, there is no dependence on the mission operating within a particular phase of the solar cycle to achieve mission success.

3.1.2. Orbital design

STEREO consists of two near-identical spacecraft; one leading the Earth (STEREO-A) and one trailing the Earth (STEREO-B) in heliocentric orbits. Each spacecraft orbits in slightly eccentric orbit with an average orbital distance slightly less than 1 AU for STEREO-A and slightly larger than 1 AU for STEREO-B such that the separation of each spacecraft from the Sun-Earth line increases by approximately 22° per year. This orbital configuration is shown in Figure 3.1. The angular separation does not increase linearly due to the eccentricity of the Earth's orbit and the spacecraft's orbit and the evolution of the separation is shown in Figure 3.2. To achieve the final orbits a series of lunar flybys were performed with STEREO A ejected into heliocentric orbit 52 days after launch and STEREO B ejected a further 38 days later.

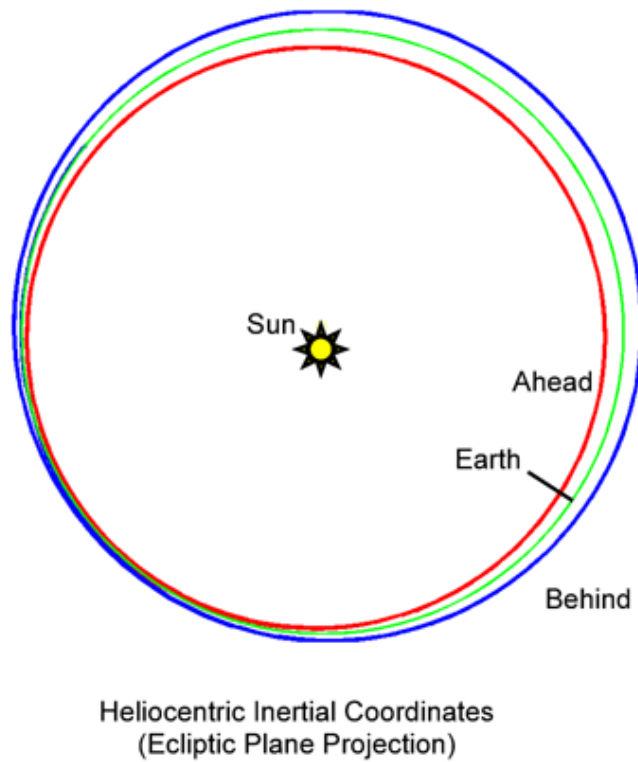


Figure 3.1: The STEREO orbits projected onto the ecliptic plane in Heliocentric Inertial Coordinates. The red orbit shows the path of STEREO A, the blue shows STEREO B, while the green line shows the orbit of Earth (Driesman, Hynes and Cancro, 2008).

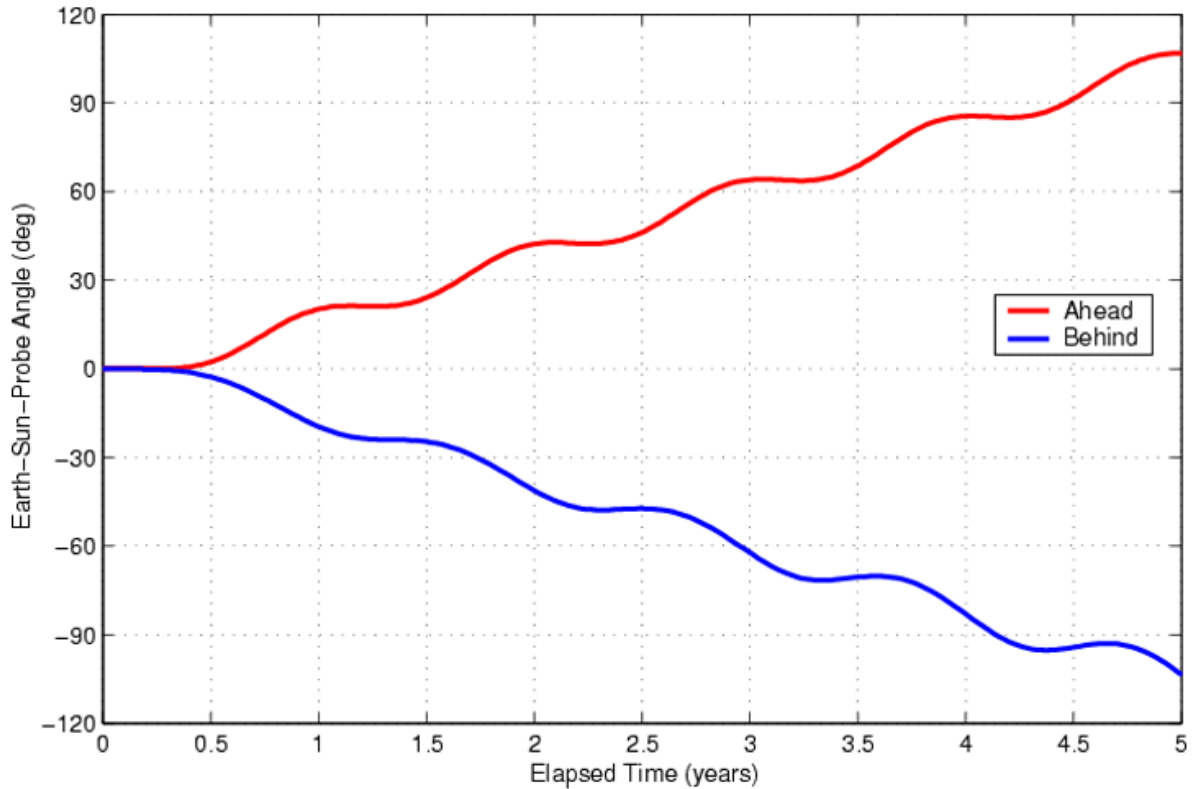


Figure 3.2: The relative separations of the two spacecraft based on the prelaunch drift rates of 22° per year (Dreisman et al., 2008).

3.1.3. Instruments

To achieve the level 1 science requirements each of the STEREO spacecraft carries four measurement packages with a total of 18 instruments. The instrument packages are listed here and those used in this thesis are described in more detail later in the current chapter.

- Sun-Earth Connection Coronal and Heliospheric Investigation (SECCHI). SECCHI is a suite of remote sensing instruments including two white light coronagraphs, an extreme ultraviolet imager and two white-light heliospheric imagers. The imagers used in this package provide the majority of the data used in this thesis and are presented in more detail in section 3.1.3.1.

- In-situ Measurements of PArticles and CME Transients (IMPACT). This measures the interplanetary magnetic field, thermal and suprathermal solar wind electrons, and energetic electrons and ions over energies as given in Table 3.2. Some in-situ data from these instruments is used in the work in this thesis. The instruments in this package are also described in section 3.1.3.2.
- PLAsma and SupraThermal Ion Composition (PLASTIC). This package provides in-situ plasma characteristics of protons, alpha particles and heavy ions over energies as given in Table 3.2. Again some data from these instruments is used in this work and the instruments are described in section 3.1.3.3.
- STEREO/WAVES (S/WAVES) is an interplanetary radio burst tracker that observes the generation and evolution of radio disturbances from the Sun through to the orbit of Earth. S/WAVES uses three orthogonal monopole antenna elements, six meters in length. The S/WAVES instruments are not used in this thesis and are described by Bougeret et al. (2008), Bale et al. (2008) and Cecconi et al. (2008).

Kaiser et al. (2008) presents a table summarizing all the instruments on board the STEREO spacecraft. A modified version is shown in Table 3.2.

Package	Instrument	Acronym	Purpose
SECCHI	Inner Coronagraph	COR 1	Coronagraph 1.4-4.0 solar radii
	Outer Coronagraph	COR 2	Coronagraph 2-15 solar radii
	Extreme Ultraviolet Imager	EUVI	Extreme Ultraviolet Imager

	Heliospheric Imager	HI	Imager, 12 – 215 solar radii (plane of sky distance)
IMPACT	Solar Wind Electron Analyzer	SWEA	Solar wind electrons 1 to 3000 eV
	Suprathermal Electron Telescope	STE	Suprathermal electrons 2 - 100 keV
	Solar Electron and Proton Telescope	SEPT	Electrons 20 – 400 keV; protons 60 - 7000 keV
	Suprathermal Ion Telescope	SIT	Composition He-Fe 300 – 2000 keV/nucleon
	Low Energy Telescope	LET	Protons, He, heavy ions to 40 MeV/nucleon
	High Energy Telescope	HET	Protons, He, heavy ions to 100 MeV; electrons to 8 MeV
	Magnetometer	MAG	Vector Magnetic field to 65,536 nT
	PLASTIC	Solar Wind Sector	SWS
Suprathermal Ions Wide-Angle Partition Sector		WAP	Wide angle heavy ions 0.3 to 80 keV

S/WAVES	High Frequency Receiver	HFR	Electric field 125 kHz - 16 MHz
	Low Frequency Receiver	LFR	Electric field 2.5 - 160 kHz
	Fixed Frequency Receiver	FFR	Fixed frequency 32 or 34 MHz
	Time Domain Sampler	TDS	Time domain to 250k sample/sec

Table 3.2: STEREO instruments, modified from Kaiser et al. (2008).

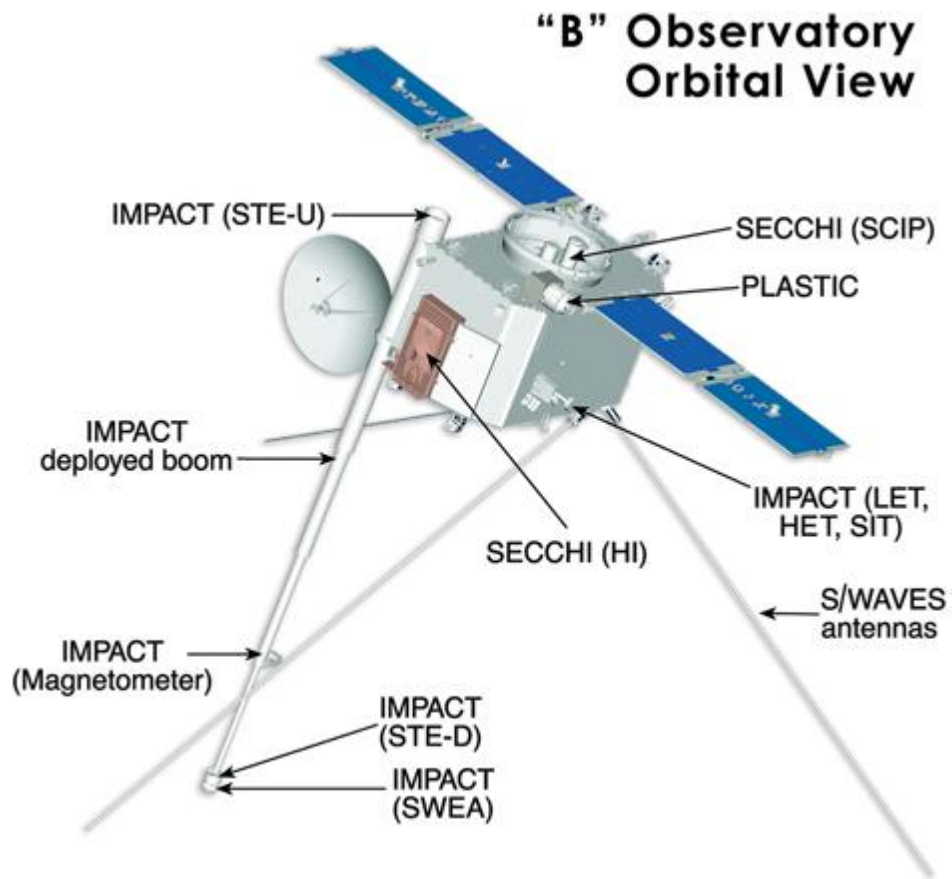


Figure 3.3: Artist's impression of the STEREO spacecraft as in Kaiser et al. (2008) showing the locations of some of the instruments.

Figure 3.3 shows an artist's impression of the STEREO Behind (B) spacecraft after the instruments have been deployed for use. The STEREO Ahead (A) spacecraft has a similar configuration although some instruments are in different positions so that the spacecraft can communicate with Earth.

3.1.3.1. The SECCHI Package

The SECCHI package comprises four remote sensing instruments designed to image the Sun from the surface out through the inner heliosphere to the vicinity of the Earth's orbit. This is achieved using five telescopes each covering a different region of the Sun or inner heliosphere. Starting at the Sun there is the Extreme Ultraviolet Imager (EUVI) which views the solar chromosphere and inner corona in four emission lines out to 1.7 solar radii. This imager is not used in this thesis as we do not study solar wind transients this close to the solar surface and so the details are not covered in this chapter. Further details are available in Howard et al. (2008). Overlapping with the outer portion of the field of view of the EUVI is the first of two visible light Lyot coronagraphs (COR1) with a field of view extending from 1.4 to 4 solar radii, again this instrument is not used in this study(Howard et al., 2008). Imaging the outer corona is the second coronagraph (COR2) with a field of view extending to 4° in elongation; the inner portion overlaps with the COR1 instrument. Elongation is the angle between the Sun-spacecraft line and the line joining the spacecraft with the observation point. COR2 is used in this thesis and the details of the instrument will be examined in greater detail later in the chapter. Moving to the outer corona/inner heliosphere STEREO carries the heliospheric imagers (HI), two imagers designed to study the heliosphere out to nearly 90° elongation, equivalent to 215 solar radii in the plane of the sky, which takes the viewing out to the vicinity of Earth's orbit. Data from these instruments are employed in a large part of the work in this thesis and these instruments will be examined in detail.

3.1.3.1.1. The COR2 instrument

The COR2 instrument observes the weak coronal light in the visible spectrum. It is an externally occulted Lyot coronagraph based on the heritage of the LASCO C2 and C3 coronagraphs on the SOHO spacecraft (Brueckner et al., 1995). It observes white light in the wavelength region 650 to 750 nm from the Sun that has been Thomson scattered by electrons in the corona. The coronagraph has been designed to have a lower stray light level than that of the COR1 instrument to allow observations at greater radial distances. In this way it complements the COR1 instrument and allows continuous coverage of the solar corona to 15 solar radii. The design of the COR2 instrument uses three lens groups, a spectral filter, a polarizer, and a three-disk external occulter to shield the objective lens from direct sunlight. The arrangement of the internal and external occulters and lens (detailed in Howard et al., 2008) defines the edges of the field of view of the instrument. This is $\pm 4^\circ$ elongation, corresponding to a radial distance of 15 solar radii in the corona when placed at 1 AU and is occulted at 2.5 solar radii. The mechanical design of the COR2 instrument is shown in Figure 3.4.

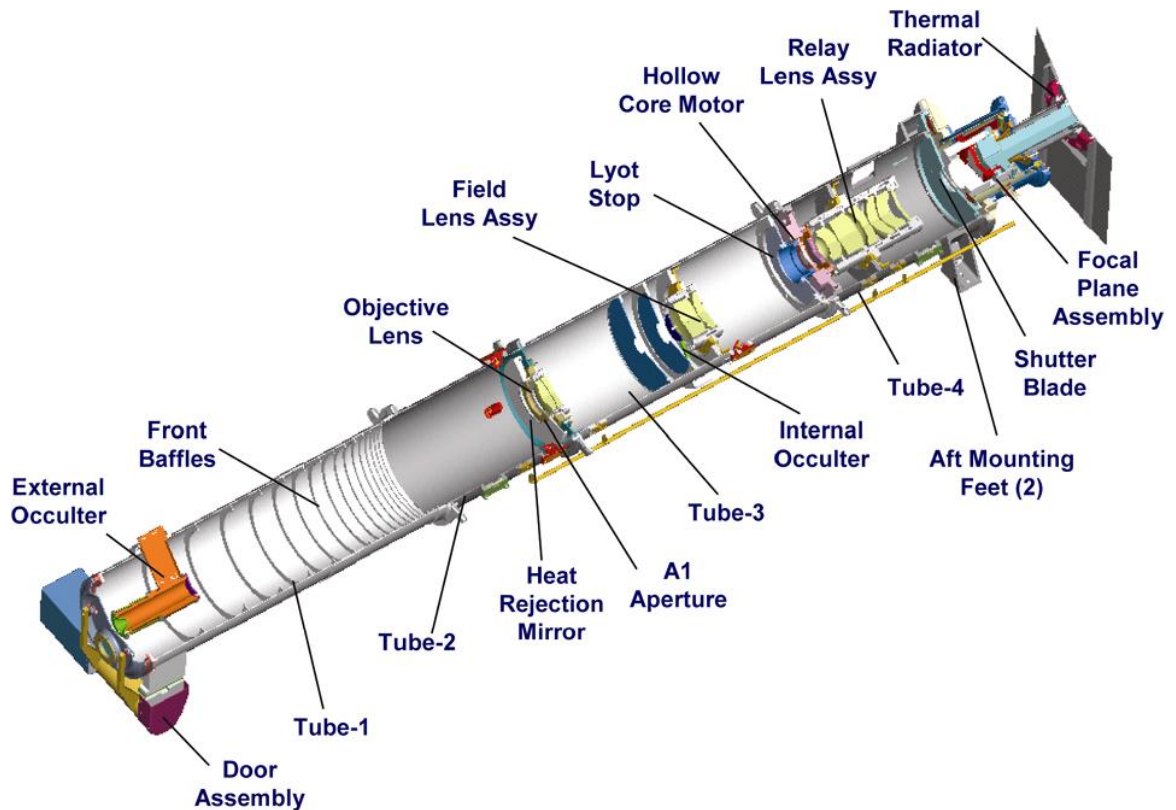


Figure 3.4: The COR2 mechanical layout, from Howard et al. (2008).

The flight unit performance was measured at the Naval Research Laboratory's Solar Coronagraph Optical Test Chamber measuring the vignetting function, that is the response of the image brightness and saturation as a function of position in the image, and spectral response in air, while the stray light levels, image quality and photometric calibration were tested in vacuum. From these tests it was determined that the instrument performance exceeded the design specifications as shown in Table 3.3.

An example of a COR2 image after basic processing to remove the flat-field response, vignetting and other instrumental effects is shown in Figure 3.5.

Parameter	Units	STEREO	STEREO
		Ahead	Behind
Field of view (half angle)	Degrees	4	4
Inner limit of field of view	Solar Radii	2.5	2.5
Pixel size, full resolution	arcsec	14.7	14.7
RMS spot size (design)	arcsec	15	15
Planned exposure time	sec	<4	<4
Polarizer attenuation	-	10^{-4}	10^{-4}
Photometric response	B_{Sun}/DN	1.35×10^{-12}	1.25×10^{-12}
Time to complete pB sequence	sec	11	11
Image sequence cadence	Min	15	15

Table 3.3: COR2 performance requirements from Howard et al. (2008).

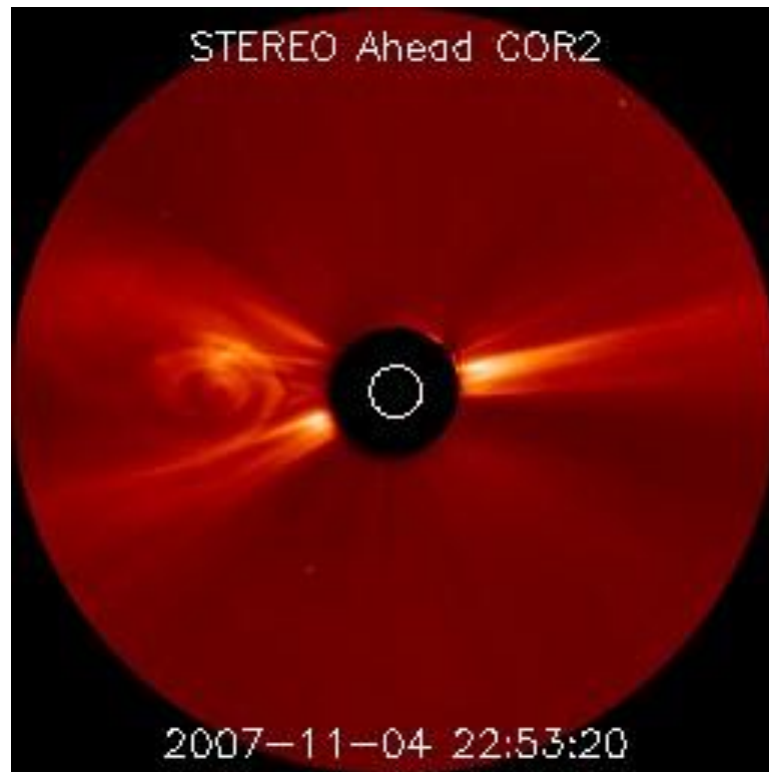


Figure 3.5: An example COR2 image from STEREO A on the 4th November 2007 showing a CME on the left hand side of the image. The black filled disc in the centre is the occulter, while the white circle shows the location of the Sun.

3.1.3.1.2. The Heliospheric Imagers

Until the launch of the STEREO mission in 2006 there were no instruments able to image space near the Sun-Earth line. By moving away from the Sun-Earth line STEREO provided the opportunity to image this region and this is achieved with the Heliospheric Imagers (HI). The HI instrument comprise 2 cameras, HI-1 and HI-2, with 20° and 70° fields of view respectively. Both cameras are aligned in the ecliptic plane with HI-1 off-pointed from the Sun direction by 14.0° and HI-2 off-pointed by 53.7°. This arrangement covers ecliptic elongations to approximately 90°.

Figure 3.6 shows the overlapping fields of view of the HI-1 and HI-2 cameras projected on the plane of the sky. However the corona is optically thin so that the location of objects within the field of view cannot be assumed to be in this plane. Figure 3.7 better illustrates this, it shows a projection, from above, of the ecliptic plane with the fields of view of the HI instruments on STEREO A and B overlaid in grey and bounded by dashed lines.

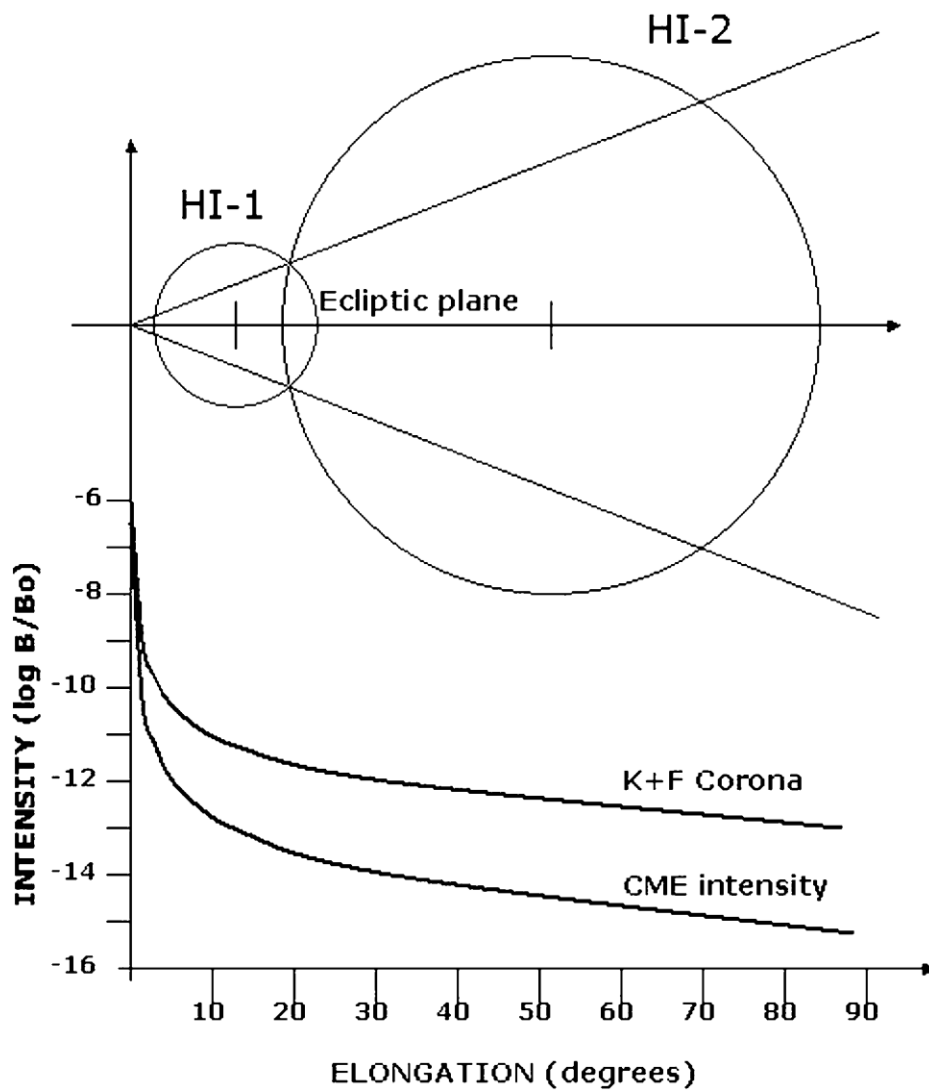


Figure 3.6: The field of view geometry of the HI instrument and the expected intensities of the corona and CMEs. Adapted from Socker et al. (2000).

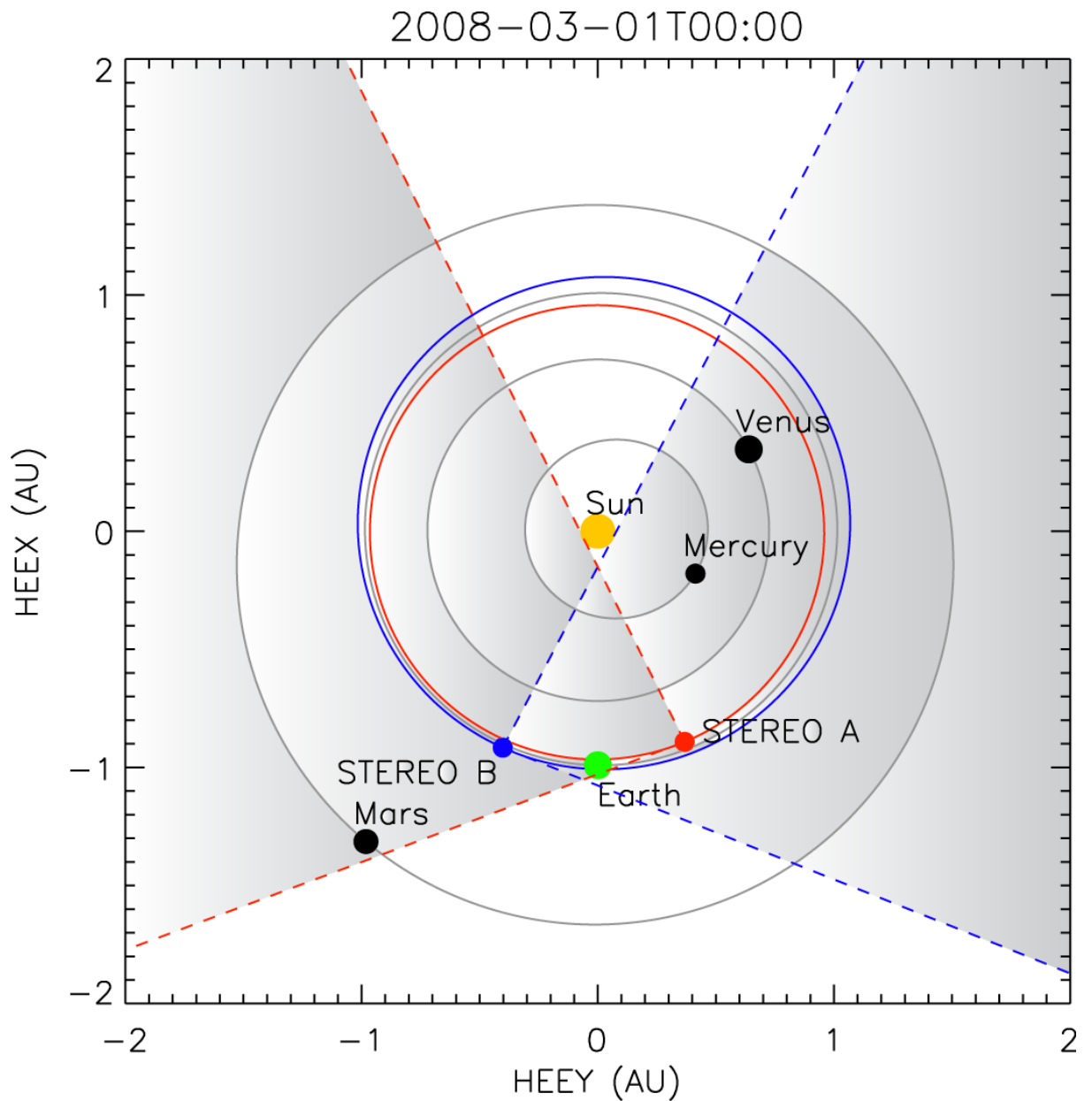


Figure 3.7: The location of STEREO A (red) and STEREO B (blue) on the 1st March 2008 projected onto the ecliptic plane. The coordinates are heliocentric Earth ecliptic Cartesian coordinates in units of 1 AU. The orbits and locations of Mercury, Venus, Earth and Mars are also shown. The dashed red and blue lines indicate the edges of the HI instrument fields of view on STEREO A and B respectively. These regions are also shaded grey to further highlight what will be visible in HI images.

The HI instrument is box shaped approximately 0.8 m long which initially was protected by a door. A detailed design of the instrument is shown in Figure 3.8 taken from Eyles et al. (2009). As Figure 3.8 shows, the two HI cameras are inset into the mounting with a series of baffles to reject stray light from the Sun. Notice that the HI-2 camera is set deeper into the instrument with more baffles so that the camera can measure the desired intensities. Amongst these baffles is an Earth occulter to protect the CCD of the HI-2 camera during the early phase of the mission when the Earth would appear as a very bright object. A protective door shielded the instrument during the launch phase of the mission until 13 December 2006 for STEREO-A and 11 January 2007 for STEREO-B and is also shown.

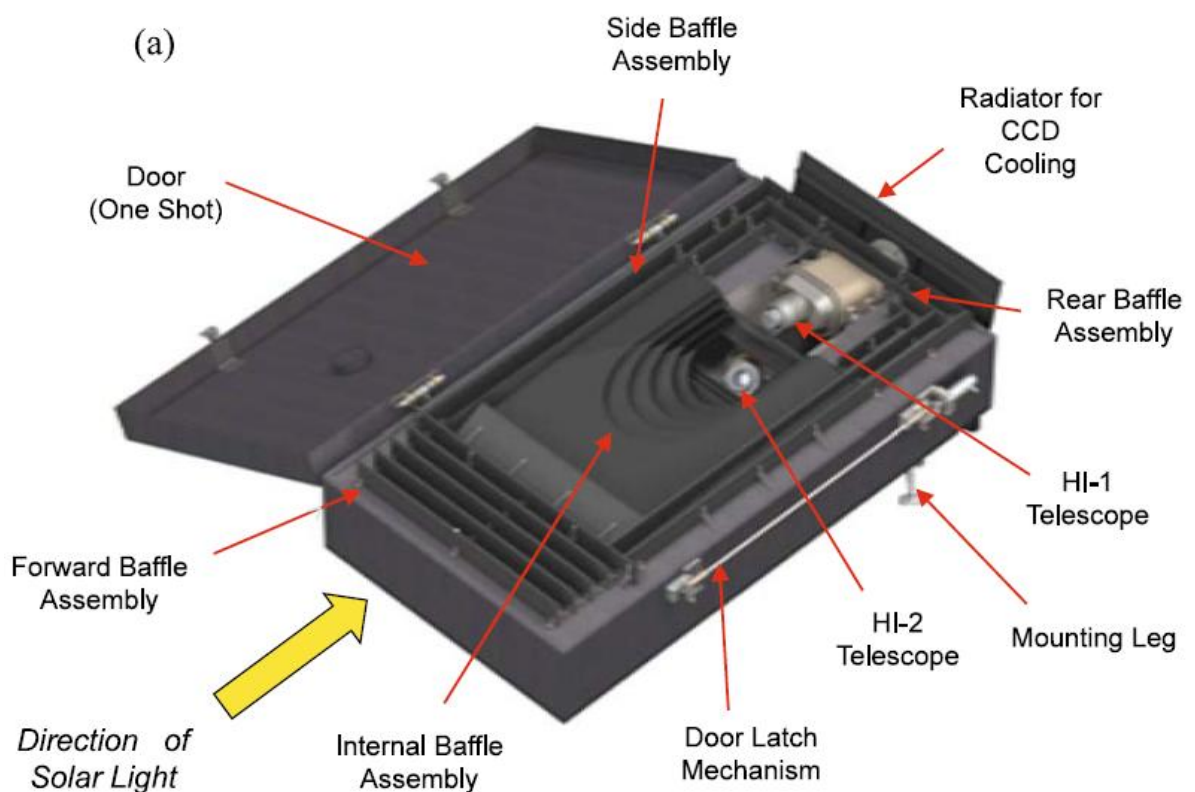


Figure 3.8: The Heliospheric Imager Design Concept (taken from Figure 3(a) of Eyles et al. (2009)).

	HI-1	HI-2
Direction of centre of field of view from Sun centre	14.0°	53.7°
Angular field of view	20°	70°
Angular range	4° - 24°	18.7° - 88.7°
CCD pixel size	35 arcsec	2 arcmin
Image array (2 x 2 binning)	1024 x 1024	1024 x 1024
Image bin size	70 arcsec	4 arcmin
Spectral bandpass	630 – 730 nm	400 – 1000 nm
Exposure time*	40 seconds	50 seconds
Exposures per summed image sequence*	30	99
Summed image cadence*	40 minutes	2 hours
Brightness sensitivity (1 unit = solar disc brightness)	3×10^{-15}	3×10^{-16}
Stray-light rejection (outer edge of field) (1 unit = solar disc brightness)	3×10^{-13}	10^{-14}

*Table 3.4: Performance requirements of the HI instruments (Eyles et al., 2009). * indicates that these are actual values optimised during mission operations rather than the original specifications.*

The performance specifications of the HI instruments as reported by Eyles et al. (2009) are shown in Table 3.4.

The HI detectors are CCDs with 2048 x 2048 pixels which for science operations are binned onboard to 1024 x 1024 image arrays. To obtain a sufficient statistical accuracy, long duration exposures are required but cosmic ray impacts would ruin such images if taken as single exposures. Thus much shorter exposures are taken and scrubbed of cosmic rays onboard before being summed to create a single image. For the HI-1 instrument 30 exposures are used for a total exposure time of 40 minutes and for HI-2 99 exposures are used for a exposure time of 2 hours. Like the COR2 instrument the HI detectors view Thomson scattered white light. The HI-1 instrument has a bandpass similar to COR2 of 630 to 730 nm, while the HI-2 instrument has a much broader bandpass of 400-1000 nm. This difference is so that the weaker coronal is maximised at the larger elongations seen in the HI-2 instrument. As previously mentioned a series of baffles on the instrument reject stray light so that the required brightness sensitivity can be achieved. For the stray-light level to not have a significant contribution to the statistical error it must be an order of magnitude lower than the coronal signal. The coronal signal and expected CME intensity across the visible elongations are shown in Figure 3.6, adapted from Socker et al. (2000).

3.1.3.1.3. Data Processing

The raw data from the HI instruments are dominated by the coronal signal and also have several instrumental effects that must be corrected in order for transient solar wind structures to be visible. Due to mechanical constraints the HI cameras do not have

shutters. Thus the CCDs are continuously exposed to the sky during the image readout process. This results in some smearing of the images during readout which is corrected (Eyles et al., 2009, section 10.1.2).

The nature of CCDs means that sometimes bright objects can saturate pixels leading to excess charge bleeding into adjacent pixels in the same column. The CCD design prevents charge bleeding horizontally across columns. As saturation in a column invalidates the shutterless correction all values in the column must be replaced with NaN before the shutterless correction takes place.

After shutterless correction has been performed a flat-field correction is applied and photometric conversion to the data occurs to produce the final image. Finally the headers of each image are updated with corrected pointing parameters, which previously had been found to be incorrect.

To reveal transient structures in the solar wind, such as CMEs, a background subtraction must be applied to remove the much brighter F-corona. This is only possible if the background is relatively constant over a period of several days, which is usually the case. To calculate the background intensity a minimum value over several images is found for each pixel then removed from that pixel in all images. This leaves the star background, which drifts across the field of view with the movement of the spacecraft, and transient structures in the field of view. A fully processed HI-1A image with the coronal background removed is shown in Figure 3.9.

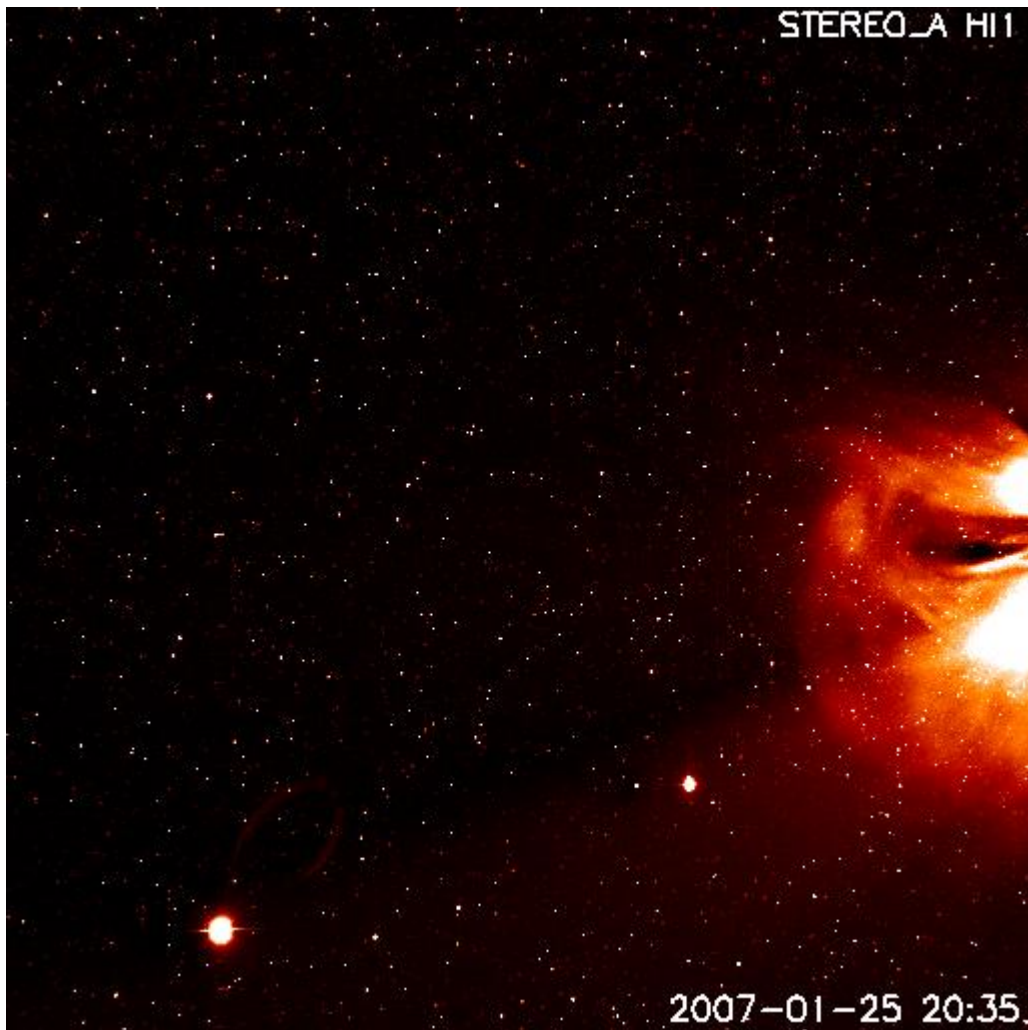


Figure 3.9: A processed HI-1A image from the 25th January 2007 showing a CME. Venus (bottom left) and Mercury are also visible.

3.1.3.2. The IMPACT package

The IMPACT package was designed to produce multipoint measurements of the solar wind and suprathermal electrons. IMPACT consists of seven in-situ sensors and a telescoping boom designed to maximise the STEREO mission goals of understanding CME structure in 3-D. In the early phases of the mission, while the angular separation of the spacecraft was small, it was anticipated that a CME would be observed in-situ at

both spacecraft. After the separation reached approximately 90° it was anticipated that this would no longer be the case and instead the primary focus would shift to comparing SECCHI observations with in-situ observations from the IMPACT package (Luhmann et al., 2008a).

The primary instrument used in this thesis from this package is the magnetometer (MAG) which is visible in Figure 3.3 on the deployable boom approximately 3m from the spacecraft body. The magnetometer is a conventional three-axis fluxgate design used on many missions (Acuña et al., 2008). The boom was deployed and instruments activated on November 1, 2006. The active range of the magnetometer is $\pm 65,536$ nT although the operational range used for the majority of the mission is ± 512 nT.

Data from the six other instruments in the IMPACT package are not used in this thesis. These instruments are listed in Table 3.2 and are briefly covered here. The Solar Wind Electron Analyzer (SWEA) (Sauvaud et al., 2008) measures the distribution of solar wind electrons in the energy range 1 – 3000 eV. The Suprathermal Electron (STE) instrument (Lin et al., 2008) measures electrons in the range 2 – 100 keV which is the primary energy range for impulsive energetic particle events. The Suprathermal Ion Telescope (SIT) (Mason et al., 2008) identifies the heavy ion composition at low energies, ~ 20 keV/nucleon to ~ 10 MeV/nucleon, allowing studies of these low energy ions in the solar wind. The Low-Energy Telescope (LET) (Mewaldt et al., 2008) measures the elemental composition, energy spectra, angular distributions, and arrival times of ions in the energy range from ~ 3 to 30 MeV/nucleon. This measures the energetic particles that result from shocks associated with CMEs. The Solar Electron and Proton Telescope (SEPT) (Mueller-Mellin et al., 2008) has been designed to study the 3-D distribution of energetic electrons and protons with an energy resolution of 30 – 400 keV and 60 – 7,000 keV respectively. This instrument actually consists of two

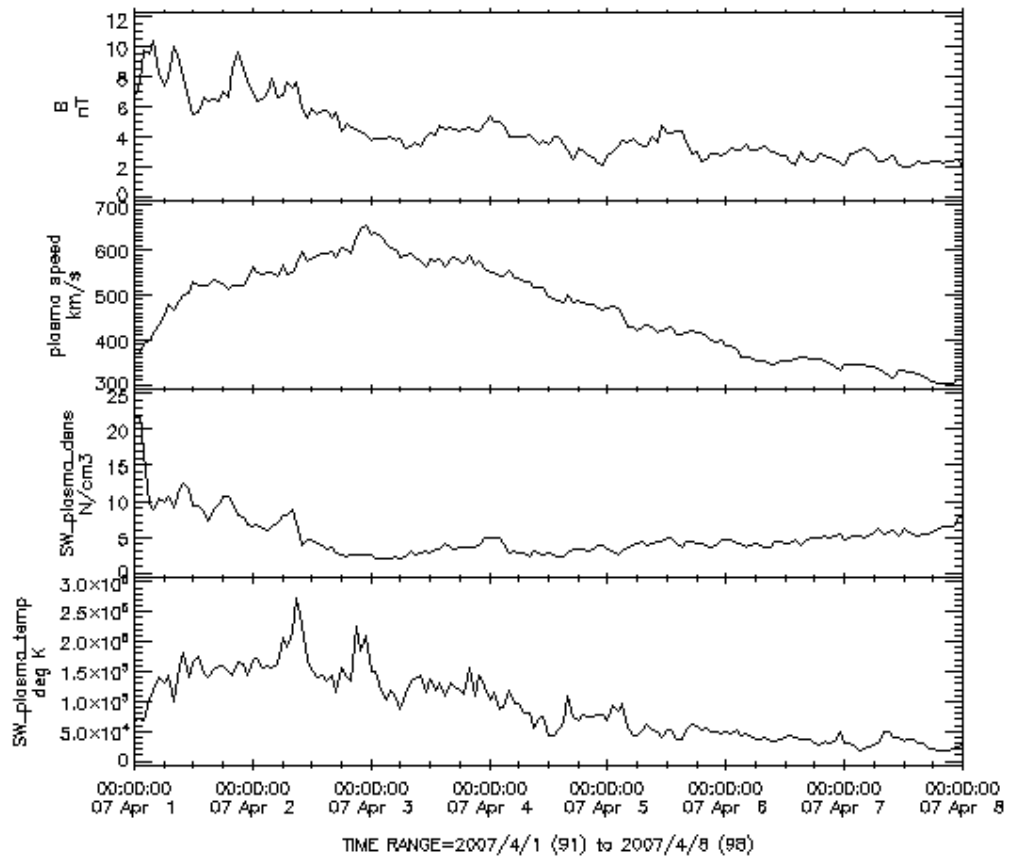
telescopes such that the entire sky can be covered. The High Energy Telescope (HET) (von Rosenvinge et al., 2008) measures the abundances and energy spectra of electrons and ion species from hydrogen to iron in a variety of energy ranges dependent on species.

3.1.3.3. The PLASTIC Package

The in-situ plasma measurements from STEREO used in this thesis are from the PLASTIC package which consists of two instruments to measure the bulk properties of solar wind protons and the composition and properties of minor ions, and to measure the composition, spectra, and anisotropy of suprathermal ions in the low energy-per-charge range of 0.3 to 80 keV/e. The mechanical details and science objectives of the PLASTIC package are covered in Galvin et al. (2008).

The data used in this thesis from the STEREO/PLASTIC and STEREO/IMPACT packages are provided by CDAWeb and are the merged hourly average values which are produced by N. Papitashvili at the NASA Goddard Space Flight Centre. Figure 3.10 shows an example of the final data output from STEREO A for the magnetic field magnitude, the plasma speed, density, and temperature.

sta MAG_PLASMA>Merged Trajectory, Magnetic Field, and Plasma C0H01HR>1 Hour Time Resolution from cohoweb



Please acknowledge data provider, Natasha Papitashvili at NASA/GSFC and CDAWeb when using these data.
Generated by CDAWeb on Thu Feb 2 09:19:51 2012

Figure 3.10: Example data output from STEREO A/PLASTIC from the 1st April 2007 to 8th April 2007. The top panel shows the magnitude of the magnetic field, the second panel shows the radial speed, the third panel shows the plasma density and the bottom panel shows the plasma temperature.

3.2. Summary

The majority of the data used in this thesis comes from the STEREO spacecraft and more specifically the HI instruments. These instruments allow us to view the transient solar wind and the orbits of the STEREO spacecraft allow the transients to be viewed from positions away from the Sun-Earth line. The STEREO spacecraft additionally provide in-situ data that are used primarily in chapter 5.

4. Deriving solar transient characteristics from single spacecraft STEREO/HI elongation variations: a theoretical assessment of the technique

4.1. Introduction

In this chapter we investigate the accuracy with which the characteristics of velocity and angle of propagation of solar wind transients can be determined from the HI observations of scattered sunlight. In their comprehensive analysis of Coronal Mass Ejections (CMEs) observed using the LASCO coronagraphs on the SOHO spacecraft (Brueckner et al., 1995), Sheeley et al. (1999) introduced the concept that the time-elongation profile of CMEs would exhibit an apparent acceleration or deceleration imposed by the observing geometry (elongation being the angle between the line from observer to Sun-centre and the line-of-sight). For the LASCO coronagraphs, the images from which extend to an outer limit of only 8° elongation, the authors assessed that this effect would be inconsequential. However, with the advent of heliospheric imaging out to far greater elongations - both by the Solar Mass Ejection Imager (SMEI) on the Coriolis spacecraft (Eyles et al., 2003) and more recently, the Heliospheric Imagers (HI) on the pair of NASA Solar TERrestrial RELations Observatory (STEREO) spacecraft (Eyles et al., 2009) - this artifact of the observing geometry is significant and is, indeed, proving to be extremely useful for defining the motion of solar wind transients (e.g. Rouillard et al., 2008, 2009a,b, 2010a,b; Sheeley et al., 2008a,b)

For an observer close to the ecliptic plane (as is the case for both the Coriolis and STEREO spacecraft) viewing a solar transient passage along the ecliptic, β corresponds to the longitude difference between the observer and transient event in an ecliptic coordinate system. This is illustrated in Figure 4.1, which shows the location of the two STEREO spacecraft in the ecliptic plane (X-Y plane in Heliospheric Earth Ecliptic coordinates, HEE) on the 1st January 2009. The locations of the Sun, Earth and other inner planets are also shown. Angles α_A and α_B in Figure 4.1 correspond to the elongation of a point P in the inner heliosphere, as viewed from STEREO A and B, respectively. P can be considered to be the location, at time t , of a solar transient propagating anti-sunward with a radial velocity V_r at a longitudes β_A and β_B with respect to STEREO A and B.

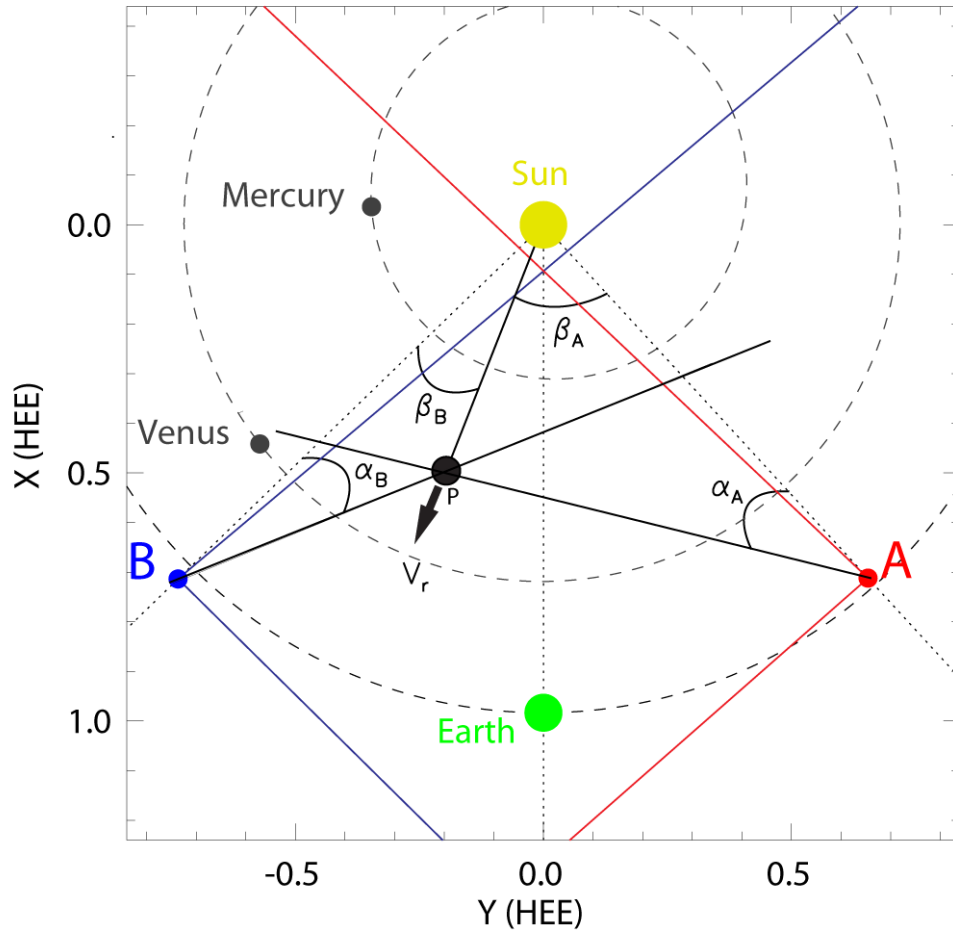


Figure 4.1: The locations of STEREO A(head: red) and B(behind: blue) in the ecliptic plane on 1st January 2009, illustrating the extent of the HI field of view on each spacecraft. The elongation of P, which corresponds to a solar transient moving with velocity V_r at an angle β_A (β_B) with respect to STEREO A (B), is α_A and α_B for spacecraft A and B, respectively.

For any given solar transient viewed by an observer situated at a radial distance r_A , from the sun, the shape of its time-elongation profile (the variation of elongation, α , as a function of time, t) can be obtained from an elongation-time map (commonly referred to as a J-map, Sheeley et al. 1999). This shape depends upon its radial velocity, V_r , and the angle between its propagation path and the Sun-observer line, which we call β (Rouillard et al., 2008). The shape of the time-elongation profile can be derived from Figure 4.1 by applying the sine rule to the triangle formed by the Sun, the point P and

one spacecraft, for this derivation we will use STEREO A although the derivation is equally applicable for STEREO B and by assuming that the angle β remains constant. If we take the distance from the Sun to the point P to be d and the distance from the Sun to STEREO A to be r , then using the sine rule we get equation 4.1.

$$\frac{\sin (180 - [\beta + \alpha])}{r} = \frac{\sin \alpha}{d} \quad 4.1.$$

Using the formula for sine subtraction we can express the numerator of the left hand side purely in terms of β and α as in equation 4.2.

$$\sin(180 - [\beta + \alpha]) = \sin 180 \cos(\beta + \alpha) - \cos 180 \sin(\beta + \alpha) \quad 4.2.$$

This expression can be reduced to $\sin(\beta + \alpha)$ as $\sin 180$ is equal to 0 and $\cos 180$ is equal to -1. We can then expand $\sin(\beta + \alpha)$ again using the sin addition rule and substitute the result into equation 4.1 to obtain equation 4.3.

$$\frac{\sin \beta \cos \alpha + \cos \beta \sin \alpha}{r} = \frac{\sin \alpha}{d} \quad 4.3.$$

If we now divide by $\cos \alpha$, multiply by r and d and then collect the terms for α we obtain equation 4.4.

$$d \sin \beta = \tan \alpha (r - d \cos \beta) \quad 4.4.$$

If we assume that the transient P has travelled at a constant velocity for the entire length d then we can replace d with $V_r t$. Then to obtain our final expression for the elongation with respect to time we divide by $(r - V_r t \cos \beta)$ and take the inverse tangent of the result to obtain equation 4.5.

$$\alpha(t) = \arctan \left[\frac{V_r t \sin \beta}{r - V_r t \cos \beta} \right] \quad 4.5.$$

Although the radial distance of the spacecraft r does change over time for transients moving over a timescale of a few days we can treat r as a constant. As will be discussed

later, the assumptions used are not necessarily always valid – transients can accelerate and decelerate, and they can be large in spatial extent. Here it is worth bearing mind that equation 4.5 works best when applied to narrow CME’s travelling at speeds close to the solar wind speed.

Figure 4.2 shows the curves transients produce in the STEREO/HI instruments if they are following equation 4.5. Panels (a) and (b) show transients travelling at a constant β of 45° with speeds ranging from 200 km s^{-1} up to 900 km s^{-1} in steps of 50 km s^{-1} for STEREO A and B respectively. The only real difference here is the value of r in equation 4.5 which is slightly larger for STEREO B but as can be seen from these two panels makes only a small difference to the shape of the tracks. Panels (c) and (d) show transients travelling at a constant speed of 400 km s^{-1} with a range of β from 10° to 90° in 10° steps for STEREO A and B respectively. In each of these panels the transients have been spaced out by 6 hours to better view the shape of each track. Additionally in panel (c) the order of the transients goes from a β of 90° to a β of 10° while that order is reversed for panel (d). This difference is due to allowing for solar rotation. Transients seen from the same source region in STEREO A will produce tracks with decreasing β over time whereas in STEREO B the tracks will have increasing β . This is particularly important when viewing CIRs as in chapter 5.

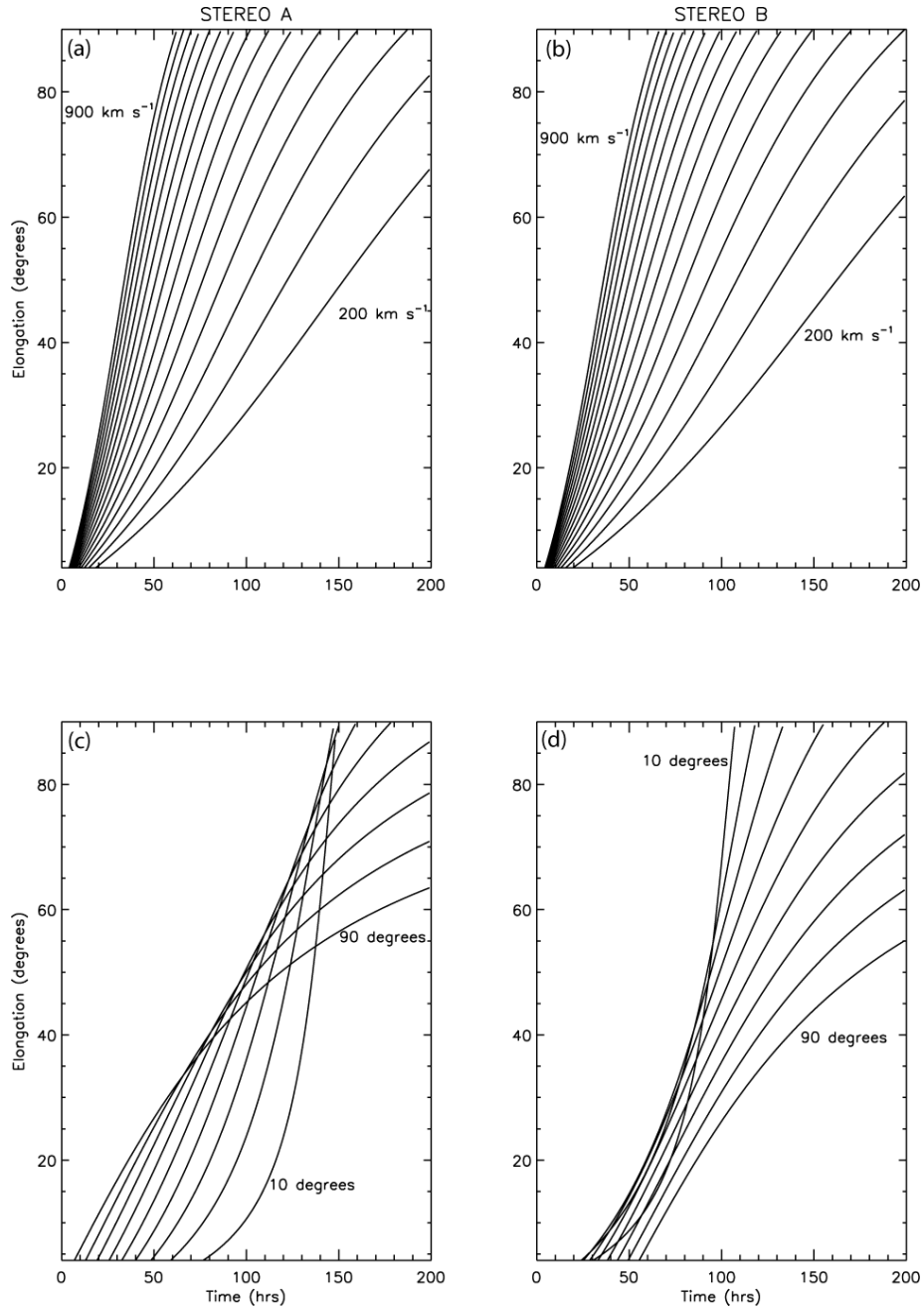


Figure 4.2: Theoretical curves indicating how transients would appear in the STEREO/HI instruments. Panels (a) and (b) show a transient travelling at an angle of 45° with velocities ranging from 200 km s^{-1} in 50 km s^{-1} steps for STEREO A and B respectively. Panels (c) and (d) show a transient travelling at 400 km s^{-1} at angles from 10° to 90° for STEREO A and B respectively. Note that in panels (c) and (d) the transients have been separated by 6 hours in time. Additionally in panel (c) the order of the tracks goes from $\beta=90^\circ$ to $\beta=10^\circ$ and panel (d) the order is reversed.

Finally, the Thomson Sphere can also affect the visibility of events in the J-maps, as once events move outside of the Thomson Sphere the intensity starts to fall off more rapidly. The Thomson Sphere is the surface of a sphere where the scattered material has the maximum intensity because light which has been Thomson scattered has the highest intensity when the angle between the incident light and scattered light is 90° . For the STEREO spacecraft the Thomson sphere is shown in Figure 4.3.

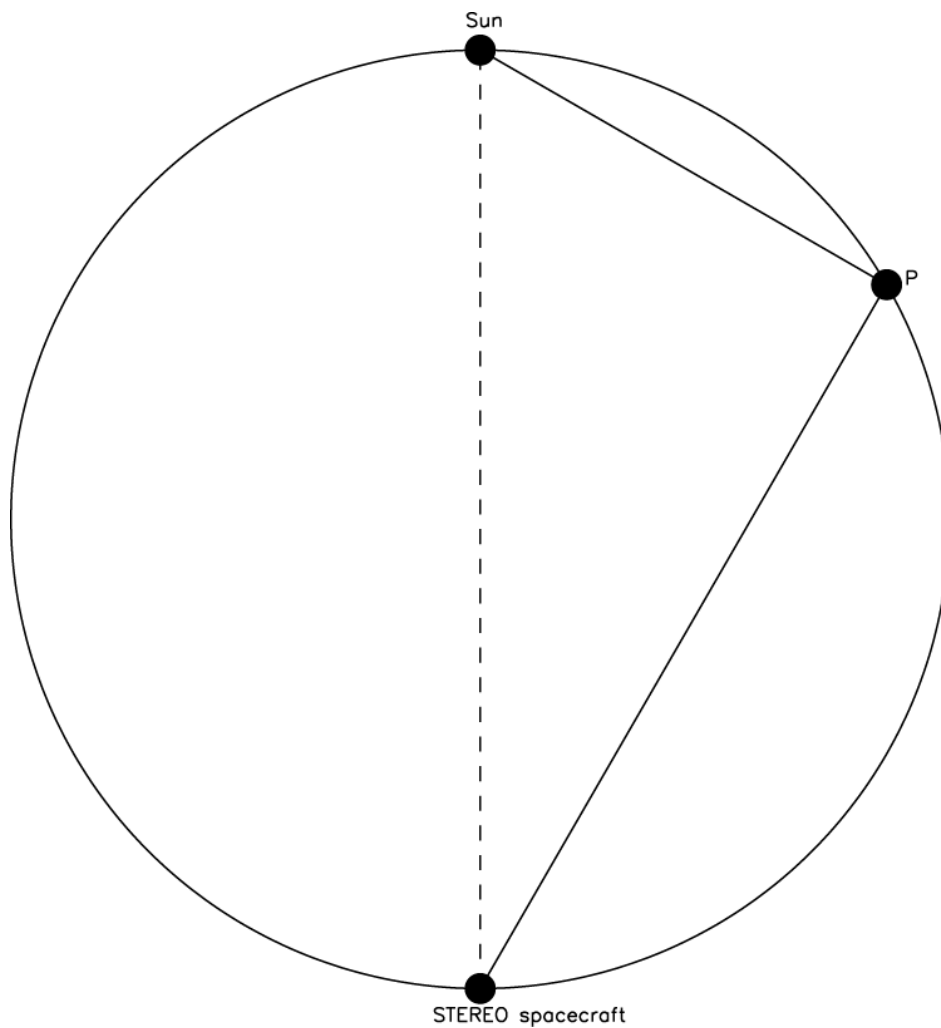


Figure 4.3: A depiction of the Thomson Sphere. The solid circle is the surface of maximum intensity from Thomson scattering. The dashed line shows the diameter and the circle is symmetric about the dashed line to produce the full sphere. The point P is to illustrate that any point on the surface of the sphere has incident light at an angle of 90° to scattered light.

The elongation variation of a solar transient can be analysed to provide unique estimates of its associated V_r and β given a long enough interval of observations. Such analysis has been performed using STEREO HI observations of transients entrained in Corotating Interaction Regions (CIRs) by Rouillard et al. (2008, 2009a, 2010a) and of CMEs by Davies et al. (2009), Davis et al. (2009), Savani et al. (2009), Baker et al. (2009), and Rouillard et al. (2009b). A number of these authors have validated the accuracy of the technique by comparison with in situ measurements by various spacecraft (e.g. including Venus Express or ACE), with ground based observations (e.g. magnetometers), and with solar surface signatures (e.g. by using precise flare locations). The analysis as performed by those authors requires the manual selection of points along the elongation-time profile of an individual transient in a J-map. The selected points are then compared to a suite of elongation variations generated theoretically using equation 4.1 for all physically realistic combinations of V_r and β , in order to obtain a “best-fit” and hence estimate the speed and direction of propagation.

The work presented here aims to assess theoretically this method of recovering the velocity and trajectory of solar transients from their elongation variations using a Monte Carlo simulation approach. In particular, we aim to assess the range of elongations over which it is necessary to make observations in order to accurately recover V_r and β . In doing this we are then able to comment on the usefulness of this method based on single spacecraft STEREO/HI observations in predicting Earth-bound space weather events.

4.2. Observations

The technique of creating time-height maps (J-maps) of coronal data, initially developed by Sheeley et al. (1999) to aid the characterisation of CMEs observed by the LASCO coronagraphs on SOHO, has more recently been applied to observations from the STEREO HI instruments, although with height being substituted by the more appropriate elongation parameter. In essence, the J-mapping technique, as has generally been applied to the HI data, involves plotting the intensity along a fixed solar radial line (usually the ecliptic) from a series of running difference HI-1 and HI-2 images as a function of time on the X-axis and elongation on the Y-axis.

The upper panel of Figure 4.4 combines HI-1 and HI-2 running difference images from 12 July 2007, during the passage of a CME through the HI field-of-view of the STEREO A spacecraft. HI observations of this CME, the launch of which was associated with NOAA Active Region 10963, have previously been presented by Davies et al. (2009). This CME exhibits a typical 3-part morphology, with a hierarchy of overlying loops followed by a density cavity and a subsequent dense, and in this case V-shaped, core. In the difference images, light grey/white areas reveal areas in which the intensity is increased relative to the previous image (corresponding to increased electron density) whereas dark grey/black areas show areas of reduced intensity (reduced density). Note that the visibility of a solar transient will not only be altered by changes in its density but also by its proximity to the Thomson sphere, as will be discussed in more detail later. A mask is applied to the HI-2 image to conceal areas of the field-of-view obscured by the stray-light baffle system and the Earth occulter. The lower panel of Figure 4.4 illustrates a time-elongation (J-) map extending over the entire of July 2007, the month encompassing this CME, produced following the method

described by Davies et al. (2009). The J-map is derived from HI-1 and HI-2 running difference observations along the centre of the combined HI field-of-view on STEREO A, which for this interval of nominal instrument operation corresponded closely to the ecliptic. The elongation range of the J-map extends from 4° , the sunward edge of the in-ecliptic portion of the HI-1 field-of-view, to 74° , a limit placed on observations of the central part of the viewing area by the Earth occulter.

The J-map reveals many inclined tracks, corresponding to antisunward-moving solar transients, which are visible out to different elongations. The clearest track, which enters the HI-1 field-of-view early on 12 July and can be observed propagating antisunward until it finally becomes obscured by the Earth occulter on 17 July, corresponds to the dense core of the CME imaged in the top panel of Figure 4.4. Note the transition between the light leading edge and dark trailing edge results from use of difference images. Preceding this track are fainter tracks corresponding to the overlying loops of the CME front.

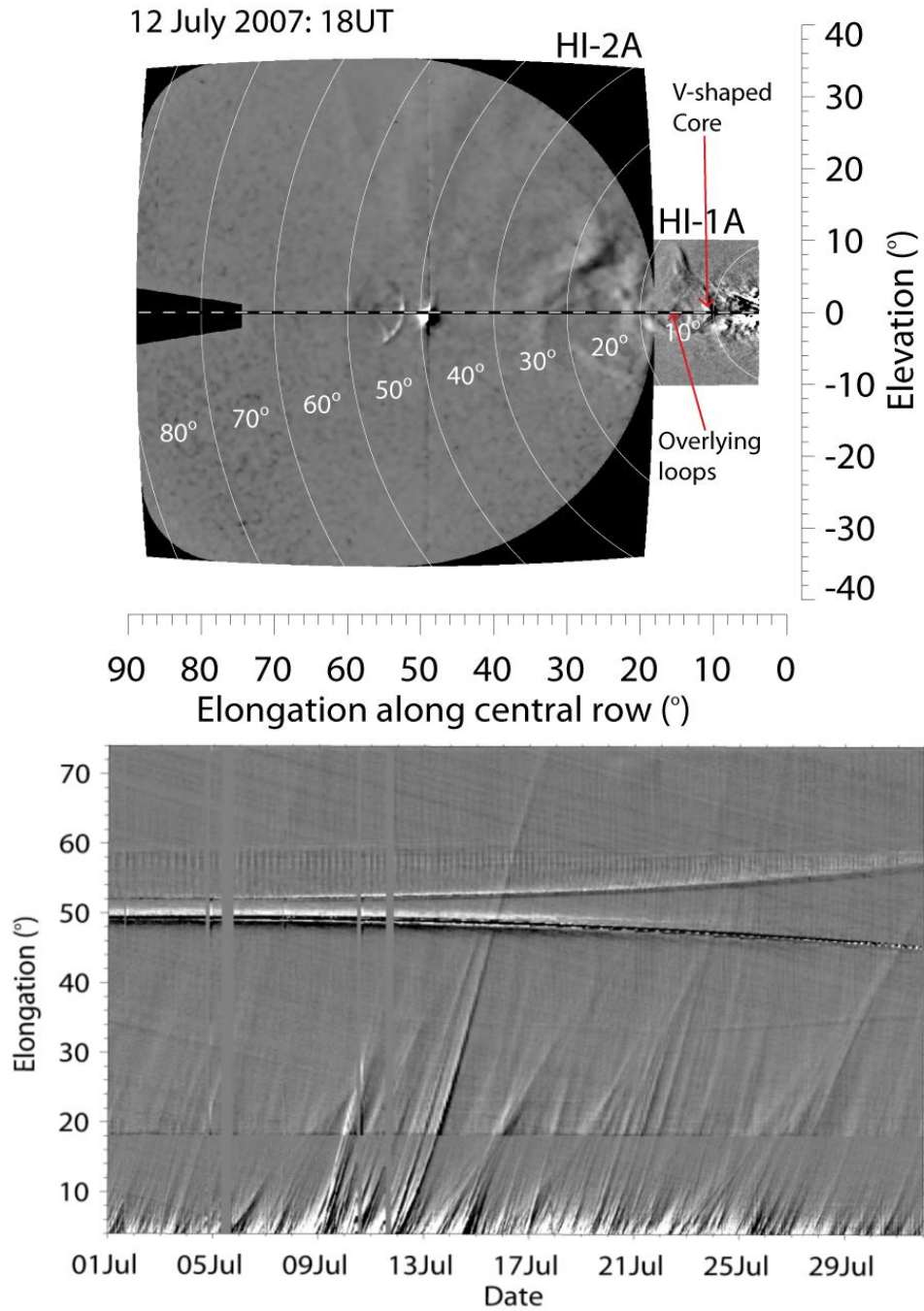


Figure 4.4: The upper panel presents combined differenced images from the HI-1 and HI-2 instruments aboard the STEREO A spacecraft from 18UT on the 12 July 2007. The dashed line corresponds to the ecliptic, along which the J-map shown in the lower panel is produced and the curved lines show contours of constant elongation. The J-map extends over July 2007 and gaps due to missing images are filled in grey. The tracks of many antisunward-moving solar transients can be seen in the J-map.

As stated previously, from the elongation variation of a given solar transient, extracted from such a J-map, it is possible to estimate its radial velocity, V_r , and the angle at which it is propagating relative to the Sun-spacecraft line, β . As noted above, the extraction of the time-elongation variation for a transient has been obtained manually by applying this technique by Davies et al. (2009). Following the method of Rouillard et al. (2008, 2009a), Davies et al. (2009) estimated the CME core to be propagating with a radial velocity of 320 km s^{-1} at a longitude relative to the Sun-STEREO A line of 48° in the ecliptic plane. These values were validated by in-situ and solar surface observations, the latter of which revealed a launch time of 04 UT on the 11 July 2007 in the vicinity of active region 10963. CME activity was also recorded in the STEREO inner and outer coronagraphs and SOHO/LASCO coronagraphs.

The accuracy of the velocity and direction estimates retrieved from fitting the elongation variation will clearly depend on the accuracy with which a specific track can be followed. This is assessed in Figure 4.5, which reproduces that portion of the J-map presented in Figure 4.4, lower panel, extending from 11 to 17 July 2007 and covering the CME passage throughout the STEREO-A HI field of view. Using the CME velocity and longitude quoted by Davies et al. (2009) for the CME core, $V_r=320 \text{ km s}^{-1}$ and $\beta=48^\circ$, its ‘ideal’ elongation variation is calculated from equation 4.1, from an elongation of 4° out to an elongation of 74° with an elongation resolution of 2° . This elongation range reflects the maximum extent to which outward propagating solar transients can be tracked through the HI viewing area in the ecliptic plane. Subsequently, three levels of random noise are added onto this ideal elongation variation, normal distributions with standard deviations of 1° , 2° and 5° , to simulate three different degrees of accuracy with which a user could conceivably trace the ideal curve. These three sets of points are over plotted onto the CME core track in the J-map

as orange, yellow and blue dots marking the sets of points with 1, 2 and 5°, respectively, from the ideal elongation variation of the CME core. By overlaying these three sets of points onto the J-map, it can be seen that selecting points along this transient track with a standard deviation of 2°, and probably even 1°, from the perfect curve, shown in red, is likely to be realistically achievable. It is possible that in the elongation ranges covered by the HI-1 instrument it would be realistic to assume a standard deviation of less than 1° due to the increased resolution compared to the HI-2 images. In the elongation ranges covered by HI-2 it is generally the case that transient events drop off in brightness with increasing elongation. Hence it would be realistic to assume an increasing error with increasing elongation with a maximum error of 2° at larger elongations being a realistic target. Clearly the blue points representing a 5° error would be completely unrealistic for any event quantified by this method.

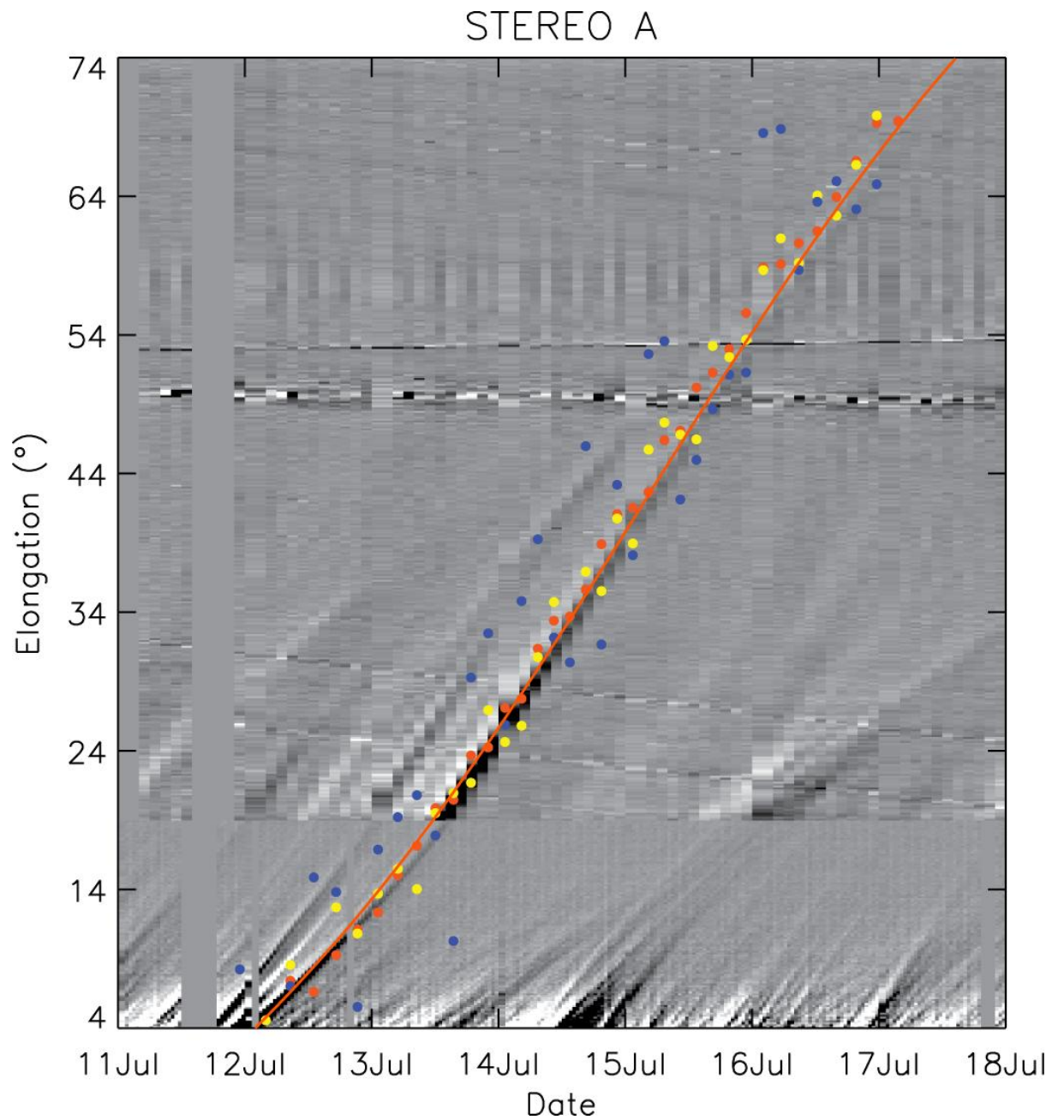


Figure 4.5: A close up view of one of the features seen in Figure 4.4, with three sets of points overlaid simulating three levels of accuracy with which the feature can be tracked. The orange, yellow and blue dots mark sets of normally distributed points with standard deviations of 1° , 2° and 5° , respectively, around those points determined theoretically for a solar transient with $V_r=320 \text{ km s}^{-1}$ and $\beta=48^\circ$.

4.3. Analysis of the 12 July 2007 CME

Clearly the choice of points a user makes in selecting a transient will have a significant effect on the derived parameters V_r and β . As discussed previously, in order to retrieve the values of V_r and β from the elongation variation of a given solar transient, the manually selected points along its track in a J-plot are compared to a suite of elongation variations generated theoretically using equation 4.5 for all physically realistic combinations of V_r and β . As discussed by Rouillard et al. (2010), the best fit is obtained by evaluating σ , the standard deviation of the residuals between the observed elongation variation, $\alpha'(t)$ and a given theoretical elongation variation, $\alpha(t)$ derived from equation 4.5 for a particular combination of V_r and β as shown in equation 4.6.

$$\sigma = \sqrt{\frac{1}{N} \sum_{i=1}^N \{\alpha'(t_i) - \alpha(t_i)\}^2} \quad 4.6.$$

The combination of V_r and β that correspond to the theoretical elongation that gives rise to the best fit defined by the minimum in this parameter σ are then assigned to the transient.

In order to demonstrate more explicitly the effect on the goodness of fit of the level of accuracy with which the user can track this transient, Figure 4.6 plots σ (which we subsequently call the fit error) obtained when fitting each of the three ‘observed’ elongation variations over plotted on the J-map in Figure 4.5, contoured as a function of V_r and β . The top-left, bottom-left and top-right panels of the figure correspond to fitting the elongation variations with random errors of 1° , 2° and 5° standard deviation,

respectively. In each case the fit error is evaluated by comparing the observed elongation variations to theoretical elongation variations computed over a range of V_r values of 0 to 1000 km s⁻¹ (with a resolution of 1 km s⁻¹; y-axis) and a range of β values of 0 to 100° (with a 1° resolution; x-axis). A white star in each panel mark the combination of V_r and β , 320 km s⁻¹ and 48° respectively, from which the three observed elongation variations are subsequently derived. The white diamond marks the V_r and β combination which is calculated to produce the best fit to the observed elongation variation in each case, by virtue of corresponding to the minimum fit error. Each panel also has a white contour line overlaid which marks the region bounded by values of σ equal to twice its minimum value.

It is clear from Figure 4.6 that the parameters corresponding to the best fit (the diamond) are closest to the input parameters (marked with a cross) when the user fit to the transient track is performed most accurately (top-left panel). This results from the much more tightly constrained minimum in the fit error, σ , as is evident by comparing the contours defined by the 2 times σ level. Also, as would be anticipated, the minimum value of the fit error is higher for the tracks with larger random error. For the case of the most poorly defined track (with its points having a random error of 5° standard deviation; top-right panel) the fit error field is highly uniform, so much so that this contour encompasses V_r values from 300 km s⁻¹ to 600 km s⁻¹ and β values from 20° to 100°. It is interesting to note that the form of the fit error field is such that, for this combination of initial parameters at least, it appears that one is likely to be able to determine V_r much more accurately than β . Obviously, as the noise added is random, with only its standard deviation specified, different runs would produce somewhat different results. We will return to this theme later when we adopt a Monte Carlo simulation scheme to compare the accuracy of fitting different extents of the elongation

variation. While this 5° standard deviation is shown mostly for comparison, it emphasises the need for the users to take care in selecting points for fitting.

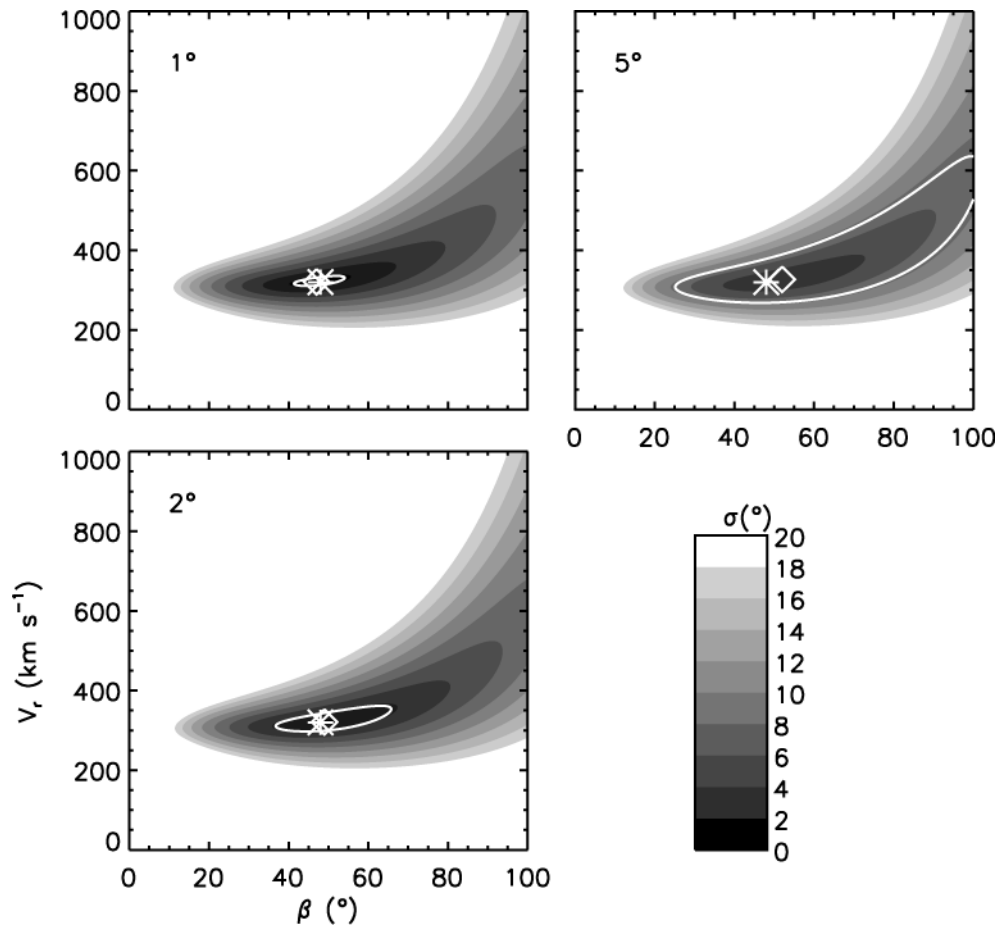


Figure 4.6: Contour plots of the fit errors obtained when fitting elongation variations corresponding to a track defined by $V_r=320 \text{ km s}^{-1}$ and $\beta=48^\circ$ onto which three levels of random error have been added (with 1, 2 and 5° standard deviation – top left, bottom left and top right panels respectively). Darker shades illustrate regions of lower fit errors, lighter shades reveal larger fit errors. The asterisk on each panel marks the input values, while the diamond marks the best fit values. The white contours here indicate a level equal to twice the minimum σ .

Based on Figure 4.5, we decide that it is realistic to assume that a user is capable of selecting a set of points along a typical transient track with a 2° standard deviation in the worst case at elongations greater than 44° , a 1° standard deviation between 24° and 44° , and a 0.5° standard deviation in the range of the HI-1 instrument of 4° to 24° elongation. We examine the effect on the accuracy of the best fit parameters of the extent over which the solar transient can be tracked by the HI instruments. Differences between the points selected by different observers (and indeed a single observer doing multiple fits of the same transient) could also result in a different value of V_r and β for a transient. The results presented here provide a method of determining the quantitative impact this will have on the parameters V_r and β . J-plots such as those shown in Figure 4.4 (lower panel) and Figure 4.5, reveal that only a minority of transients can be tracked over the full range of elongations viewed by HI, 4° to 74° , in the ecliptic plane. As well as the precision with which it is possible to follow the transient signature in a J-plot, it is suggested that the elongation extent over which it can be tracked will also affect the accuracy of retrieving the parameters from the observed elongation variation; this we assess now.

Figure 4.7 presents contour plots of the errors in fitting, similar to those presented in Figure 4.6, but where the elongation profile is fitted over decreasing ranges of elongation 4° to 74° , 4° to 64° , 4° to 54° and 4° to 44° (a-d), 4° to 34° , 4° to 24° and 4° to 14° (e-g). This simulates the effect of this technique of tracking solar transients that are only visible in the HI images to different points in the field of view. As in Figure 4.6 the asterisk and diamond mark the initial input and best fit values, respectively, and a white contour marks the boundary of twice the minimum value of σ . The top-left panel, showing the error map derived from fitting the elongation variation of a solar transient which can be detected over the full extent of both HI cameras, from

4° to 74° , will be similar to the bottom left panel of Figure 4.6, though differences will exist due to the smaller errors used at elongations less than 44° . We define the minimum value of σ as σ_{min} and here we look for the range of V_r and β which have a σ of less than $2\sigma_{min}$. The $2\sigma_{min}$ level here corresponds to a certainty of V_r and β of 95%. The main notable difference is a better certainty in the fit from the $2\sigma_{min}$ level in Figure 4.7. The panels showing fit errors associated with fitting an event seen further than approximately halfway across the HI 2 field of view, panels b-d, potentially give a very good fit. It should be noted that the range of values that form the smallest mean error is slightly larger than when using the full extent of the cameras and this range increases as the visible extent decreases. Panels e-g use a smaller extent covering the HI 1 camera and sunward portion of the HI 2 camera. The result of fitting over shorter elongation extents is clear: rather than a band running across a range of β s and a narrow range of velocities, there is a broader spread that runs from high V_r and small β values to large β and V_r , again as shown by the overlaid white contour lines. The best fit is again marked with a diamond and, in general, the panels (a-e) which use the HI 2 camera have a best fit which is very close to the perfect fit.

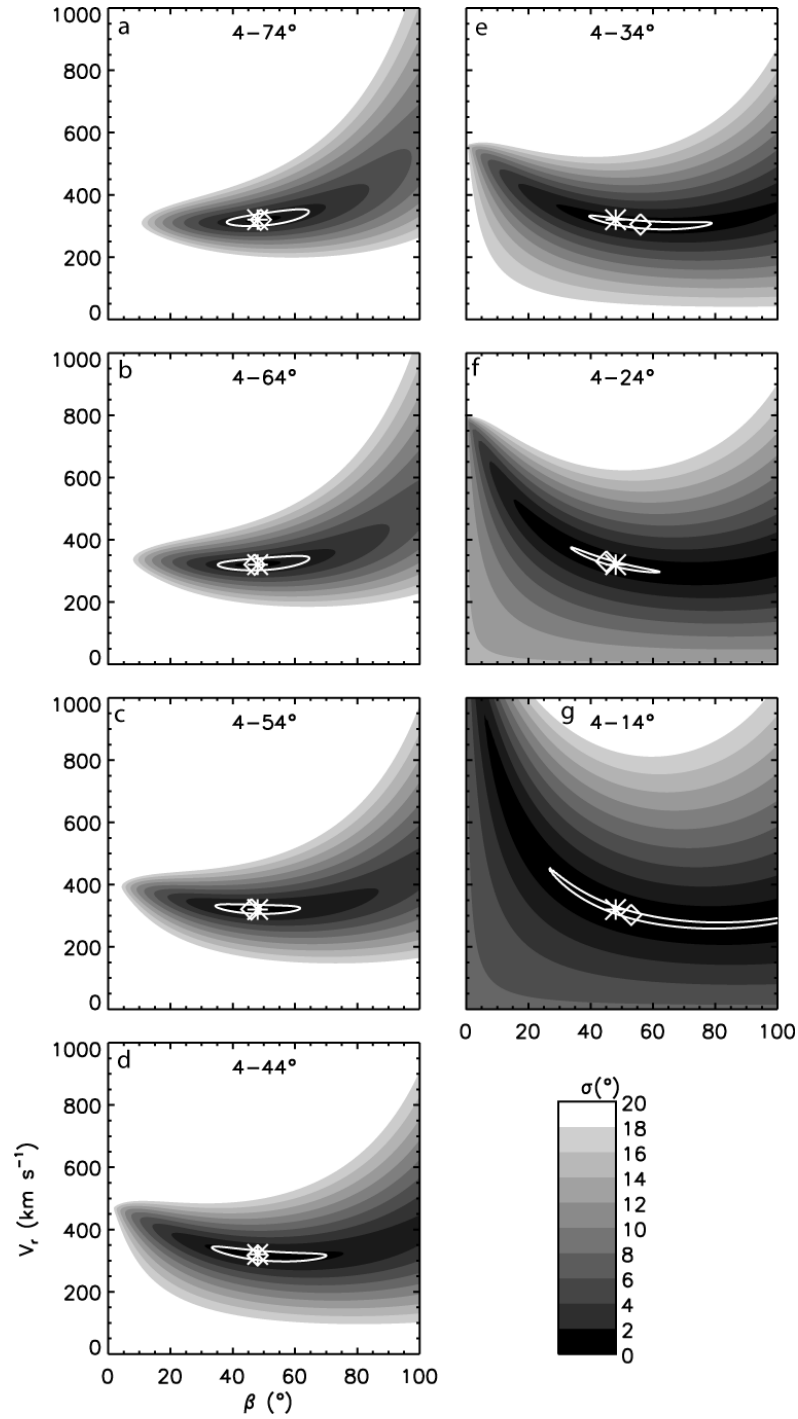


Figure 4.7: Contour plots of the fit errors obtained when fitting decreasing extents of the elongation variation corresponding to a track defined by $V_r=320 \text{ km s}^{-1}$ and $\beta=48^\circ$ onto which a random error has been added as described in the text. In each panel the Asterisk marks the input values, and the diamond marks the best fit values. Each panel corresponds to the elongation range given. The white line marks a contour equal to twice the minimum fit error.

4.4. Monte-Carlo simulations

We have until now looked at the results of fitting an observed elongation variation defined by one pair of input parameters, with a set of normally distributed errors dependent on elongation. As the addition of errors invokes a random number generating technique, it is clear that it can be done many times, with the resultant profile being fitted for each. Thus we use a Monte Carlo method to determine the mean absolute errors between the retrieved V_r and β and the initial values over a range of simulated events. Here, instead of comparing the observed elongation values with the theoretical elongation values, the best fit V_r and β are compared to the input value. Equation 4.6 is used to find σ_{min} and hence the best fit and this is done 1000 times for each input combination. The mean absolute error between the best fit values of V_r and β and the input values (for each combination of the latter) is stored. This is done for a range of input V_r values from 100 km s^{-1} to 900 km s^{-1} in steps of 50 km s^{-1} and a range of β values of 10° to 90° in 5° steps. To simplify matters a 2° standard deviation error is applied to the entire elongation range and the analysis is applied over the same elongation extents as for Figure 4.7. The mean absolute error in V_r , contoured as a function of V_r and β is shown in Figure 4.8. Similarly the mean absolute error in β is shown in Figure 4.9.

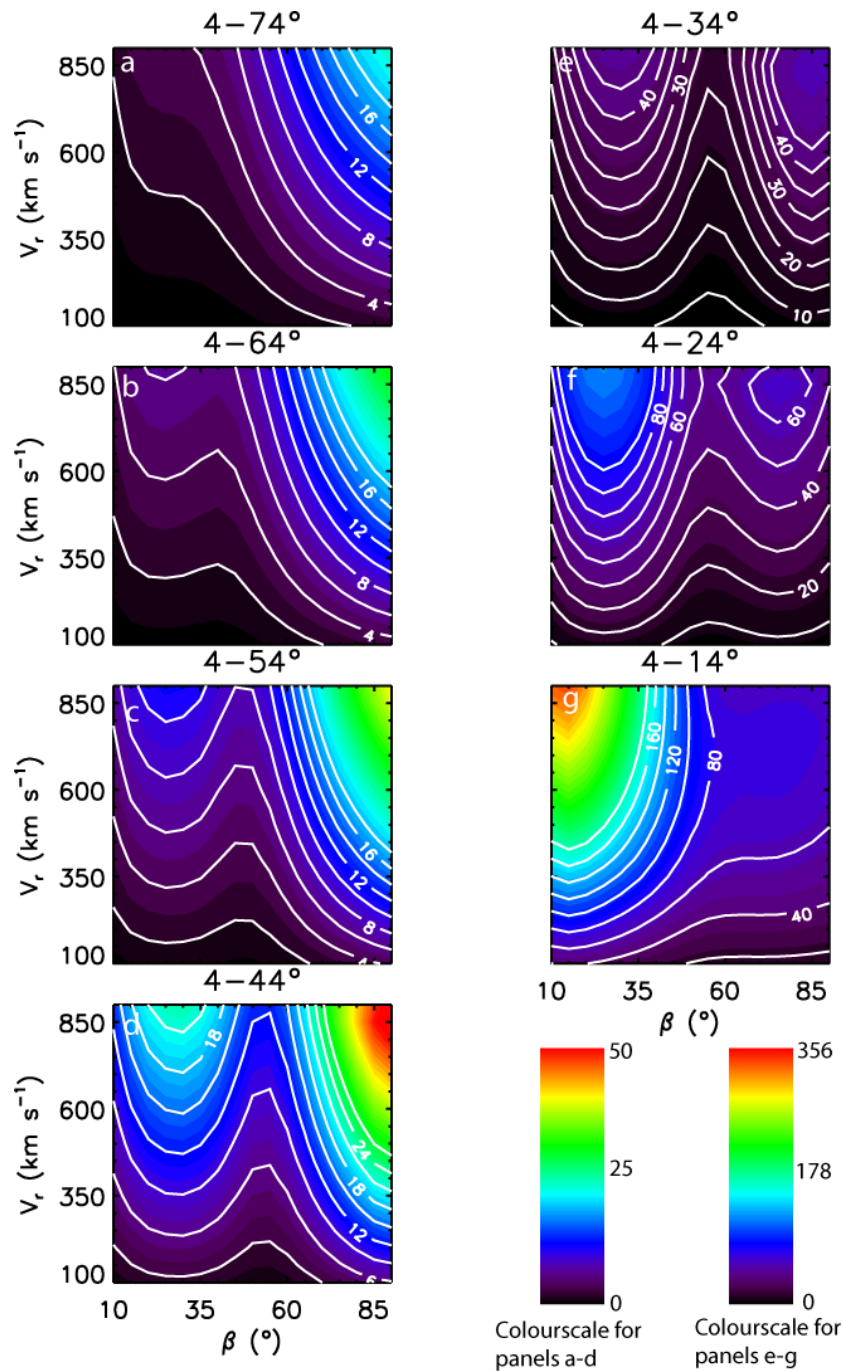


Figure 4.8: Contour plots of the mean absolute error in V_r as a function of V_r and β . Each panel is derived from fitting tracks over the elongation range given. The mean absolute error is colour coded, with black (red) corresponding to small (large) values, and values of the error in km s^{-1} are also marked on the overlaid contours. Note that the panels in the left hand column are on a common colour scale, and those on the right are on a common but different colour scale.

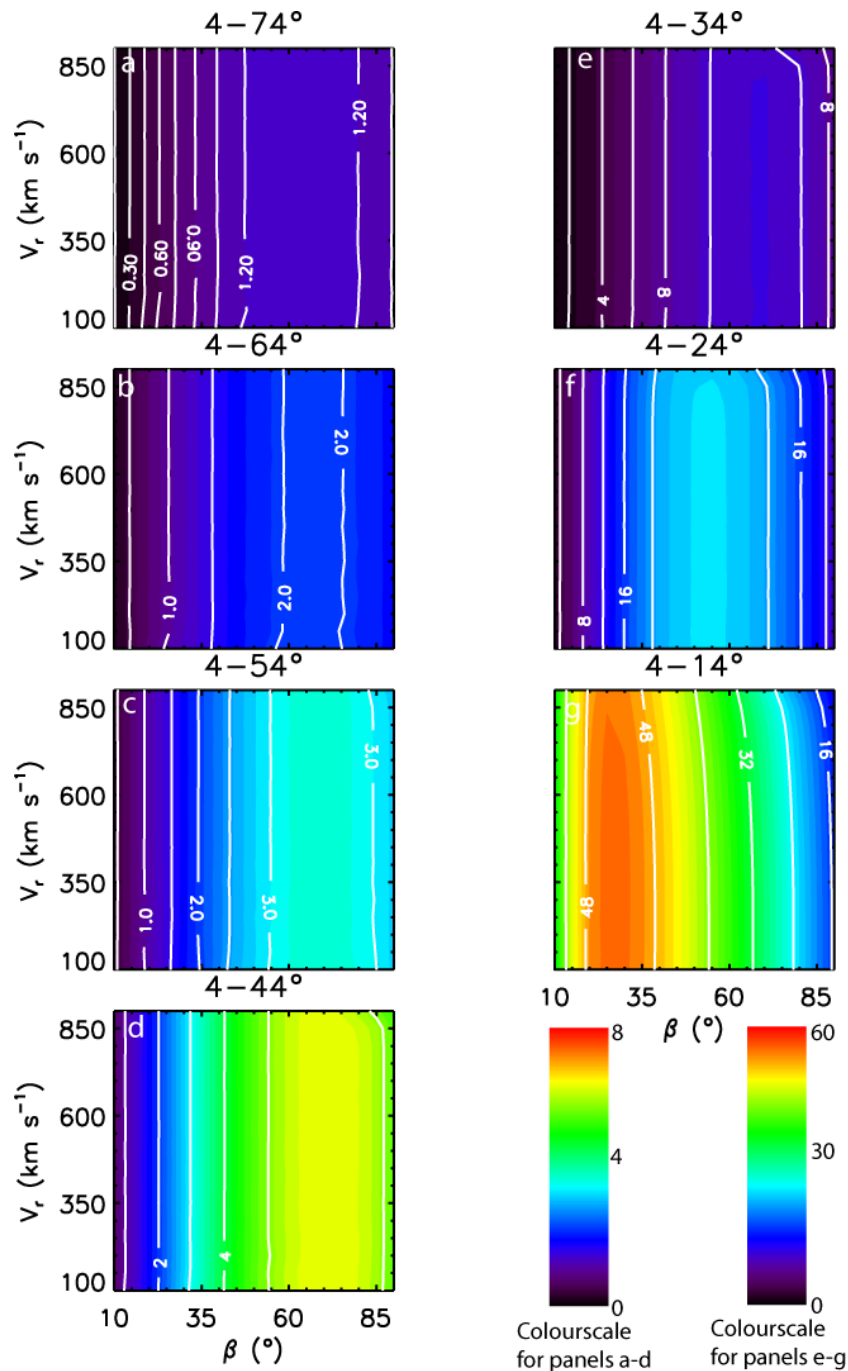


Figure 4.9: Contour plots of the mean absolute error in β as a function of V_r and β . Each panel is derived from fitting tracks over the elongation range given. The mean absolute error is colour coded, with black (red) corresponding to small (large) values, and values of the error in $^\circ$ are also marked on the overlaid contours. Note that the panels in the left hand column are on a common colour scale, and those on the right are on a common but different colour scale.

Figure 4.8 shows in descending order the error in fitting V_r as a function of the input V_r and β for fits to elongations of 4° to 74° (a), 4° to 64° (b), 4° to 54° (c), 4° to 44° (d), 4° to 34° (e), 4° to 24° (f) and 4° to 14° (g). Note that the colour scale in panels a-d is different to the colour scale in panels e-g as shown. Looking at Figure 4.8 as a whole it is interesting to note that the value of β with the smallest error in V_r increases as the elongation range over which the event is fitted decreases. Figure 4.8 appears to show that in all cases, the error in V_r , for any given β , decreases with decreasing V_r . Figure 4.8 also shows two peaks in error present, one at high values of β , 65° and higher, and another at mid-range value of β , 30° to 40° . It can be seen that one peak is normally more prominent than the other and the prominence of one peak over the other is dependent on the visible extent of the event.

Panel a of Figure 4.8 shows the absolute mean error in V_r when the fitting is done over the elongation variation of the full HI field of view, from 4° to 74° , and has smaller values than any of the other panels. Here the smallest errors occur at the smallest values of β , while the largest errors are in the region where $\beta \geq 60^\circ$. Panels b, c and d of Figure 4.8 with maximum elongation extents of 44° to 64° show the errors when fitting out to approximately halfway through the HI-2 field-of-view. The errors here are of the similar magnitude but slightly larger than that in panel a, but the location of minimum error has shifted to the region of $\beta = 50^\circ$ to $\beta = 60^\circ$, while a second region of maximum error forms at lower values of β as previously mentioned. Clearly this shows that the method works best when an event is seen throughout the elongation range of the HI-1 and HI-2 instruments.

Panels e, f and g of Figure 4.8, where fitting is done to a maximum elongation of 34° , show much larger errors than panels a-d. Here, the error is at a minimum in the region of $\beta = 60^\circ$ to $\beta = 70^\circ$ and a maximum in the region $\beta = 30^\circ$ to $\beta = 40^\circ$, while the error

population at larger β values disappears entirely. Clearly this shows that the important part of the fit for smaller values of β occur at larger elongations, whereas for larger values of β the early region of the fit describes the event quite well. Again note the increasing size of the errors with diminishing elongation extent.

Figure 4.9, like Figure 4.8, shows the mean absolute error in β as function of the input V_r and β for fits to the same ranges of elongations as shown in Figure 4.7 and Figure 4.8. Again the colour scale is different in panels e-g and panels a-d as shown. Here, similar to the case for V_r , the smallest errors occur when β is the smallest and, much like the case of V_r , this is true for any given velocity. Unlike the error in V_r , all panels have a similar pattern of near uniform increases in error in β with increasing β .

While the mean absolute error behaves in a similar manner in each panel, the elongation range over which the fit is performed has a much larger effect on the size of the mean absolute error. At large elongation ranges, as in panels a-d, the values for the mean fit error are much lower across the range of V_r and β , while in the elongation range used in panels f and g (4° to 24° , 4° to 14°) the mean fit error is much larger. Compare the maximum errors, $\approx 1.5^\circ$ in the elongation range 4° to 74° with $\approx 25^\circ$ in the elongation range 4° to 24° . This large difference makes accurately identifying the direction of transient events much more difficult when only using the HI-1 instrument.

4.5. Discussion

We have investigated the accuracy of determining the velocity and direction of solar wind transients observed by the STEREO HI instrument. As has been shown, events which are not seen out to a large elongation have a less accurate fit, such as events which are faint in intensity. One factor that will influence the elongation out to which a solar transient can be observed is its direction of propagation relative to the so-called Thomson Sphere (e.g. Vourlidas and Howard, 2006). The Thomson sphere, the surface from which the HI cameras will see the most scatter of light from electrons, is a sphere in which the Sun-Spacecraft line forms a diameter. Solar transients propagating at a large β will move outside the Thomson Sphere at shorter distances from the Sun and this will tend to hinder their visibility to large elongations. Obviously, despite this effect transients with large associated densities, such as those likely to create adverse conditions on Earth will still be seen out to over 40° elongation. Clearly Earth-bound events, which could have detrimental effects on satellite in orbit around the Earth, can be seen and predicted best while the spacecraft are within $40\text{-}50^\circ$ of the Earth. The combinations of this technique with the images used to make up a J-map allow for a good estimate of speed, direction and potentially geo-effectiveness when applied to Earth directed events.

The Thomson Sphere is also going to reduce the visibility of most events that do not pass close to the spacecraft at large elongations. In addition Thomson Sphere effects can change what part of a transient is imaged as it evolves in shape and structure throughout the heliosphere. This effect for wide CMEs, where the leading edge is not necessarily the same as the observed leading edge, has been noted by Webb et al. (2009) and Lugaz et al. (2009). If it is the case that different parts of a CME front are

observed with time it can result in a slightly varying value for β and will obviously result in a different profile in a J-map which is clearly a source of additional error to be aware of when using this technique. However, analysis of planetary-bound events has been undertaken with success, through verification by in-situ measurements, at both Venus (Rouillard et al., 2009b) and Earth (Rouillard et al., 2010a,b) to track a variety of transient events.

It has been shown that the extent to which an event can be seen in the HI cameras has a significant effect on the accuracy of the fit. Indeed the difficulty associated with being sure of the fit has been noted by Savani et al. (2009), where they state that only including data from the HI-1 camera introduces large uncertainties in the fitting results. While this is true for events with a small β , we have shown that for larger β values the error in V_r is approximately the same regardless of the extent to which the event is seen. Obviously the only way to measure the true velocity of an event is through the use of in-situ data and this will only be possible for events that pass over a spacecraft with the instruments to measure the plasma properties. As mentioned previously the analysis method used here assumes discrete plasma points and makes no measurement of the angular size of the event in the ecliptic plane, although this can be estimated if the event can be seen in both STEREO spacecraft. In this case each STEREO spacecraft will image different parts of the same event and so an approximation of the angular size can be made.

The analysis assumes that the event velocity is constant neglecting any acceleration phase that may occur near the Sun or deceleration at larger radial distances. It is assumed that any acceleration occurs before the event enters the field of view. Generally transient events tend to accelerate or decelerate towards the ambient solar wind speed, as shown by Gopalswamy et al. (2000) and Jones et al. (2007) for example.

In addition there is evidence of cases of “late accelerating” transient events reported by Tappin (2006). In both these cases the profile of the transient in a J-map will be altered. These changes will not necessarily be apparent to an observer resulting in an additional error in the estimates of V_r and β . As the profile of an accelerating or decelerating transient event is not governed by equation 4.1 the estimates of V_r and β will have a greater uncertainty. The start of the field of view at 4° elongation corresponds to a minimum distance of $16 R_{sun}$, although this value is dependent on the angle of propagation of the event. For larger β values the minimum distance from the Sun to the field of view of the HI cameras is smallest (see Figure 4.1). This makes the assumption of constant velocity in the HI field of view less likely to be valid for such events. As noted by Savani et al. (2009) and Sheeley et al. (1999), acceleration has generally ceased before the event reaches the C3 coronagraph of the LASCO instrument at a radial distance of approximately $30 R_{sun}$. Conversely for events with a small β the minimum distance between the Sun and the HI field of view is larger and so the assumption of constant velocity is more likely to be valid provided that the transient velocity is not significantly larger than the ambient solar wind speed when deceleration effects may play an important role. Interestingly when an event is only seen out to small elongations the area with the smallest error in velocity is that of high β and low velocity. As these are the most likely to still be in the acceleration phase this could be seen as a possible false result and events which fall into this category should be examined carefully. This combined with the relatively high errors associated with high values of β due to the fitting method makes these events harder to accurately parameterize. The additional errors associated with the assumptions of the method as described could result in an error on the values of V_r and β that is comparable to the

error examined here and users should be aware of this when applying this method to the analysis of transient events using J-maps.

The method examined here uses observations from only one of the STEREO spacecraft. From this a direction can be obtained for the propagation of transient events, although an elongation range extending over 40° is required for an accurate fit. Although observations from one spacecraft are insufficient to determine the longitudinal extent of a transient event, this method still allows an estimate of the direction which can then be used to estimate if the event will impact on the near-Earth environment. Given STEREO's capability to observe an event from multiple angles and so estimate the longitudinal size it should then be possible to improve the estimate of the likelihood of impact on the near-Earth environment. Other methods which make use of CME models and observations from the coronagraphs on the STEREO spacecraft such as by Thernisien et al. (2009), de Koning et al. (2009) and Maloney et al. (2009) can also provide an estimate of the longitudinal size of a transient and the J-plot technique could complement the work done by these authors.

4.6. Conclusions

The HI cameras on the STEREO spacecraft have the potential to be a powerful predictive tool for Space Weather. We have shown that the manual selection of points must be done with care to ensure the best fit to an elongation profile for any given transient event. We have also shown how the extent in the HI instruments to which a transient event is seen affects the accuracy of the resulting fit. This allows for the velocity and direction of an event to be stated with a statistical confidence for the

method examined here. Finally we demonstrated how the mean fit error varies for different values of V_r and β , finding that, in general, the error in V_r increases with velocity for any given β , although there are some differences when events are fitted out to different elongations. We also found that, in general, the error in β increases with β for any given V_r and that unlike the error in V_r the main difference here between events fitted out to different elongations was the size of the error. Hence we conclude that to accurately predict when Earth-bound events will arrive at 1 AU the event must first be seen out to an elongation well into the HI-2 camera range. The beacon data sent from the STEREO spacecraft could be used to provide the range required and allow some warning for events which could strike the near-Earth environment. Ideally the event should be seen out to a minimum of 40° , although the further it can be seen the better the measurement of velocity and direction can be. Clearly if this is to be used in a space weather prediction context then a compromise must be reached between accuracy and allowing sufficient time to give a useful warning.

5. Tracking CIRs from the Sun through to the orbit of Mars using ACE, MEX, VEX and STEREO

5.1. Introduction

Solar wind transients, enhancements in solar wind velocity and/or density, often have effects on planetary magnetospheres that are of great interest. These events are sporadic in nature and difficult to predict. However it is hoped that once they are first observed close to the Sun they can then be tracked through the solar system and their arrival at the planets predicted. During the recent solar minimum of 2007/8, observations of a number of CIRs have been reported (e.g. Mason et al., 2009) and these form the focus of this study. CIRs are regions of enhanced density formed at the interface between a fast solar wind stream catching up with a preceding slower solar wind stream. As this interface rotates with the Sun the high speed stream sweeps out a large swath in heliospheric longitude and the CIR assumes the shape of an Archimedian spiral, similar to the Parker spiral of the interplanetary magnetic field (Gosling and Pizzo, 1999). CIRs are characterised in in-situ measurements by a peak in plasma density followed by an increase in solar wind speed and plasma temperature. One of the objectives of the STEREO spacecraft, and more specifically the HI instruments, is to trace the visible evolution of CMEs through the inner heliosphere. Due to the solar minimum conditions in which it has been operating it has also been possible to study the evolution of CIRs through the inner heliosphere using STEREO/HI (Rouillard et al., 2008, 2009a; Sheeley et al., 2008a,b; Tappin and Howard, 2009; Wood et al., 2010). As previously mentioned the impact of transient solar wind events is often of great

interest to observers of planetary magnetospheres. For example, solar wind transients are responsible for producing geomagnetic storms at Earth(Cliver, 2006; Milan et al., 2009), and have a demonstrable effect on other solar system bodies including Mars. At Earth the direction of the interplanetary magnetic field (IMF) as well as the dynamic pressure has an effect on the magnetosphere, whereas at Mars, pressure pulses in the solar wind have been observed to increase the outflow of atmospheric heavy ions by a factor of 2.5 (Edberg et al., 2010), and at Venus, ICMEs have also been observed to increase atmospheric ion loss(Luhmann et al., 2008b). The role of the IMF in determining disturbances at Mars and Venus is less clear as these planets do not possess intrinsic magnetospheres. Prediction of the arrival times of solar wind transients at points of interest would be of great use to observers for estimating solar wind conditions if in-situ measurements are unavailable. To this end, in this study we track CIRs through the inner heliosphere based on in-situ and imaging observations from spacecraft situated throughout the inner solar system and then predict their arrival at different planetary bodies and spacecraft based on this information.

5.2. The ACE, VEX and MEX instruments

In this chapter we also present in-situ measurements from the Solar Wind Electron Proton and Alpha Monitor (SWEPAM) (McComas et al., 1998) and magnetic field (MAG) (Smith et al., 1998) instruments aboard the Advanced Composition Explorer (ACE) spacecraft. ACE is in a Lissajous orbit around the L1 Lagrange point, approximately 1.5 million km upstream of the Earth in the solar wind. This enables it to take continuous measurements of the upstream solar wind. We also present observations from the Electron Sensor (ELS) and Ion Mass Analyzer (IMA)

components of the Analyzer of Space Plasma and Energetic Atoms 3 and 4 (ASPERA-3 and ASPERA-4) instruments on board Mars Express (MEX) (Barabash et al., 2006) and Venus Express (VEX) (Barabash et al., 2007), respectively. ELS within ASPERA-3 (ASPERA-4) measures electrons in the energy range 1 eV-20 keV (1 eV-15 keV) with a field of view of 4° by 360° (10° by 360°) and a time resolution of 4 s (32 s). IMA within ASPERA-3 and ASPERA-4 measures ions in 32 mass rings and 16 radial sectors over energies from 10 eV to 30 keV in 96 logarithmically equidistant steps. It then sweeps over polar angles from -45° to $+45^\circ$ in 16 steps, with the whole process taking 192 s. The orbit of VEX is elliptical in such a way that it only spends a limited time of each orbit within the exosphere of Venus and for the majority of its orbit it is in the solar wind. ASPERA-4 mainly makes observations near perigee when VEX is within the exosphere; this contributes to the apparent gaps in the ELS data we present here. The orbit of MEX is also elliptical with a period of 6.7 hours. Like VEX at Venus, MEX only spends a limited time within the exosphere of Mars. However unlike VEX the ASPERA-3 instrument continues to take observations when MEX is in the solar wind.

5.3. Method

The plasma and magnetic field data from ACE for the period 1st July 2007 to 31st August 2008 were searched for signatures of CIRs. The signatures we used were regions of high solar wind density, greater than $15 \text{ protons cm}^{-3}$, immediately followed by regions of increased solar wind speed, increasing by a factor of 1.3 or more over a 24 hour period, and increased magnetic field strength, here increasing to over 8 nT. These signatures were then confirmed by visual inspection to ensure that they were

clearly CIRs and other transient structures such as CMEs were removed. A time of arrival was chosen that corresponded to the time of the first peak in density in the compressed region checked against the CIR list presented by Mason et al. (2009).

Upon finding a signature which could clearly be identified as a CIR, we found the arithmetic mean velocity from the maximum of the high speed stream following the CIR and the minimum of the low speed stream preceding it and took this as being representative of the radial velocity of the CIR, V_r . We assumed that the adjacent sources of fast and slow solar wind would continue to emit coronal plasma at these same velocities. Using this assumption, we can use the following equation to calculate the expected travel time, Δt , from the observation of the CIR at the ACE spacecraft to its impact at a planetary body or another spacecraft at a different location based on the method used by Vennerstrom et al. (2003):

$$\Delta t = \frac{\Delta r}{V_r} + \frac{\Delta \beta}{\omega_{Sun}} \quad 5.1.$$

where Δr is the radial distance between the two bodies of interest, which is assumed constant for the duration taken for the CIR to propagate between the two points, and $\Delta \beta$ is the angle between the two bodies in terms of solar longitude, again assumed to be constant for the duration of the event. Here ω_{Sun} is the equatorial rotation rate of the Sun, approximately $14.4^\circ \text{ day}^{-1}$, equivalent to a complete solar rotation every 25 days. Using equation 5.1 and knowledge of the time of observation of the CIR at ACE we are able to calculate an approximate arrival time of the CIR at Venus, Mars, and locally at STEREO A and STEREO B. Clearly this will not be the same plasma as observed at ACE, unless there is radial alignment, but plasma that is part of the same overall CIR front. We used these estimated arrival times to look for signs of CIR impact at Venus and Mars. Here we use two signatures which could indicate the arrival of a CIR. The

first is an increased differential energy flux in the ELS instruments on MEX and VEX, which has previously been attributed to increased electron fluxes observed in the magnetosheath due to the arrival of a solar wind pressure pulse at Mars (Edberg et al., 2010). Secondly, we can monitor the solar wind speed more directly by examining the energy of the ion beam summed over all anodes of the IMA instrument on VEX and MEX. For this we use the IMA extra data as it is the best quality available. When an increase in the beam energy is seen outside of the planetary exosphere we interpret this as an increase in the solar wind plasma speed, indicative of the arrival of a CIR. The former method is primarily used for observations by MEX and is supported by the latter method, while observations by VEX are much clearer with the IMA instrument so the latter method is preferred.

We also compared in-situ observations from STEREO A and STEREO B with CIR observations from ACE using equation 5.1 to obtain an expected time of CIR impact at each spacecraft, as was done with MEX and VEX. The observations from STEREO A and STEREO B are more directly comparable with those from ACE. To obtain the observed times of arrival at STEREO A and STEREO B we compared the solar wind velocity profiles from each spacecraft using the computed cross-correlation function to obtain a time lag which best aligned the profiles from ACE with STEREO A or STEREO B.

In addition, we used observations from the HI cameras aboard STEREO to aid our study of the propagation of CIRs from the Sun through to the orbit of Mars, Venus, STEREO A and STEREO B. To do this we have used the technique of creating time-elongation (J-)maps, first used by Sheeley et al. (1999) with the LASCO instrument onboard SOHO and subsequently applied to the STEREO/HI observations by authors such as Rouillard et al. (2008), Davies et al. (2009) and Savani et al. (2009) as

explained in chapter 4. Features visible in Figure 5.1 include the passage of Mercury through the field of view, starting at approximately 10° elongation at the start of September and progressing through to approximately 25° elongation at the end of September. Also visible are the tracks of background stars not fully removed in image processing and differencing which have a negative gradient and appear due to the motion of the spacecraft in its orbit. Finally there are some data gaps which are visible as vertical gray areas, most visible on the 25th September. Figure 5.1 shows two clear converging families of tracks, the first entering the HI field of view between the 8th September and 12th September and the second entering the HI field of view between the 17th September and 19th September. Such converging families of tracks are characteristic signatures of CIRs in HI observations, and correspond to plasma elements that have been emitted by the same (rotating) source region at different times and have been entrained at the stream interface (Rouillard et al., 2009b). Note these tracks only converge in J-maps from STEREO A; in STEREO B the family of tracks associated with a CIR diverge (Rouillard et al., 2008). From the track of a given solar transient we can deduce its speed and direction of propagation as shown in chapter 4 with equation 4.5.

By fitting the elongation profile for each track with equation 4.5 we have built up a database of transient events each with a velocity, V_r , and direction of propagation, β . If we assume that each of these tracks is associated with a plasma parcel which forms part of a CIR, then we are able to calculate arrival times at Venus, Earth and Mars using equation 5.1, substituting the appropriate values of velocity and propagation angle. For each of the CIRs identified in the ACE in-situ observations we selected the most identifiable tracks and fitted them using equation 4.5. Of these tracks we are most interested in those which are observed to propagate to elongations greater than 30° as

demonstrated in chapter 4 which showed that these tracks produce estimates with smaller errors on velocity and direction of propagation. For example we were able to select 3 tracks clearly from the CIR between the 8th and 12th September in Figure 5.1 and fit those using equation 4.5. The results of this fitting are shown in table 5.1. When using these to calculate the arrival times at other solar system objects we used the mean velocity from all tracks identified and took the starting point to be the track closest to the Sun-Earth line along with the associated start date and time.

Start Date and Time	Speed (km s⁻¹)	Angle relative to Sun-Earth Line (°)
08/09/2007 15:29	208	-60
09/09/2007 09:29	207	-48
10/09/2007 20:49	235	-35

Table 5.1: Summary of the results of three tracks from plasma blobs within a CIR seen in the STEREO A/HI between the 8th September and 12th September. The negative angle indicates that the angle is westward of the Sun-Earth line.

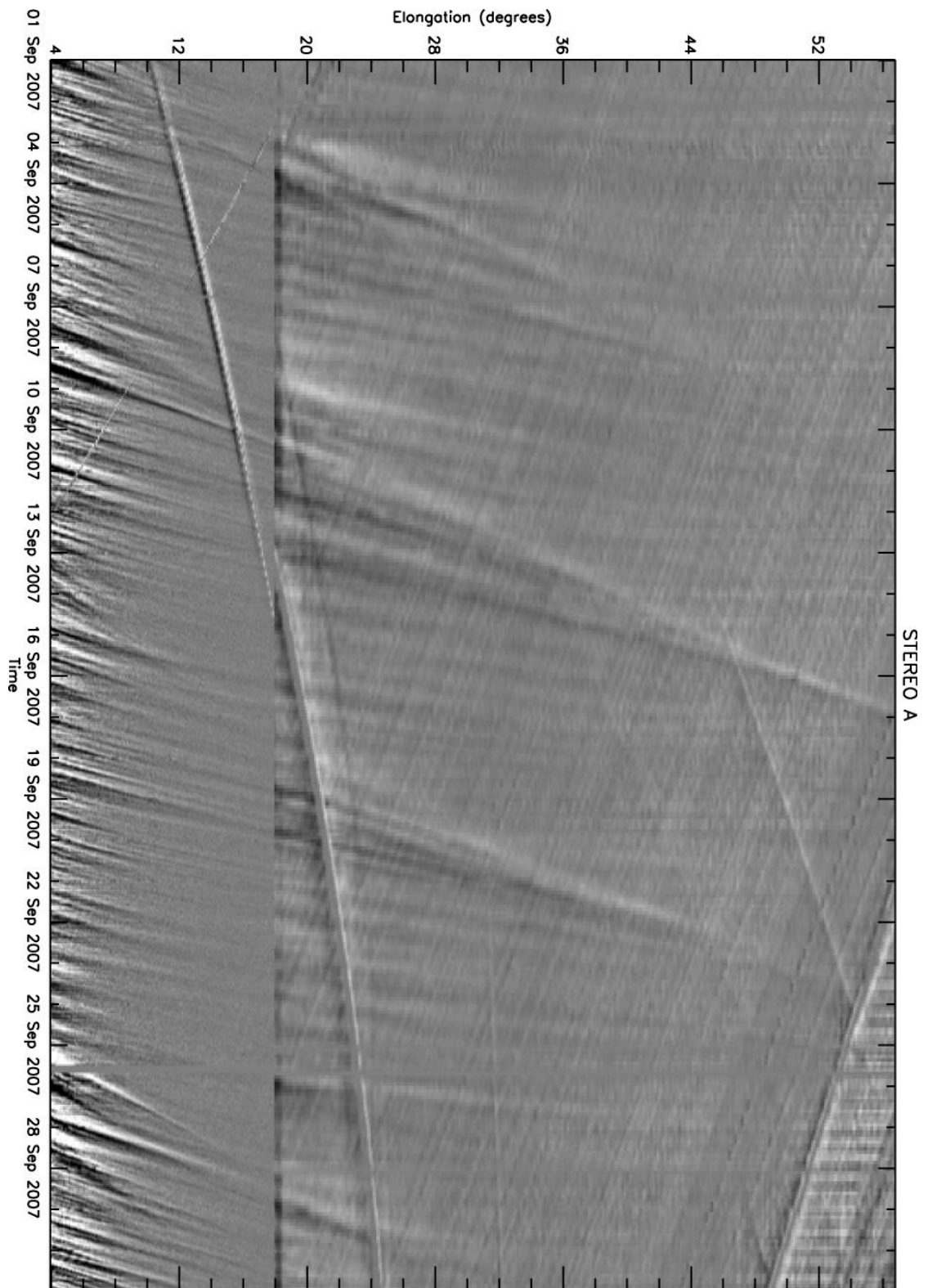


Figure 5.1: A typical J-plot along the ecliptic for September 2007 from STEREO A. The overlap of the HI cameras is clearly visible at 18° elongation. The tracks in the periods from 8 to 12 September 2007 and 17 to 19 September 2007 are typical of a CIR whereby the Sun emits plasma at different times as it rotates.

5.4. Observations

Using the methods of calculating arrival times outlined above we have examined the period from 1 July 2007 to 31 August 2008 and determined the velocities of 24 CIRs as observed by ACE. These events were selected to match times with good coverage of MEX data and where the signature at ACE was clearly of a CIR. Events which were not clearly CIRs were not selected. For each of these events we looked for corresponding signatures in the data from VEX and MEX, and for observations of the groups of tracks in STEREO/HI, at the times expected based on the CIR times derived from ACE observation, using equation 5.1. Although we assume that the front of a CIR is an Archimedian spiral in shape we assume that the individual blobs within the CIR can be modelled as in equation 5.2. As an example we present here a detailed study of one of these CIRs observed by ACE on the 5 January 2008 at approximately 00:30 UT. Figure 5.2 shows plasma data from instruments on MEX (panel v), VEX (panel i), ACE (panel iii), STEREO A (panel iv) and STEREO B (panel ii). We present the plasma density (green line) and speed (black line) and magnetic field (red line) from the SWEPAM and MAG instruments aboard ACE at L1 (Figure 5.2 panel iii). For Venus and Mars we present energy spectrograms from the ELS and IMA instruments on VEX and MEX spacecraft. At STEREO A and STEREO B we present plasma density (green line) and bulk speed (black line) observations from the PLASTIC instrument and magnetic field magnitudes (red line) from the magnetometer instrument in the IMPACT package. Using the mean of the minimum and maximum speed of the CIR observed by ACE gives V_r of 389 km s^{-1} . Using this value, from equation 5.1 we obtained estimated times of arrival of 9 January 2008 at 09:35 UT at Venus and 7 January 2008 at 03:26 UT at Mars. Similarly, expected arrival times of 6 January 2008 at 13:58 UT at STEREO A and 3 January 2008 at 07:12 UT at STEREO B were derived. Overlaid on Figure 5.2 are

red lines indicating the observed arrival time of the CIR at each spacecraft, and black lines indicating the expected arrival times at the four other spacecraft derived from the CIR arrival time at ACE.

We used the speed in a simple model of the Parker Spiral to confirm arrival times at each planet as shown in Figure 5.3. Figure 5.3 shows 5 CIR fronts produced by the model, each spiral shows the expected location of the plasma density enhancement for the indicated time in days, where $t=0$ is the arrival time at ACE. Assuming a constant V_r of 389 km s^{-1} , the expected location of the CIR front at STEREO A ($t=1.54$ days), STEREO B ($t=-1.29$), Mars ($t=1.94$) and Venus ($t=5.03$) is shown.

Although the observations from VEX/ASPERA-4 and MEX/ASPERA-3 are not directly comparable with the ACE observations, we can identify CIR impact at these spacecraft using the two methods previously described. For VEX/ASPERA-4 this is approximately 10 January 2008 at 02:00 UT, and for MEX/ASPERA-3 this is approximately 6 January 2008 at 23:00 UT (red lines). These differ from the expected arrival times (black lines) by 16 hours and 4 hours for VEX and MEX respectively. For clarity Figure 5.4 shows the period from 9 January to 11 January 2008 for the VEX/ELS and IMA observations. Here we can more clearly see the increase in speed of the solar wind through the increased energy of the ion beam. This shows an enhancement similar to that seen in the MEX/ELS but of much shorter duration. Reasons for this are discussed in section 5.5. These enhancements in MEX/ELS have been shown to correspond to periods of increased ion outflow from the atmosphere of Mars (Edberg et al., 2010) compared to periods when no CIR is present.

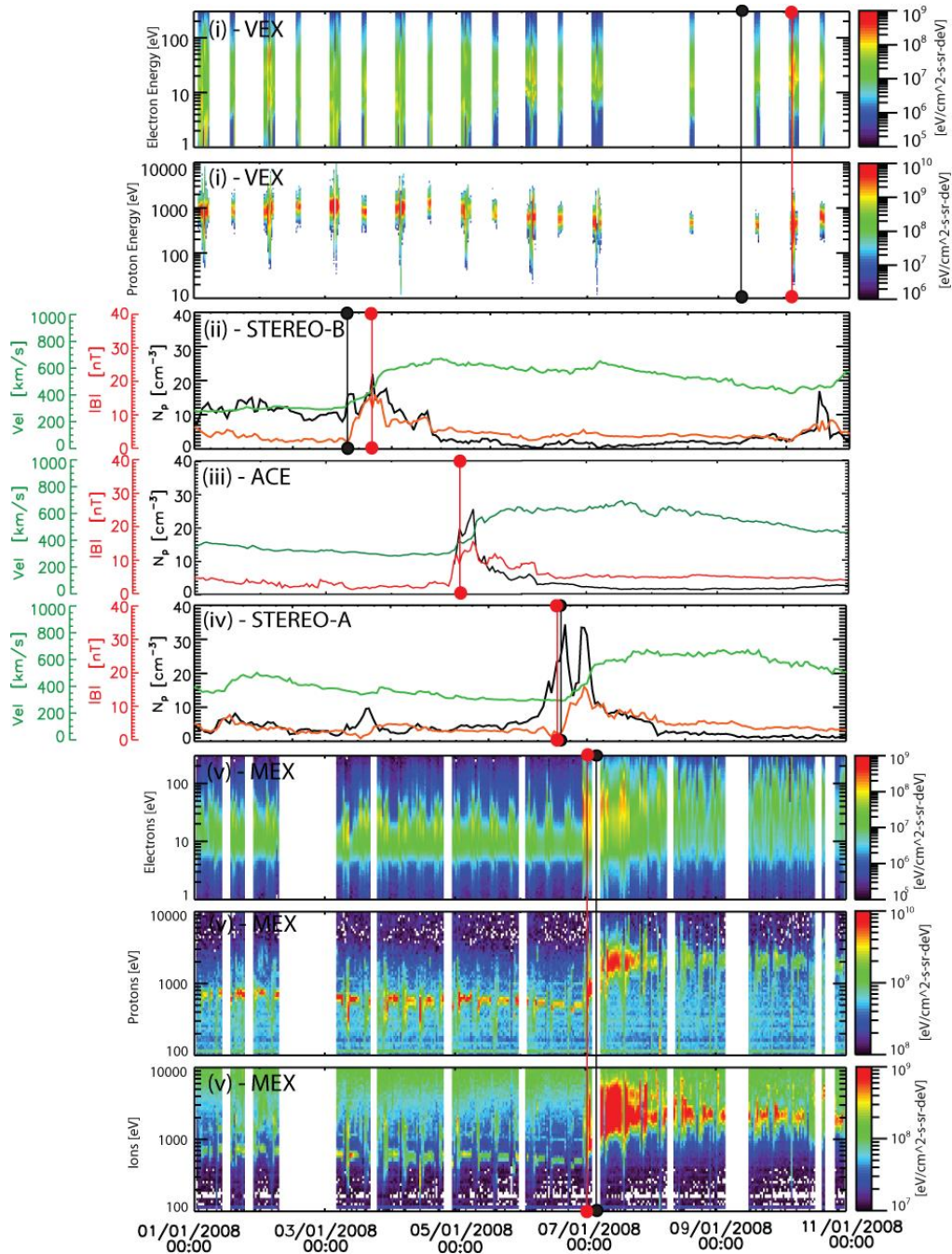


Figure 5.2: Time series plots of (i) Venus Express ELS and IMA data, (ii) STEREO-B plasma and magnetometer observations, (iii) ACE plasma and magnetometer observations, (iv) STEREO-A plasma and magnetometer observations, and (v) Mars Express ELS and IMA data (including the IMA “extra” data) for the period 1-11 January 2008. The observed arrival time is marked as a solid red vertical line, while the expected arrival time from the observation at ACE is marked as a solid black vertical line.

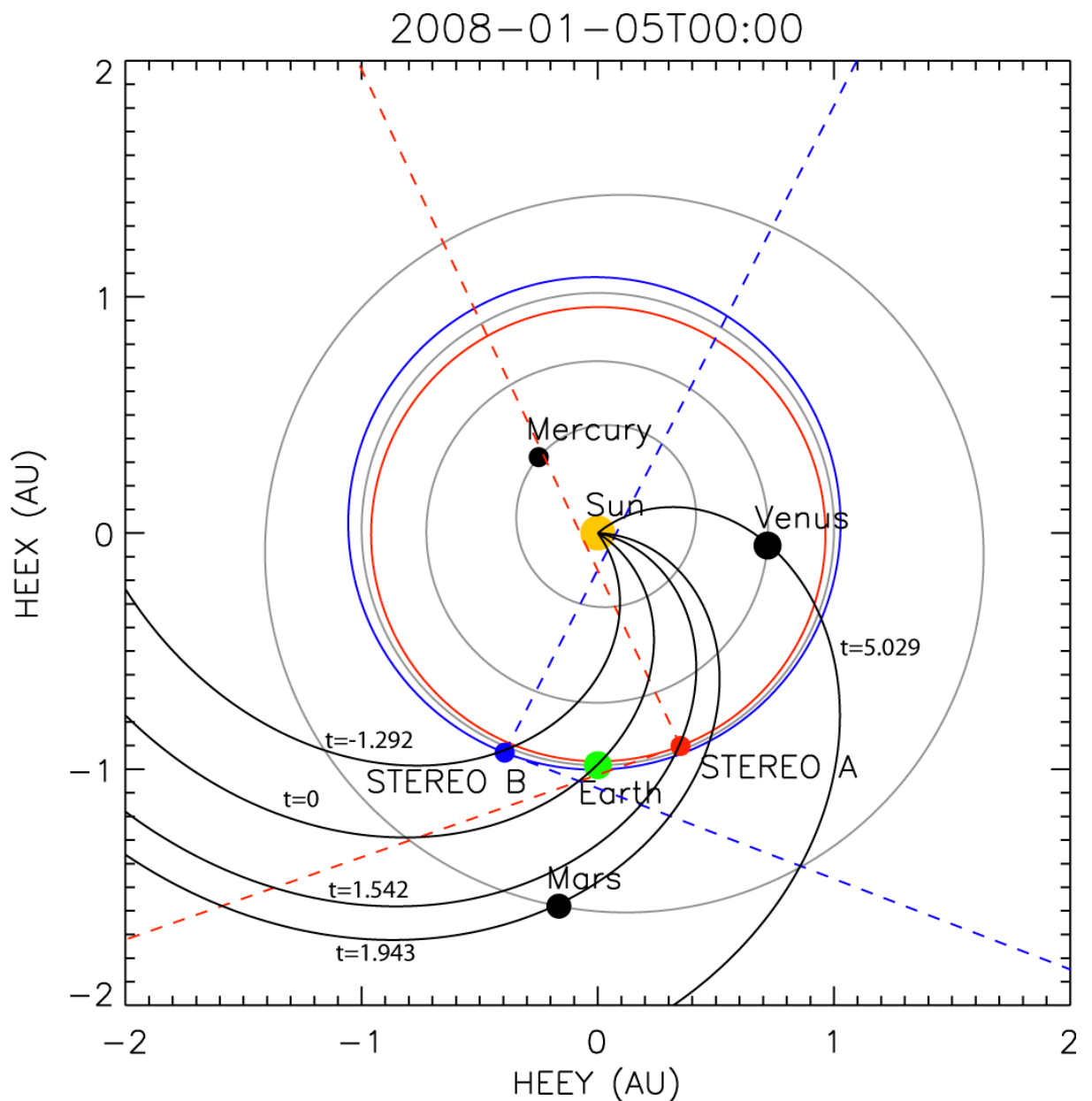


Figure 5.3: The location of the inner planets and STEREO A (red) and STEREO B (blue) on 5 January 2008, 00:00 UT, with the fields of view of the HI instruments marked as dashed lines. There are 5 spirals marked. The first at $t=0$ days represents the approximate Parker spiral associated with a transient which passes over Earth. All other spirals are the location of the CIR front as it passes over other bodies with values of t given in days with respect to the time from when the spiral is at Earth. Each spiral uses a velocity of 389 km s^{-1} to determine the shape.

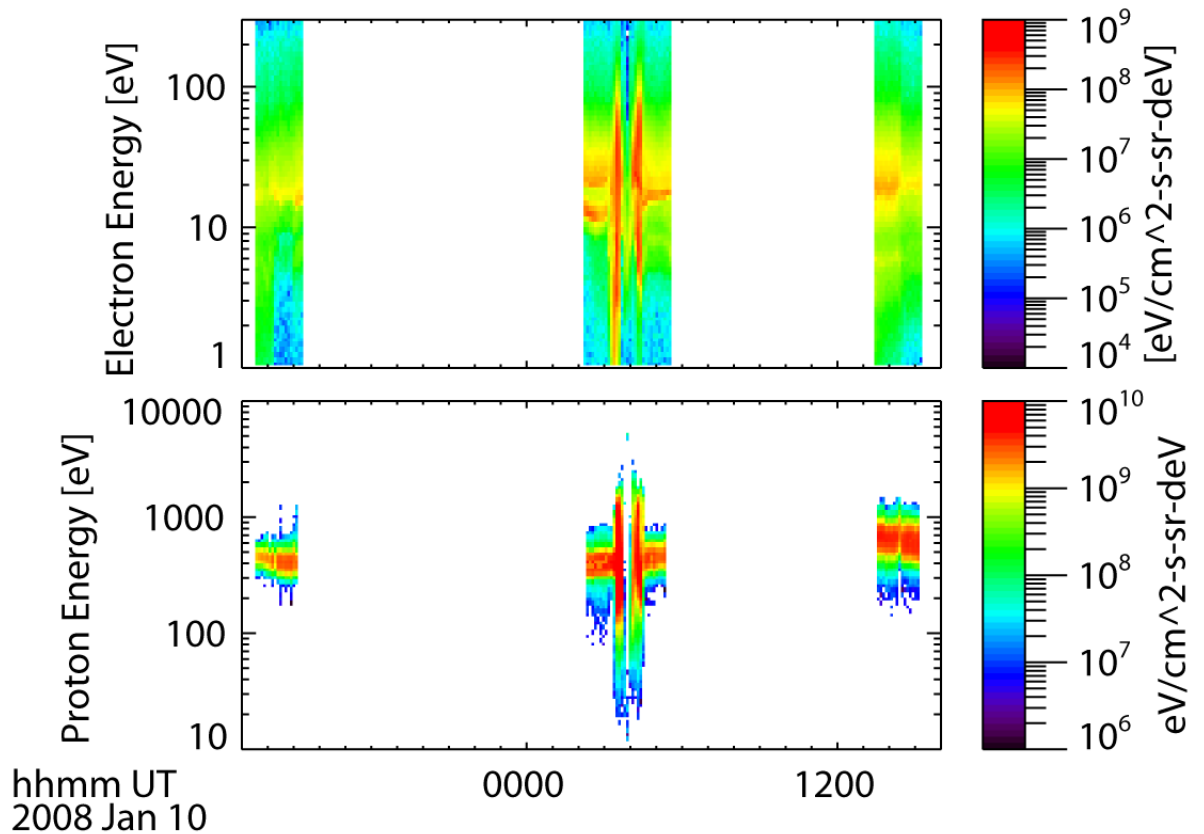


Figure 5.4: Expanded section of the Venus Express ELS and IMA data from Figure 2 showing the enhanced electron energies from 9 to 11 January 2008. The top panel shows an increase in the energy of the main electron beam. The bottom panel shows a slight increase in the ion beam energy indicating an increase in the solar wind speed.

As mentioned in the previous section we used a cross-correlation of the velocity profiles to find the actual CIR arrival times at STEREO A and STEREO B. For the example shown in Figure 5.2 the arrival times from this method are 6 January 2008 at 13:30 UT for STEREO A and 3 January 2008 at 17:30 UT for STEREO B with cross-correlation values of 0.87 and 0.64 respectively. These differ from the expected arrival times by approximately 30 mins and 10 hours for STEREO A and STEREO B respectively. Although in the case of STEREO B visual inspection of the observations indicate a density enhancement and velocity increase starting at the expected arrival

time. The lower value of the peak cross-correlation coefficient indicates a larger error on the timing is to be expected. It also indicates that the signature is somewhat different which indicates a potential error in our initial assumptions.

As previously mentioned, we applied this technique to 24 CIRs and found in the majority of cases good correlation between estimated arrival times and observed arrival times. Figure 5.5 shows a sample interval (5 July 2007 to 5 August 2007) with several CIRs. Overlaid are boxes marking the observed event (blue) in VEX, ACE and MEX data with each event numbered. In some cases it should be noted that the time of arrival at VEX lies between actual observations. Although the arrival is clear from the difference in the energy of the solar wind ion beam between successive observations, this does lead to an error of ± 11 hours. Here the time of arrival of events in the MEX observations are the same as reported in Edberg et al. (2010). In addition the estimated arrival times as calculated from ACE and STEREO A/HI are plotted, with an approximate width for error and to account for the size of the events, in green and red respectively. Edberg et al. (2010) showed that the effects of CIRs last for approximately 36 hours during this period which enables us to add an approximate width. This is combined with the error on velocity observed by STEREO/HI as defined in Rouillard et al. (2010a).

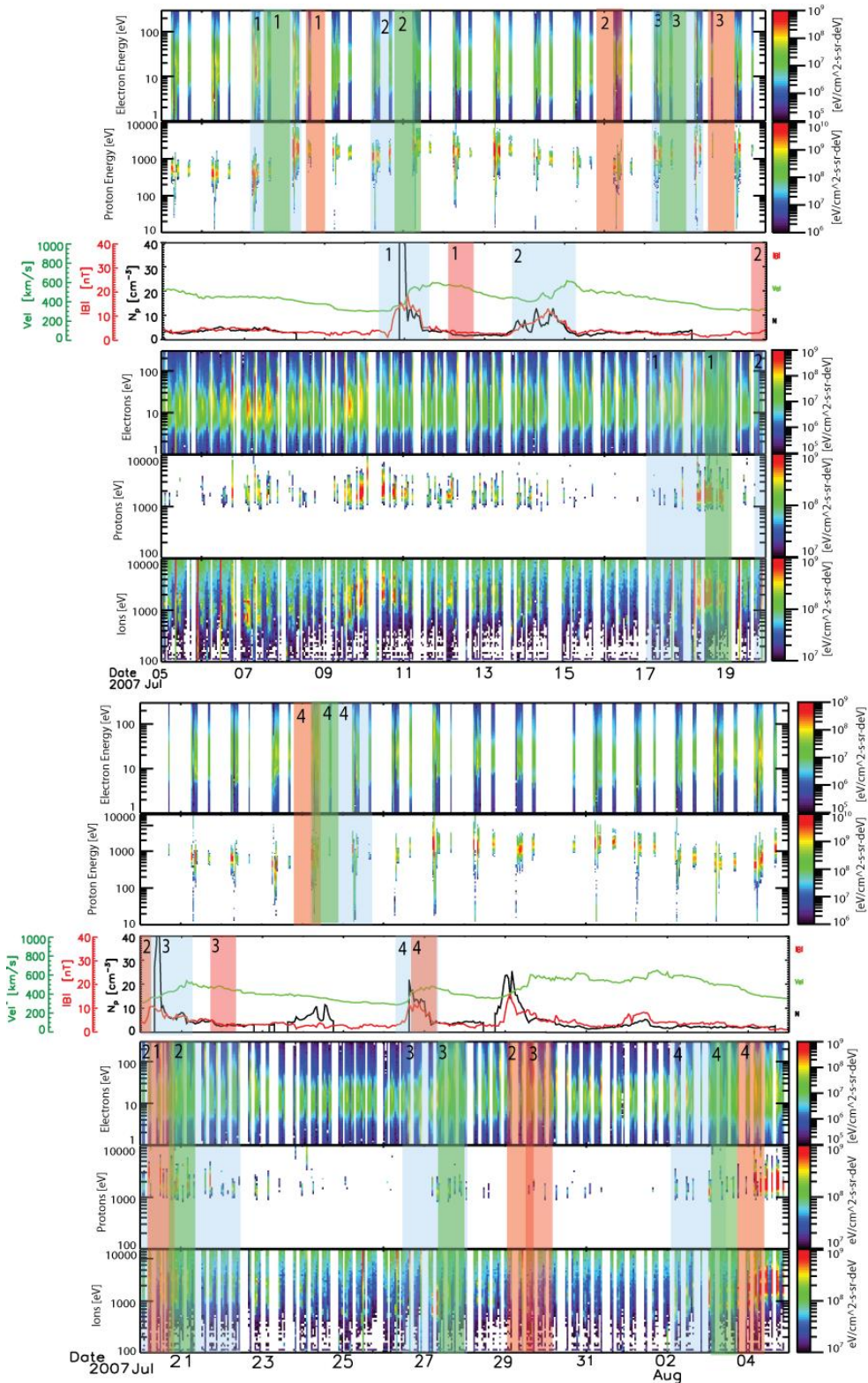


Figure 5.5: Time series plots as in Figure 5.2 for the period from 5 July 2007 to 5 August 2007. During this period 4 CIRs are visible in VEX, ACE and MEX. The blue boxes indicate the observations of the numbered CIR. Green boxes indicate predictions using ACE, while red boxes indicate predictions from STEREO/HI observations.

In general, using the ACE data provides the basis for a very good estimate of the time of arrival at other planetary bodies. This is best shown by presenting the difference between arrival times expected from ACE and the observed arrival time from MEX, STEREO A and STEREO B for all 24 events. The difference is plotted in Figure 5.6 which shows a histogram with 6 hour bins. Figure 5.6 shows the difference between the expected and observed arrival times at VEX (panel a), MEX (panel b), STEREO A (panel c) and STEREO B (panel d). In panel (a) we note that the majority of events occur within 1 day of the expected arrival time. However, due to data gaps, we were only able to examine 17 CIRs, although we note there could be other reasons for a lack of observations as described below. From panel (b) we can see that 17 of the CIRs arrive within 1 day of when they are expected at MEX, with all CIRs arriving within 1.5 days of when they are expected. Looking at panels (c) and (d), where we have a more direct comparison of observations with ACE, we notice that the majority of CIRs arrive within 18 hours of when we expect. In the case of STEREO A, the distribution of time differences is mostly around zero with CIRs arriving both earlier and later than expected, although the typical displacement is approximately 12 hours. However at STEREO B all CIRs arrive later than expected with the majority arriving 6-18 hours later than expected.

We plot similar histograms for the differences between the expected arrival times from STEREO A/HI and the observed arrival times at each spacecraft in Figure 5.7. As in figure 5.6 we plot the difference between the observed and expected arrival times with a negative value indicating that the CIR was observed before it was expected as calculated from the STEREO A/HI observations. From figure 5.7 we can see that in the majority of cases we observe the arrival of a CIR before we expect to from the HI observations. The main point to note here is that the differences between the observed

and expected arrival times are in general much larger than those seen in figure 5.6. There is also one clear outlier that gets progressively further away from the observed CIR as it progresses radially through the heliosphere. This is a sign of either a very large underestimate of the radial speed of the CIR or an incorrectly identified CIR. This outlier does also reflect the increasing differences between observed and expected arrival times seen with increasing radial distances in the majority of events indicating that, in general, STEREO/HI underestimates the radial speed of the CIR.

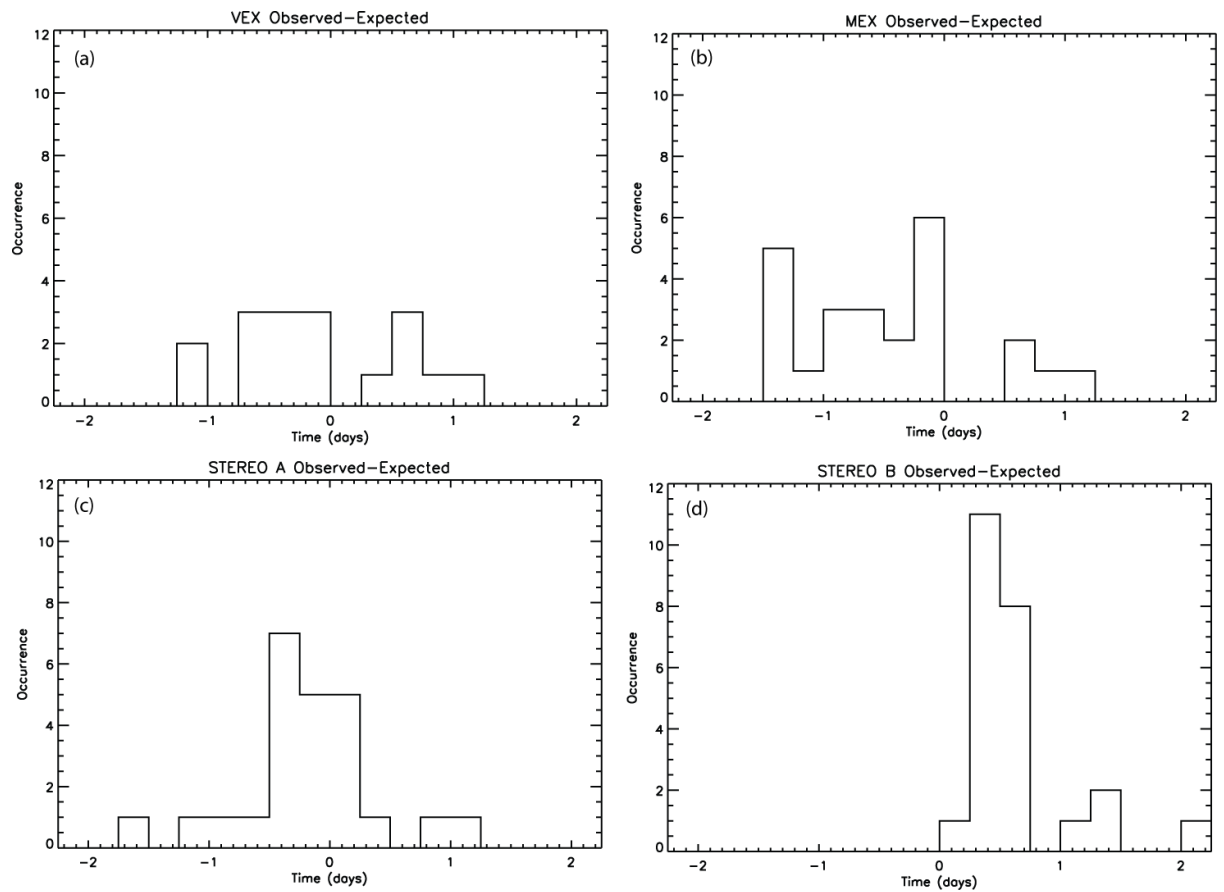


Figure 5.6: Occurrence distribution of the difference between arrival times as calculated using equation 5.1 from ACE observations and the observed arrival times from (a) VEX, (b) MEX, (c) STEREO A, and (d) STEREO B. Each bin is 6 hours wide.

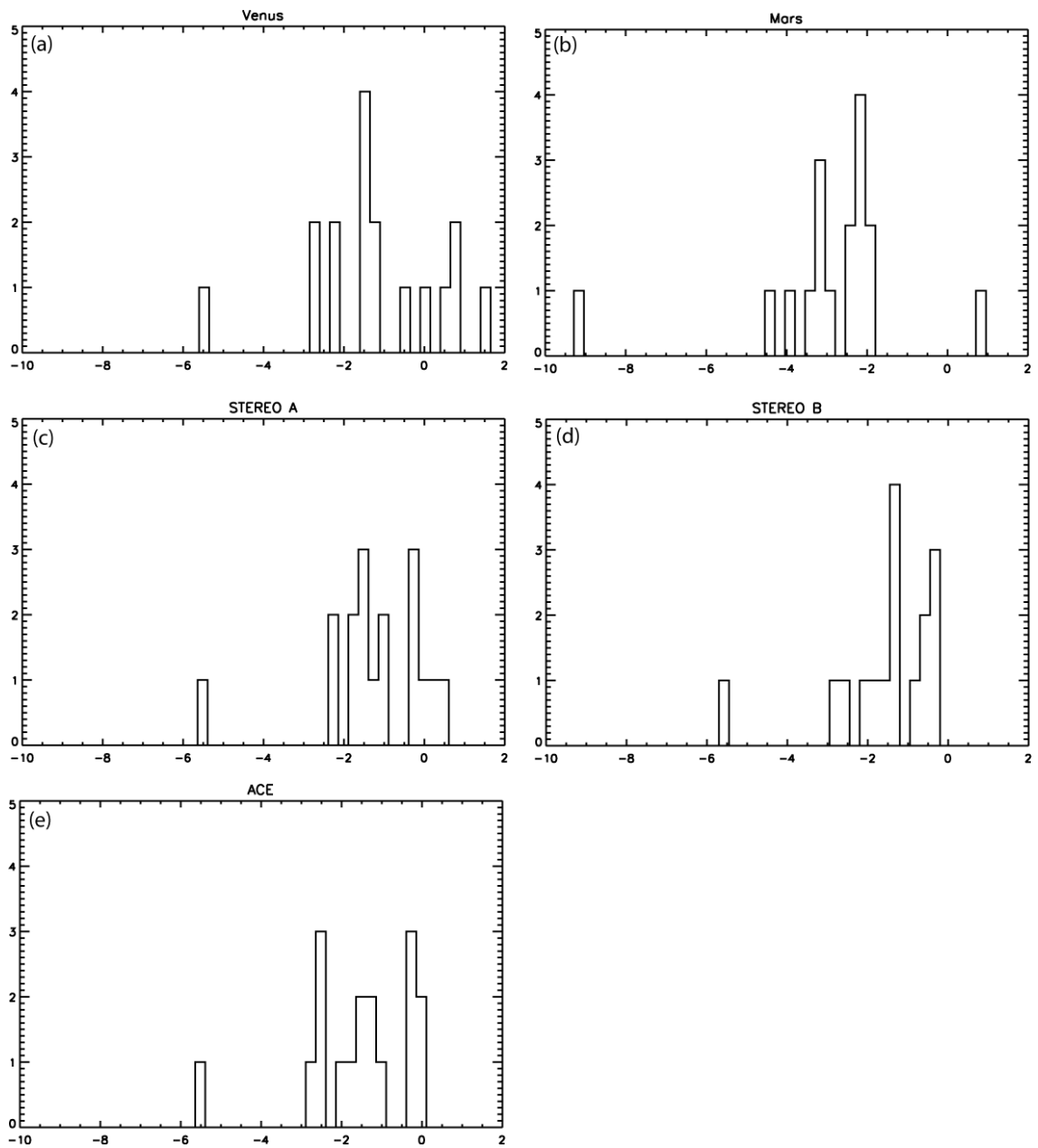


Figure 5.7: Occurrence distribution of the difference between arrival times as calculated using equation 5.1 from STEREO A/HI observations and the observed arrival times from (a) VEX, (b) MEX, (c) STEREO A, (d) STEREO B and (e) ACE. Each bin is 6 hours wide.

5.5. Discussion

As shown by Figure 5.5 there is a discrepancy between arrival times of CIRs estimated from STEREO/HI J-maps and the observed arrival time at ACE. With regard to the estimates of arrival times at Venus and Mars both data sets have inherent problems. ACE is only one point in space and so cannot measure the radial CIR speed at all heliographic longitudes. Using only ACE gives us no information about the continuity of the CIR in longitude, although the addition of STEREO A and STEREO B in-situ observations help to fill this gap. The lack of good correlation described earlier strengthens this argument. Observations of the source coronal hole on the sun would also aid in establishing the continued presence of the CIR. Despite these potential drawbacks there is good agreement between the estimated arrival times and actual arrival times of CIRs at Mars using the limited data provided by ACE and two assumptions of CIR behaviour.

Estimates from STEREO/HI J-maps have their own inherent problems. While there have been several documented cases of the method used here providing velocities and directions in agreement with in-situ data and estimates from other methods (Davis, Kennedy and Davies, 2010; Rouillard et al., 2009a,b), other work has also shown that it can be difficult to identify complete events in the J-maps (Savani et al., 2009) and this can lead to an inaccurate estimation of the propagation angle or velocity or both. Indeed the correct identification of complete events for sufficient periods is probably the largest source of error for this method. In addition, the effects of the assumptions should be considered. This method assumes two things about the propagation of transient events through the STEREO/HI field of view, firstly that the transients are point-like objects and secondly that they move at a constant velocity and in a constant direction. The first assumption is an effect unique to the J-map method. CIRs are inherently three-

dimensional objects, as is clear from their formation mechanism, and although they are visible in HI observations the tracking technique used here is not applicable as it assumes point-like objects are being tracked. The extended nature of CIRs mean this technique is unsuitable for application to CIRs. However the signatures of plasma parcels which are entrained within a CIR can be treated as point-like objects and tracked using the method presented here, as highlighted in Figure 5.1 and described in Rouillard et al. (2009a). By assuming a constant velocity and direction any acceleration which could alter the shape of the transient track is ignored. This can lead to an error in determining the velocity and direction which will lead to errors in determining the arrival time of the CIR front at other locations. If the direction of propagation is known from another method, then a velocity profile can be found which might allow for an estimation with less error.

There is one further source of error that should be considered when using the method of estimating solar transient event properties from STEREO/HI J-maps, which is the inherent user error in selecting the points for fitting to equation 5.2. This source of error has been more thoroughly investigated in the previous chapter using simulated point selection for an ideal trace and a Monte-Carlo method to determine a suitable visibility of events in elongation to minimize errors.

As mentioned in the previous section there are some events which were not observable in the VEX/ASPHERA-4 data and, as previously described, the observations are intermittent due to the orbital configuration of VEX with respect to Venus. As VEX only spends a short time each orbit in the exosphere of Venus it is possible that ASPHERA-4 was not in a good location for long enough to collect many clear signatures. Another reason for a lack of clear signatures could be due to the difference in densities in the atmospheres between Venus and Mars. It is possible that the increased density at

Venus allows it to better retain its atmosphere during CIR transits. In addition, as hypothesized by Edberg et al. (2010), CIRs could be less well developed at the orbit of Venus and this may have a smaller impact on the Venusian atmosphere.

One potential further source of error that applies to all comparisons of data is the potential for latitudinal differences in the structure of interaction regions. Although the differences are small, approaching approximately 3° at the end of July 2008 between ACE and either STEREO spacecraft, they could make a difference and could help to explain why the density structures observed at the 3 spacecraft are frequently so different. Helios observations (Schwenn and Marsch, 1990) showed that a latitudinal separation of only 1° between two spacecraft can lead to significant observational differences as they observe different latitudinal slices of the same coronal hole. Indeed Simunac et al. (2009) undertook a correlation of expected bulk velocity and density at STEREO B from STEREO A during 2 events in July 2008 and while there was an approximately 1:1 correlation (0.96) in bulk velocity, there was a poor correlation in density.

5.6. Conclusion

We have presented a technique for estimating the time of arrival of CIRs at planetary bodies and other spacecraft from observations of their passage through the inner heliosphere in the STEREO/HI instruments, and from ACE observations. As we have shown, using the mean measured velocity from ACE gives a good prediction. STEREO/HI will provide additional information about the temporal behaviour and may in future give a predictive capability. At the time of writing the STEREO spacecraft are separated by approximately 70° from Earth and so are moving out of position to get

optimum views of Earth-directed events. Hence predictions of arrival times at Earth will need to be done by future missions. There are times when predictions of arrival times at Venus or Mars would only be possible in advance with STEREO/HI, such as when either planet is lagging the Earth in their orbit, as with Mars in Figure 5.3. In this case waiting for the CIR to arrive at ACE would be too late as it would have already arrived and impacted at Mars or Venus. STEREO/HI observations can still give us advance warning of an impending CIR at Earth if we use a reasonable estimate of the velocity, for example a mean velocity from several previous CIRs and make the assumption that the fitted angle is correct.

6. Examining the radial motion of transient solar wind events using STEREO/HI

6.1. Introduction

In this chapter we will examine coronal mass ejections (CMEs) during their transit from the Sun to the Earth. The heliospheric imagers on the STEREO spacecraft can be used to examine several bulk properties of CMEs and these measurements can be compared with in-situ observations to gain an understanding of the CMEs radial motion as it travels out from the Sun.

CME evolution close to the solar surface has been well studied using coronagraphs on a variety of missions such as the Solar and Heliospheric Observatory (SOHO). From these previous observations we have learned that CMEs have a limited size both longitudinally and latitudinally (Hundhausen, 1993). We also know that CMEs typically undergo the majority of their acceleration close to the Sun (Howard et al., 1997) and from then on tend to have an approximately constant speed (Sheeley et al., 1999).

The value of the acceleration leading up to this constant speed has been previously measured (e.g. Howard et al., 1997; Sheeley et al., 1999) and found to be variable depending on what other solar phenomena are associated with the CME. CMEs are typically associated with either the lift off of prominence material or a solar flare occurring nearby. Those CMEs associated with the lift off of prominence material tend to accelerate slowly and reach a speed similar to that of the background solar wind, around $300\text{-}400 \text{ km s}^{-1}$ (Andrews and Howard, 2001). CMEs associated with a solar

flare tend to be much more impulsive and accelerate quickly, often to a speed higher than that of the background solar wind (Andrews and Howard, 2001).

A further observable property of CMEs is their longitudinal expansion rate which is also variable depending on the associated solar phenomenon (e.g. Cremades and Bothmer, 2004; Michalek, Gopalswamy and Yashiro, 2009; Savani et al., 2009) although it typically follows a power law with increasing radial distance.

In addition to remote imaging of CMEs we are able to measure the in-situ properties of CMEs as they pass over spacecraft such as the Advanced Composition Explorer (ACE). CMEs have several identifying signatures visible in in-situ data (Neugebauer and Goldstein, 1997) but not all CMEs have all of these features. For the purposes of this chapter it is sufficient to know that we are looking for an enhancement in the solar wind density and this will usually be accompanied by a magnetic cloud (Marubashi, 1997) which is characterised by a rotation in one or more magnetic field components.

By combining observations from the STEREO spacecraft with in-situ observations from the ACE spacecraft we aim to examine CME speeds from near the solar surface to the near-Earth environment. Figure 6.1 shows the positions of the STEREO spacecraft and the field of view of the HI instruments on the 1st February 2010 which is the start of our observing period.

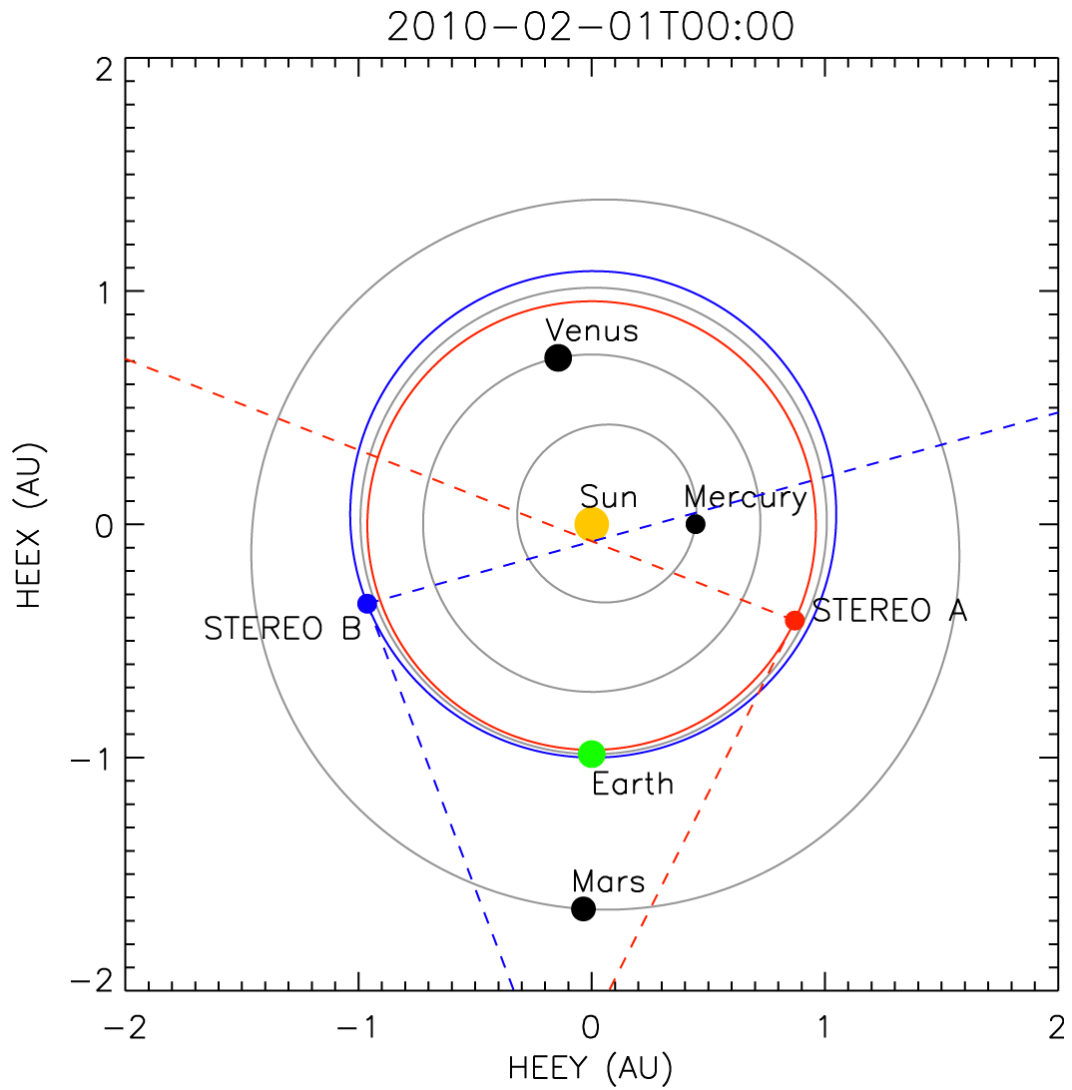


Figure 6.1: The positions and orbits of the inner planets and the STEREO spacecraft for the 1st February 2010. The edges of the HI fields of view are shown in red for STEREO A and blue for STEREO B.

6.2. Method

Using images from the STEREO/HI we constructed elongation-time plots known as J-maps for the period from February 2010 to April 2010 as previously described (Sheeley et al., 1999; Rouillard et al., 2009a). An example is shown for STEREO A and B in Figure 6.2. From these J-maps we extracted the velocities and directions of the leading tracks for each of our events using equation 4.5 and points taken from traces of transients visible in the J-maps. The events chosen in this case were selected based on the event being visible in both STEREO spacecraft and being visible to elongations of greater than 40° in at least one of the J-maps.

Those events suspected to be Earth-directed, within 10° of the Sun-Earth line, were then confirmed using in-situ data from the ACE spacecraft. Using the expected time of arrival we looked for enhancements in the observed density where the velocity observed was similar to that measured using the STEREO J-maps and used the leading edge of the observed density enhancement as our observed arrival time. For each of our events we studied the leading track to obtain our time of arrival and used 5 measurements of that track to obtain an average velocity and direction for the track although some of the events studied had several tracks corresponding to different features within the transient,. Using multiple measurements of each track helps to reduce the user identification error demonstrated in chapter 4. Using these average values for velocity and direction we calculated the expected arrival time at Earth for the transient. Then using the 5 tracks which made up our average we calculated arrival times for those velocities and directions. Using these arrival times we were able to add an error on the expected arrival time by looking at the average deviation of the arrival times. Applying this to the second track in Figure 6.2 in STEREO A we obtained a

velocity of 302 km s^{-1} resulting in an expected arrival time of 8 Feb 2010 23:56. The actual arrival time for the density enhancement associated with this track was 8 Feb 2010 04:30 and the observed velocity was slightly higher at 350 km s^{-1} .

Next using the angle of separation of the STEREO spacecraft with the ACE spacecraft, the observed in-situ velocity at the observed arrival time of a transient and equation 6.1 we created model traces for each of the observed traces in the J-map. These model traces align as closely as possible to observed in-situ density enhancements. Then keeping the velocity constant we adjusted the angle used to produce the model trace until the model trace more closely aligned with the observed trace. We then plotted the directions obtained from the J-map model traces on a two dimensional projection of the solar system to more clearly see how close the transients were predicted to approach Earth.

When we compare expected and observed arrival times we find good matches and poorer matches. We will examine the events in more detail to try to explain why for some events the expected arrival time and observed arrival time do not match closely and why for others it does. Using Figure 6.2 as an example, we show a combined plot of the J-maps of STEREO A and STEREO B with overlaid back traces calculated using equation 6.1 using the observed solar wind parameters and timing. Often there are multiple traces shown on the J-map, some of which may not actually be Earth-directed but are included as they occur close to the event we are interested in. At the top of the figure the solar wind density (black) and the velocity (red) are shown and to the right is displayed the direction corresponding to those traces. In all cases the traces are colour coded to match with the directions indicated on the direction plot to the right of the figure. The vertical black lines indicate the time at the end of the back trace which is approximately Earth orbit.

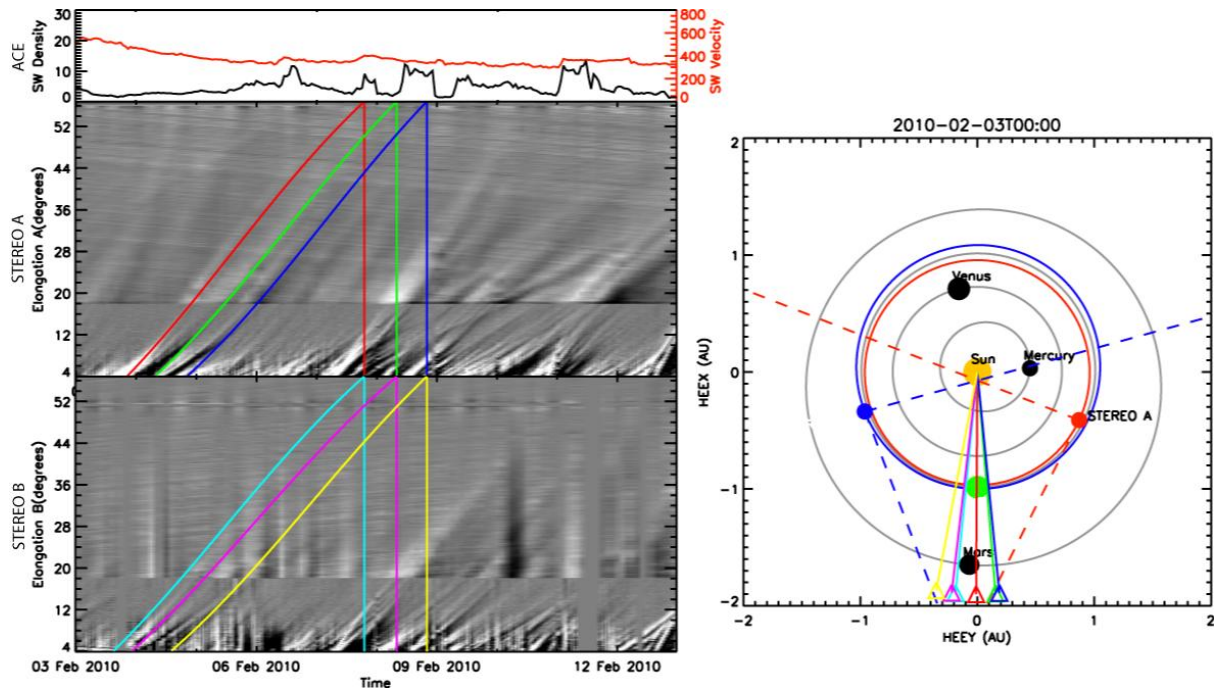


Figure 6.2: Combined J-map, solar wind density, velocity and direction plots for the 3rd February 2010 event as described in the text.

6.3. Observations

Our observations are from the period from the 1st February to the 30th April 2010, a period during which the STEREO spacecraft were able to observe transients with separations of 60° to 70° from the Sun-spacecraft line. This separation corresponds to close to the Sun-Earth line and also has good visibility along the Thomson Sphere. During this period we observed several transient structures which were Earth-directed, which we will now examine. Table 6.1 below shows a list of the transients with the date of first observation. The table also shows the observed time of arrival at ACE, lagged to Earth, for the leading edge of the CME.

Date (2010)	Expected arrival as determined by STEREO A	Error on expected arrival time (mins)	Expected arrival as determined by STEREO B	Error on expected arrival time (mins)	Observed arrival at ACE
3 rd February	08/02/2010 23:56	69	08/02/2010 04:34	238	07/02/10 18:10
7 th February	11/02/2010 03:37	82	10/02/2010 16:16	151	11/02/10 02:00
12 th February	14/02/2010 23:22	121	15/02/2010 07:29	60	15/02/10 19:00
19 th March	24/03/2010 09:20	48	25/03/2010 05:07	28	25/03/2010 11:50
3 rd April	05/04/2010 11:58	60	05/04/2010 05:47	232	05/04/2010 08:45
8 th April	11/04/2010 16:00	72	11/04/2010 19:06	153	11/04/2010 15:00
19 th April	23/04/2010 03:58	30	23/04/2010 04:37	29	22/04/2010 21:00

Table 6.1: Transient events used in this study as observed by STEREO A and B, with expected arrival and observed arrival at ACE.

As we can see from Table 6.1 there is a range of uncertainty between 28 minutes and 238 minutes (or nearly 4 hours). In some cases, there is a significant difference

between the expected arrival time and the observed arrival time, which is better illustrated in Figure 6.3. This shows the difference between the observed arrival time and expected arrival time for each of the events from each spacecraft. The vertical error bars shown are those errors from the expected arrival time calculated using the 5 measurements determined earlier. Here a positive value indicates that the expected arrival time is earlier than the observed arrival time and a negative value indicates that the expected arrival time is later than the observed arrival time.

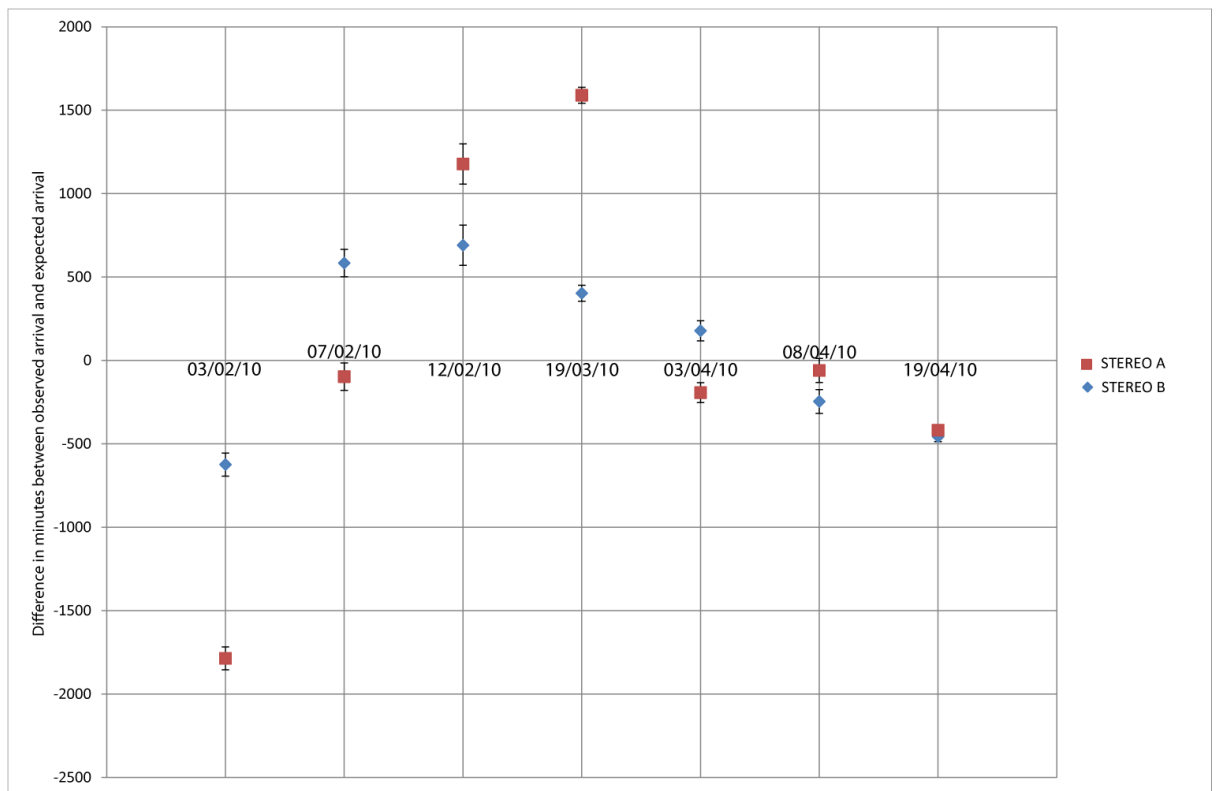


Figure 6.3: The time differences in minutes between the observed and expected arrival times with error bars indicating the error on the expected arrival times.

In Figures 6.4-6.9 we will now examine all the events in detail using the same format as Figure 6.2. The latter figure shows the traces from the 3rd February event and from Table 6.1 we see that the expected arrival time was later than the observed arrival time for this event. At low elongations the J-maps show a clear deviation from the back traced line. Attempts to align the back trace both with this section of the J-map, which is usually the brightest as the coronal material is denser nearer the Sun, and with the rest of the J-map were unsuccessful. There are two possible explanations for this. First, there could still be some acceleration occurring in this region (e.g. Andrews and Howard, 2001; Sheeley et al., 1999; Wood et al., 2009). Second, the STEREO HI cameras might be observing other material, either another part of the CME to that observed later, or other coronal material, which is travelling at either a different speed or in a different direction, or both. However if we ignore these sections at low elongations and focus on the trace at larger elongations we notice a good agreement between the trace and the observations and we can see that these traces match with enhancements in the observed solar wind density. Finally looking at the directions of the traces we note they remain close to the Sun-Earth line, so we consider it likely that the observations from the STEREO spacecraft are the same density enhancements observed by the ACE spacecraft.

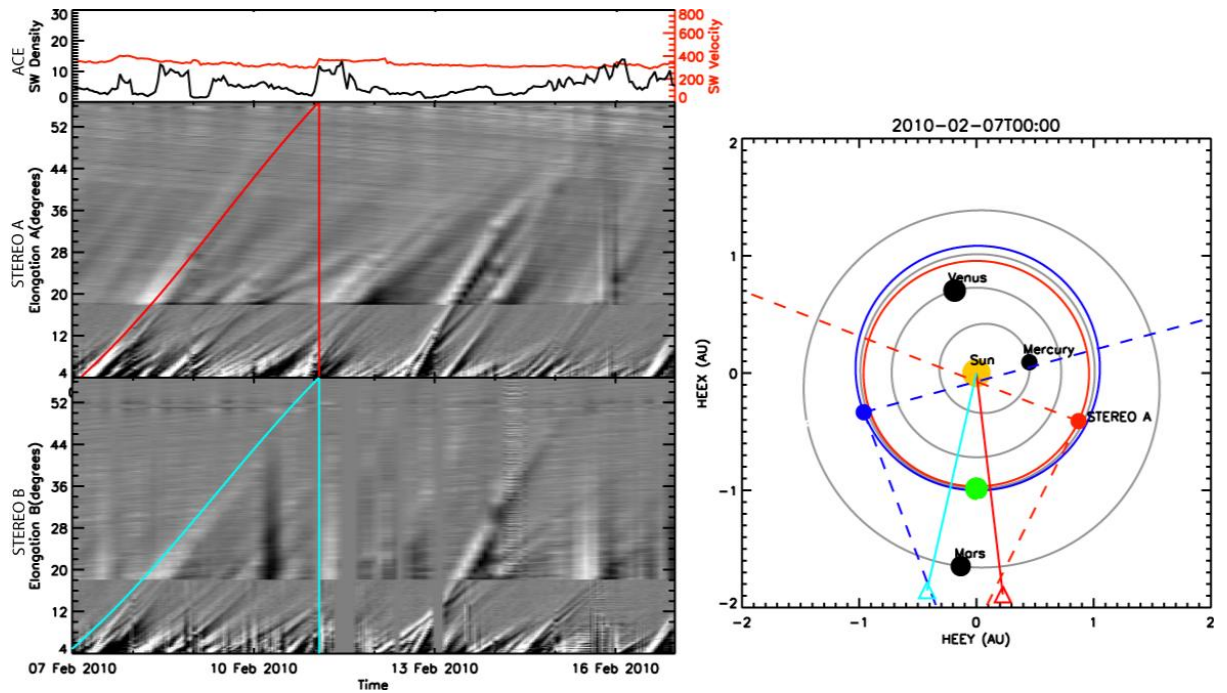


Figure 6.4: Combined J-map, solar wind density, velocity and direction plots for the 7th February 2010 event as described in the text.

Figure 6.4 shows the event of the 7th February (also visible in Figure 6.2) and from Table 6.1 and Figure 6.3 we note that the expected arrival time from STEREO A was very close to the observed arrival time. In this case this most probably represents the central peak of the density enhancement in ACE being visible in the STEREO HI rather than the leading edge of the CME. However in STEREO B we note that the expected arrival time was nearly 10 hours earlier than the observed arrival time. If we now look at the trace on the J-map for both STEREO A and B we first note that the back trace does appear to be slightly ahead of that in the J-map but the back trace aligns with the observed enhancement in solar wind density. Looking at the low elongations it is interesting to note that there are several thinner traces with different shapes which all appear to make up the trace seen at greater elongations. It is possible that these conflicting shapes have introduced an error into the calculations and caused the discrepancy between the expected and observed arrival times. Returning to the

STEREO A J-map we note a similar dual profile at low elongations. However one of these profiles matches the back trace very well and so gives a clear identification of the transient. Looking now at the directional plot, we can see that the trace from STEREO A passes close enough to the Earth to be the likely cause of the observed enhancement in solar wind density, while the trace from STEREO B is further away. This is an indication of the lower limit of the angular extent of the transient although earlier studies (e.g. Savani et al., 2009) suggest that the transient is likely to be wider than this.

Figure 6.5 shows multiple traces from the period around the 12th February. From the directional plot it is clear that some of these tracks are more likely to be related to solar wind density enhancements observed at ACE than others. Indeed there are three tracks which can be identified as clearly causing density enhancements at Earth. Two of these tracks are visible in STEREO A and are first visible on the 10th February, while the third begins in STEREO B on the 11th February. The STEREO A tracks are a good match to the underlying J-map as is the track in STEREO B. The tracks also appear to end at times of enhanced density in the solar wind. However it is also interesting to note that the enhanced solar wind density is quite long lasting and does not have a clear onset. It is worth noting the other back traces in these plots which match well to the J-maps but which are much less likely to be responsible for the enhanced solar wind density. They are however much brighter and so illustrate the potential for confusion that can arise when studying J-maps for transients, especially those which are Earth-directed.

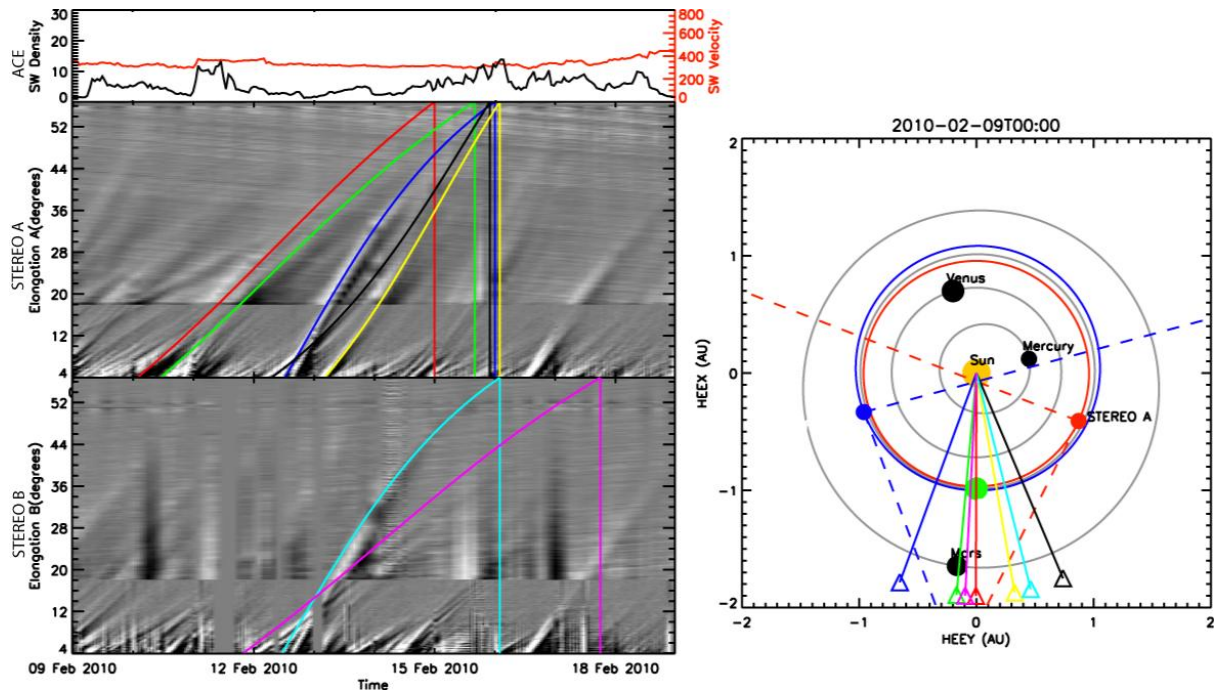


Figure 6.5: Combined J-map, solar wind density, velocity and direction plots for the 12th February 2010 event as described in the text.

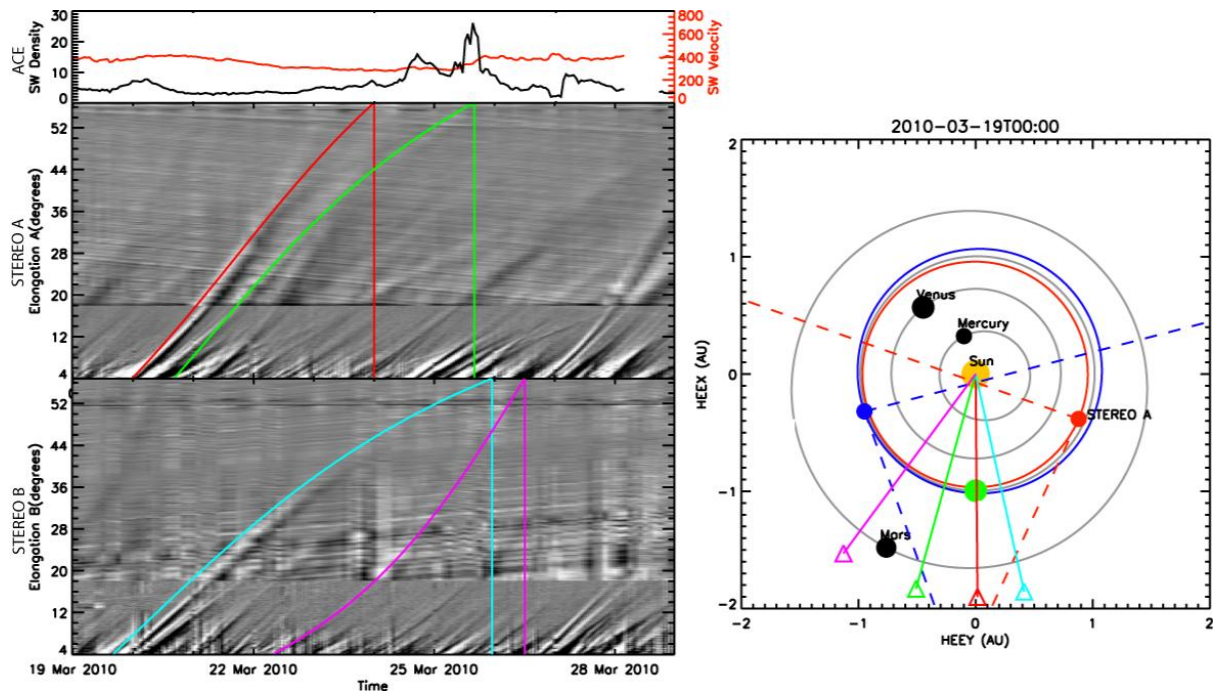


Figure 6.6: Combined J-map, solar wind density, velocity and direction plots for the 19th March 2010 event as described in the text.

Figure 6.6 shows the event from March 19th 2010 where there is a clear track in STEREO A which is Earth-directed and which for the most part appears to match closely to the underlying J-map. However returning to Table 6.1 and Figure 6.3 we see that the expected arrival time calculated from STEREO A is over a day earlier than any observed density enhancement at ACE, suggesting that this trace is not in fact Earth-directed. The second trace visible in STEREO A does appear to match more closely with a density enhancement observed in ACE but the direction plot suggests that the STEREO observations are not directly of Earth-directed material and once again observations of elongations close to the Sun do not match the overlaid trace at all well. Once again this suggests either early acceleration of the transient or the observation of coronal material that is not Earth-directed. Looking at the J-map from STEREO B we struggle to find a track which we can then align with an enhancement in the solar wind density although the direction plot indicates that perhaps one of the tracks will pass close enough to Earth to be observed by ACE. However, for these tracks we do have a much better agreement at small elongations between the back trace and the J-map. This is especially true of the first track which is conjugate with the STEREO A tracks indicating that there is no acceleration for this part of the transient. If we extend that to the rest of the transient including that part observed by STEREO A we can conclude that the difference between the back trace and the J-map in STEREO A is most likely a result of different azimuthal sections of the transient being observed at different elongations.

Figure 6.7 is an example of a very fast CME and is also one in which the expected arrival times are close, approximately 3 hours difference, to the observed arrival times. It is clear that for this event we have conjugate images of the same CME in both STEREO A and B and that in both cases we can find a back trace that matches

well with the J-map. From the direction plot we can see that STEREO observes a relatively narrow portion of the transient, this could be a result of the observational geometry or a property of this particular CME. It should be noted that for this CME the STEREO B/HI-2 observations are of poor quality and it is very difficult to see evidence of the transient in that camera. Reasons for the poor quality of HI-2 observations for April 2010 are at present unclear.

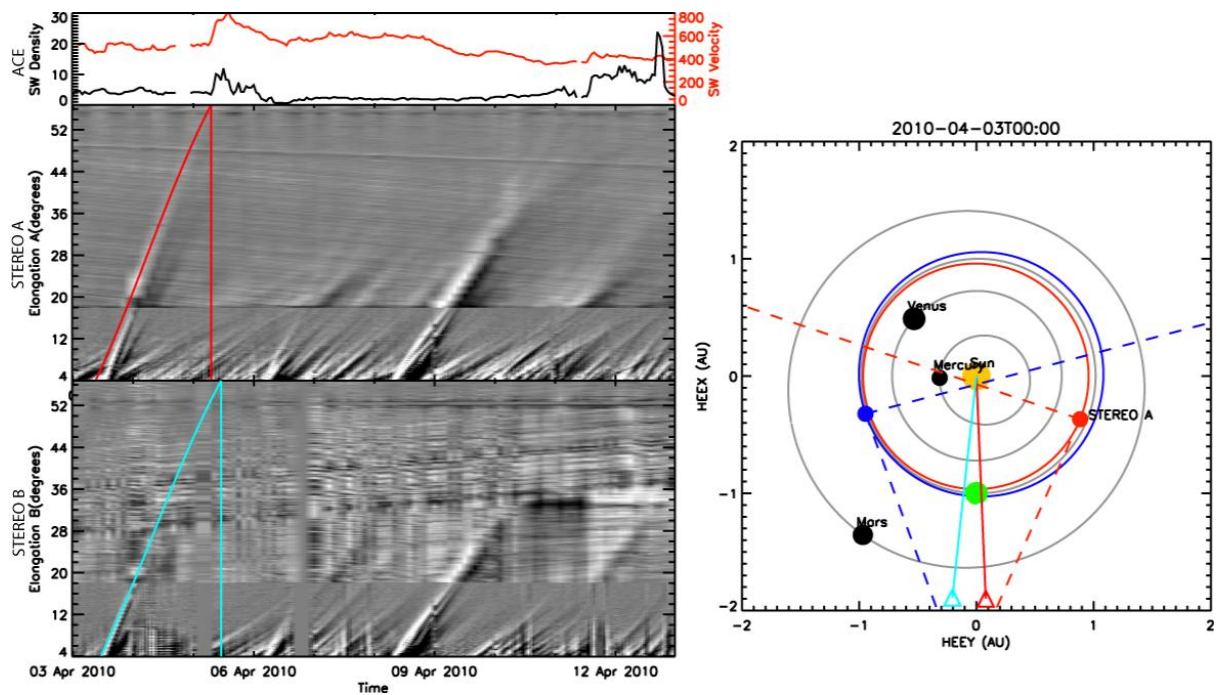


Figure 6.7: Combined J-map, solar wind density, velocity and direction plots for the 3rd April 2010 event as described in the text.

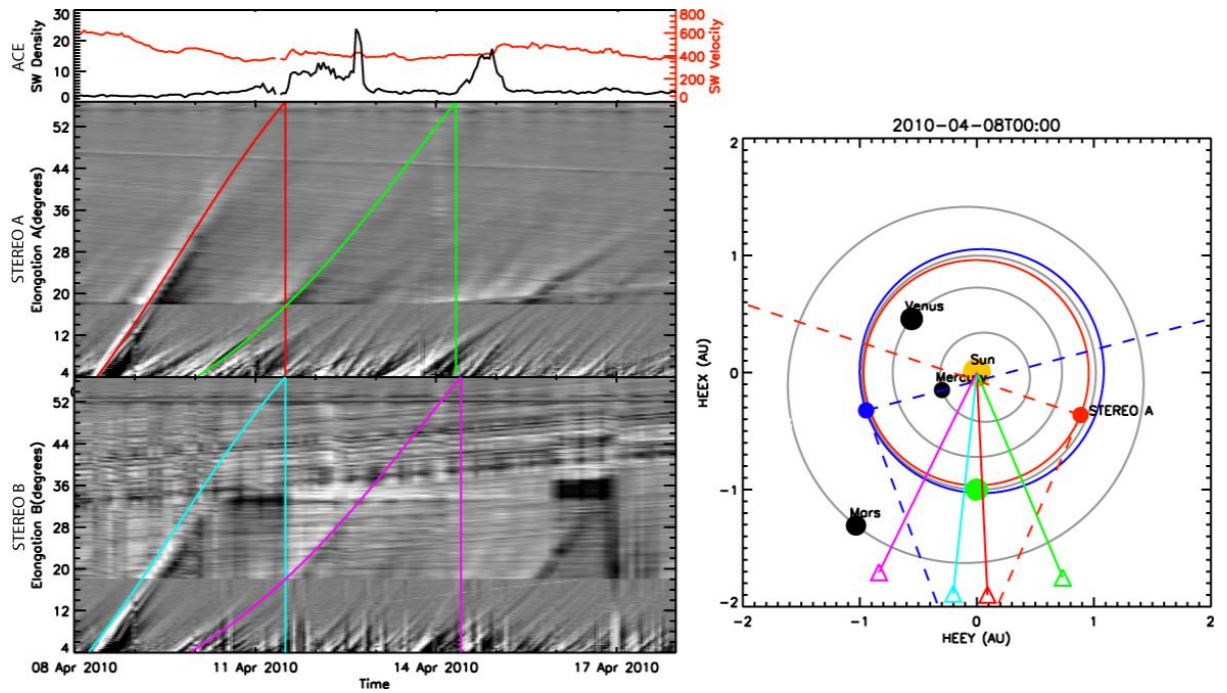


Figure 6.8: Combined J-map, solar wind density, velocity and direction plots for the 8th April 2010 event as described in the text.

Figure 6.8 shows two potential transients which both appear to produce an enhanced density in the solar wind at Earth. The first track in STEREO A and B appear to be directed very close to the Earth and so an enhanced density should perhaps be expected. However the second tracks in STEREO A and B, which appear to be conjugate, have directions much further from the Sun-Earth line and we might not expect them to cause a density enhancement observable by ACE. It is notable that we can make the case for observing coronal material out to large elongations in STEREO A for this second track which we can align with a density enhancement but that the same region in STEREO B is less clear. Consequently the direction and arrival of the transient for STEREO B could be incorrect in this case although it is not impossible that the angular width of the transient could be as large as suggested by the directional plot in Figure 6.8. Also of note is that Table 6.1 only refers to the first pair of tracks in

Figure 6.8 and in this case we can see that the back trace agrees well at all elongations with the J-map and the expected arrival times are close to observed arrival times.

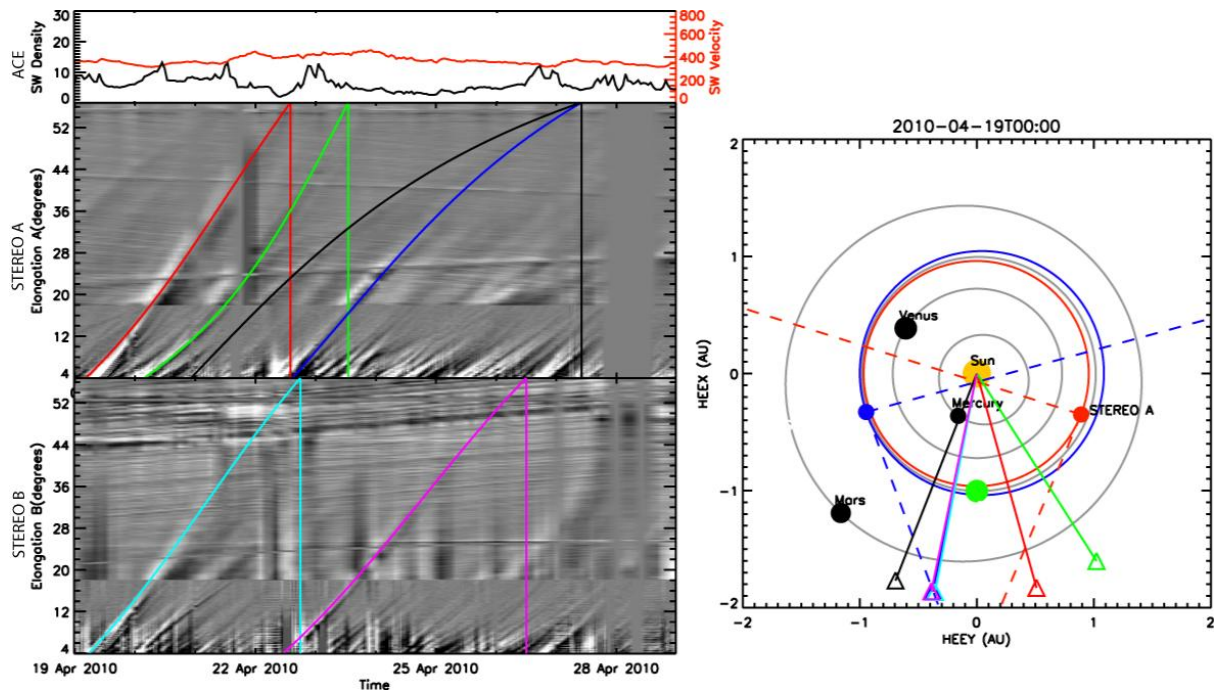


Figure 6.9: Combined J-map, solar wind density, velocity and direction plots for the 19th April 2010 event as described in the text.

Figure 6.9 is the final event we have studied in this period and once again encompasses multiple events, only the first of which is reported in Table 6.1. It is interesting to note that here we have very good agreement between the back traces and the J-map and the enhancements in the solar wind density. However from Table 6.1 we see that the expected arrival times for both STEREO A and B are a few hours after the observed arrival time. The reason for this is not at all clear from the J-maps and back traces. However looking at the directional plot it would appear that we are viewing a section of the transient which is slightly further away from the Sun-Earth line which has reached Earth orbit after the Earth directed section has already arrived. Once again it

would appear that we have a good agreement between the back traces and the J-maps which results in a good initial fit.

6.4. Discussion

We have studied the signatures of Earth-directed CMEs in STEREO HI data and compared the predicted arrival time at 1 AU with in-situ observations from ACE. In several events we notice a good agreement between the back trace from the ACE observations and the observations made in the STEREO J-map. It is interesting to note that when we see a good agreement at low elongations we also notice that the expected arrival time as determined by the STEREO spacecraft as presented in Table 6.1 matches well with the observed arrival time in ACE. Similarly those events where the STEREO J-map observations do not match well, the ACE observations have a much larger difference between the expected and observed arrival times.

There are two possible reasons for this discrepancy both related to the underlying assumptions in equation 6.1. As a reminder these two assumptions are that we are observing a point source, and that it is travelling at a constant speed within the HI field of view. Let us consider the situation where we are not observing a point source but instead an extended source or alternatively different point sources at different elongations which make up an overall transient as shown in Figure 6.10. Figure 6.10 shows a hypothetical transient with a typical arc structure propagating away from the Sun. Diagram (a) shows the arc at time t_0 where the STEREO spacecraft is observing the black point. If the spacecraft were to continue observing that point then we would measure the transient to be travelling in that direction at the speed of that point which we assume is the speed of the whole transient. Diagram (b) shows a later time, t_1 , here

we are observing a section of the transient travelling at much different angle. Note that the change in observed points is greatly exaggerated and the actual change in direction occurring as a result of observing different material is likely to be less extreme.

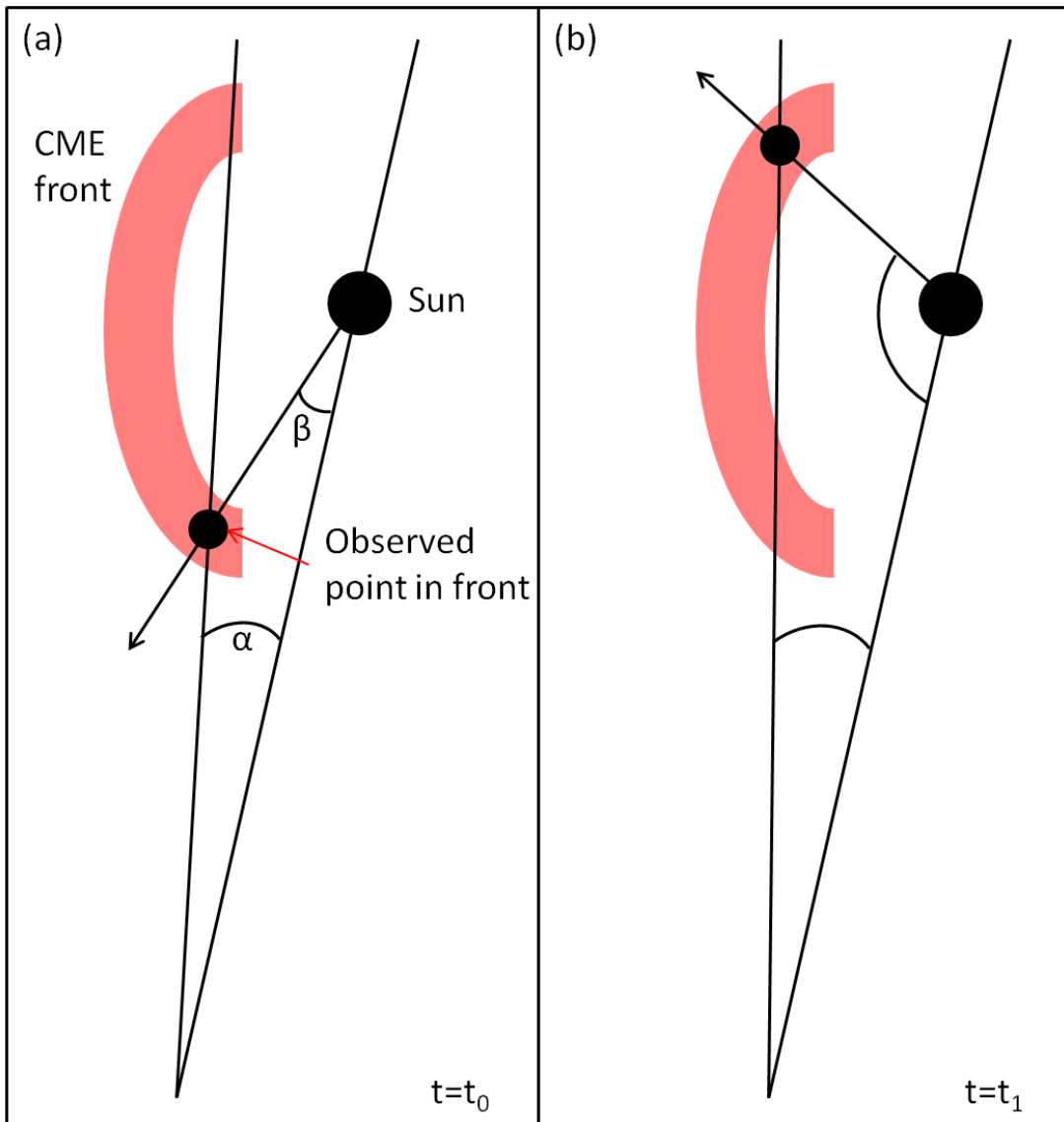


Figure 6.10: A possible way in which STEREO/HI could observe 2 points within a transient in the solar wind. Diagram (a) shows the view from above the ecliptic plane of the position of a transient at a time, t_0 , and the elongation observed of a particular point (shown in black) with an arrow indicating the direction that it appears to be travelling in. Diagram (b) shows the same transient at a later time t_1 where we are now observing at a slightly larger elongation (as in a J-map).

This change in direction, however slight, can affect the observations extracted from the J-map and so adjust the values of V_r and β we obtain.

Secondly it is possible that at low elongations the transient could still be accelerating. This will also affect our measurement of the speed and direction while still appearing as a constant track in the J-map. Previous work has shown that some transients can indeed still be accelerating at larger radial distances although those studies have previously been limited to coronagraph observations (Andrews and Howard, 2001; Sheeley et al., 1999; Wood et al., 2009). Similarly for fast CMEs such as in figure 6.7 there exists the possibility of deceleration although this has previously been found to occur within a few solar radii of the Sun (Sheeley et al., 1999). At larger radial distances studies have been unable to detect the deceleration of CMEs although this appears to be a general result for all CMEs (Liu, Richardson and Belcher, 2005).

The two effects already mentioned both tend to occur at low elongations but there is one further complication which is visible in many of the J-maps of Figures 6.3 to 6.9, that of multiple tracks occurring in quick succession and crossing over each other. When these tracks have similar profiles it can be tricky to distinguish between them, although this is usually possible in the HI-1 camera. However the HI-2 camera takes longer to take an image which means that if there are two tracks entering the field of view of the HI-2 imager at similar times they can appear to merge into one track. This can produce a discontinuity in the individual tracks and introduces a potential source of error on the speed and direction measurement.

Despite the potential sources of error we have discussed, we have also presented clear evidence that the technique using J-maps and equation 6.1 is valid for some transients. There are cases where the technique gives an estimated time of arrival much

later than the observed arrival time, though we conclude that this occurs mainly due to an inability to discriminate between multiple overlapping tracks.

6.5. Conclusions

For the events presented here, where the STEREO spacecraft were approximately $65^\circ - 70^\circ$ away from the Sun-Earth line, we find a generally good agreement between the expected arrival time and observed arrival time for 7 CMEs. We find the best agreement when the observations of the CME at low elongations are easily distinguishable and can be accurately fitted on a J-map. In those cases where the low elongation observations of a CME on a J-map do not agree well with a model trace the expected arrival time differed significantly from the observed arrival time. Possible reasons for this difference are observations of an extended source or an accelerating source at low elongations. Future work should examine with the aid of coronagraphs what is occurring in this low elongation region to establish if CMEs are still accelerating or if this is a consequence of the CME morphology and density variation.

7. Conclusions and Future Work

This thesis has examined the appearance of transient features of the solar wind in the field of view provided by the STEREO/HI instruments and assessed the efficacy of the technique to extract information about solar wind transients. This thesis has applied the technique to studies of both CIRs and CMEs and the results of those studies is summarised here.

Chapter four examined the contribution of human error in extracting transient tracks from STEREO/HI J-plots and how the visibility of a transient to large elongations affects the results of the fit from the J-plot. We found that, when done with care, the human error in extracting transient tracks can be reduced to a small error compared to the perfect fits. The example in chapter 4 (figure 4.5) shows relatively small errors for velocity, V_r , but much larger potential errors in the direction, β . Using panel d as an example we can see that for an input V_r of 320 km s^{-1} the modelled human error introduces an error of $\pm 25 \text{ km s}^{-1}$ for a 95% certainty level but the input β of 48° produced a much larger range of values for a 95% certainty level from 33° to 70° . Despite this however we can also see that the determined best fits the values are actually very close to the input values. This is a good indication that any human error introduced is minimal and can be accounted for when extracting transient properties from J-maps.

Chapter four also allowed us to make comments on how the visibility of a transient in the STEREO/HI J-maps affects the error in the resulting fit. This is best seen in figures 4.6 and 4.7 which show how the absolute error on velocity and direction respectively vary within a range of velocities and directions and how this error changes

with the visibility of a track. We see that when a transient is seen through the whole of the HI cameras the errors on both velocity and direction are minimised. We can also see though that the errors remain relatively small when the transient is seen out to around 45° elongation but for transients which are seen to elongations of less than 35° the errors quickly start to increase. From this we conclude that to get an accurate estimate of a transient's velocity and direction then the transient should be visible to elongations of 40° or more.

Chapter five studied the propagation of CIRs through the inner heliosphere using a variety of spacecraft situated at various points to compare expected arrival times with observed arrival times. The expected arrival times were calculated using the observed velocity and arrival time at the ACE spacecraft and the observed velocity calculated from observations of small scale transients observed within a CIR front by the STEREO/HI cameras. From the in-situ observations of the arrival of CIRs at Venus, Mars and the two STEREO spacecraft we came to the conclusion that using the in-situ observations from ACE was more reliable than using STEREO/HI observations. However, we also concluded that at times it would be necessary to use either the STEREO/HI observations or in-situ observations from STEREO if we were interested in the arrival of a CIR at a particular body. Future work should focus on improving the estimates from the STEREO/HI observations perhaps with the use of the coronagraphs on the STEREO spacecraft.

Chapter six showed the technique described in chapter four applied to several CMEs seen in both STEREO spacecraft and we used this technique to compare expected arrival times from STEREO/HI observations to the observed arrival times at ACE. We generally found good agreement between the expected arrival times from STEREO/HI and the observed arrival time at ACE. The best agreements were generally when

STEREO/HI observations of tracks from elongations close to the sun were easily distinguishable from other tracks. It is often the case that close to the sun there is a lot of visible activity which can make identification of CME tracks difficult. Using the actual observations from STEREO/HI can aid in determining the correct track. However there are still CMEs which produce a poor match between the expected and observed arrival time even when the track is clear and the track can be accurately identified. Suspected reasons for this are either acceleration occurring within the field of view of the STEREO/HI cameras, or an extended source region being visible. Future work should aim to identify if either of these is a case for these CMEs or other transient events and if they are causing a poor match then the size of these effects should be investigated.

Future work using this technique could focus on further testing of the assumptions particularly the assumption of constant speed. The work in chapters five and six suggest the possibility of acceleration still occurring at a significant rate at low elongations. By focusing on this region and with the aid of in-situ observations a clearer understanding of any acceleration occurring in the HI field of view should arise. This acceleration should be investigated independently for CIRs and CMEs.

Future studies of CIRs should focus on the small scale transients observed in STEREO/HI and their role within CIRs as a whole. The formation of CIRs suggests that these small scale transients could experience a significant pressure force from the fast solar wind stream on the trailing edge of a CIR. If this is the case then we might expect to see some extended acceleration for small scale transients and where we see multiple transients will we then see the same acceleration applied to all transients or will the fast solar wind stream apply a different force to each transient?

This thesis has not used the stereoscopic capabilities of the STEREO mission to investigate solar wind transients although chapter six does use observations from both STEREO spacecraft, but they are not combined to produce 3-D images. Here we use the two spacecraft to improve the analysis of events compared with observations from a single spacecraft. As previously mentioned STEREO B has a limited use when studying the small scale transients associated with a CIR. However when studying larger one-off events such as CMEs then the twin spacecraft allow for estimates of the extent of the CME. Future studies could use this dual viewpoint to examine the apparent extent of events and compare the extent with associated active regions on the solar surface.

From the work presented in this thesis I conclude that the technique can be used in studies of CMEs and CIRs under certain conditions. In the case of CMEs the technique works very well when a clear set of tracks is visible in the J-maps and is visible to elongations of around 40° . For CIRs the value of the technique lies in the tracking of small scale transients within a CIR. This gives multiple estimates of the speed and direction relative to the observer which can be combined with the observed time of each track and the solar rotation rate to constrain arrival times at Earth or other planetary bodies. The CIR observations are best done with STEREO A where the tracks of multiple small scale transients converge and thus are more easily observed; this is not the case for observations from STEREO B where the tracks will diverge.

Bibliography

Acuña, M.H., Curtis, D., Scheifele, J.L., Russell, C.T., Schroeder, P., Szabo, A. and Juhmann, J.G. (2008) 'The STEREO/IMPACT magnetic field experiment', *Space Science Reviews*, **136**, (1-4), 203-226.

Andrews, M.D. and Howard, R.A. (2001) 'A two-type classification of LASCO coronal mass ejection', *Space Science Reviews*, **95**, 147-163.

Aschwanden, M.J. (2005) *Physics of the Solar Corona*, Chichester: Praxis.

Baker, D., Rouillard, A.P., van Driel-gesztelyi, L., Demoulin, P., Harra, L.K., Lavraud, B. and Davies, J.A. (2009) 'Signatures of interchange reconnection: STEREO, ACE and Hinode observations combined', *Annales Geophysicae*, **27**, 3883-3897.

Bale, S.D., Ullrich, R., Goetz, K., Alster, N., Cecconi, B., Dekkali, M. and Lingner, N.R. (2008) 'The electric antennas for the STEREO/WAVES experiment', *Space Science Reviews*, **136**, (1-4), 529-547.

Barabash, S., Lundin, R., Andersson, H., Brinkfeldt, K., Grigoriev, A., Gunell, H., Holmstrom, M., Yamauchi, M., Asamura, K., Bochsler, P., Wurz, P., Ceruli-Irelli, R., Mura, A., Milillo, A., Maggi, M., Orsini, S., Coates, A.J., Linder, D.R., Kataria, D.O., Curtis, C.C. et al. (2006) 'The analyzer of space plasmas and energetic atoms (ASPERA-3) for the Mars Express mission', *Space Science Reviews*, **126**, (1-4), 113-164.

Barabash, S., Sauvaud, J.-A., Gunell, H., Andersson, H., Grigoriev, A., Brinkfeldt, K., Holinstroem, M., Lundin, R., Yamauchi, M., Asamura, K., Baumjohann, W., Zhang, T.L., Coates, A.J., Linder, D.R., Kataria, D.O., Curtis, C.C., Hsieh, K.C., Sandel, B.R.,

Fedorov, A., Mazelle, C. et al. (2007) 'The analyzer of space plasmas and energetic atoms (ASPERA-4) for the Venus Express mission', *Planetary and Space Science*, **55**, (12), 1772-1792.

Billings, D.E. (1966) *A guide to the Solar Corona*, London: Academic Press.

Bougeret, J.L., Goetz, K., Kaiser, M.L., Bale, S.D., Kellogg, P.J., Maksimovic, M., Monge, N., Monson, S.J., Astier, P.L., Davy, S., Dekkali, M., Hinze, J.J., Manning, R.E., Aguilar-Rodriguez, E., Bonnin, X., Briand, C., Cairns, I.H., Cattell, C.A., Cecconi, B., Eastwood, J. et al. (2008) 'S/WAVES: The radio and plasma wave investigation on the STEREO mission', *Space Science Reviews*, **136**, (1-4), 487-528.

Brueckner, G., Howard, R., Koomen, M., Korendyke, C., Michels, D., Moses, J., Socker, D., Dere, K., Lamy, P., Llebaria, A., Bout, M., Schwenn, R., Simnett, G., Bedford, D. and Eyles, C. (1995) 'The large angle spectroscopic coronagraph (LASCO)', *Solar Physics*, **162**, (1-2), 357-402.

Bunce, E.J., Cowley, S.W.H., Wright, D.M., Coates, A.J., Dougherty, M.K., Krupp, N., Kurth, W.S. and Rymer, A.M. (2005) 'In situ observations of a solar wind compression-induced hot plasma injection in Saturn's tail', *Geophysical Research Letters*, **32**.

Cecconi, B., Bonnin, X., Hoang, S., Maksimovic, M., Bale, S.D., Bougeret, J.L., Goetz, K., Lecacheux, A., Reiner, M.J., Rucker, H.O. and Zarka, P. (2008) 'STEREO/WAVES goniopolarimetry', *Space Science Reviews*, **136**, (1-4), 549-563.

Chapman, S. (1950) 'Corpuscular influences upon the upper atmosphere', *Journal of Geophysical Research*, **55**, 361.

Chen, F.F. (1974) *Introduction to Plasma Physics and Controlled Fusion*, 2nd edition, New York: Springer.

Cliver, E. (2006) 'The 1859 space weather event: Then and now', *Advances in Space Research*, **38**, (2), 119-129.

Cranmer, S.R. (2002) 'Coronal holes and the high speed solar wind', *Space Science Reviews*, **101**, 229-294.

Cremades, H. and Bothmer, V. (2004) 'On the three-dimensional configuration of coronal mass ejections', *Astronomy and Astrophysics*, **422**, (1), 307-322.

Davies, J.A., Harrison, R.A., Rouillard, A.P., Sheeley, N.R., Perry, C.H., Bewsher, D., Davis, C.J., Eyles, C.J., Crothers, S.R. and Brown, D.S. (2009) 'A synoptic view of the solar transient evolution in the inner heliosphere using the Heliospheric Imagers on STEREO', *Geophysical Research Letters*, **36**.

Davis, C.J., Davies, J.A., Lockwood, M., Rouillard, A.P., Eyles, C.J. and Harrison, R.A. (2009) 'Stereoscopic imaging of an Earth-impacting solar coronal mass ejection: A major milestone for the STEREO mission', *Geophysical Research Letters*, **36**, L08102.

Davis, C.J., Kennedy, J. and Davies, J.A. (2010) 'Assessing the accuracy of CME speed and trajectory estimates from STEREO observations through a comparison of independent methods', *Solar Physics*, **163**, (1-2), 209-222.

de Koning, C.A., Pizzo, V.J. and Biesecker, D.A. (2009) 'Geometric localization of CMEs in 3d space using the STEREO beacon data: First results', *Solar Physics*, **256**, 167-18.

Dorrian, G.D., Breen, A.R., Davies, J.A., Rouillard, A.P., Fallows, R.A., Whittaker, I.C., Brown, D.S., Harrison, R.A., Davis, C.J. and Grande, M. (2010) 'Transient Structures and Stream Interaction Regions in the Solar Wind: Results from EISCAT

Interplanetary Scintillation, STEREO HI and Venus Express ASPERA-4

Measurements', *Solar Physics*, **265**, 207-231.

Driesman, A., Hynes, S. and Cancro, G. (2008) 'The STEREO observatory', *Space Science Reviews*, **136**, (1-4), 17-44.

Edberg, N.J.T., Nilsson, H., Williams, A.O., Lester, M., Milan, S.E., Cowley, S.W.H., Franz, M., Barabash, S. and Futaana, Y. (2010) 'Pumping out the atmosphere of Mars through solar wind pressure pulses', *Geophysical Research Letters*, **37**, (L03107).

Eyles, C.J., Harrison, R.A., Davis, C.J., Waltham, N.R., Shaughnessy, B.M., Mapson-Menard, H.C., Bewsher, D., Crothers, S.R., Davies, J.A., Simnett, G.M., Howard, R.A., Moses, J.D., Newmark, J.S., Socker, D.G., Halain, J., Defise, J., Mazy, E. and Rochis, P. (2009) 'The Heliospheric Imagers Onboard the STEREO Mission', *Solar Physics*, **254**, (2), 387-445.

Eyles, C.J., Simnett, G.M., Cooke, M.P., Jackson, B.V., Buffington, A., Hick, P.P., Waltham, N.R., King, J.M., Anderson, P.A. and Holladay, P.E. (2003) 'The solar mass ejection imager (SMEI)', *Solar Physics*, **217**, (2), 319-347.

Feynman, J. (1997) 'Evolving magnetic structures and their relation to coronal mass ejections', in Crooker, N., Joselyn, J.A. and Feynman, J. (ed.) *Coronal Mass Ejections*, Washington: AGU.

Forbes, T.G. (2000) 'A review on the genesis of coronal mass ejections', *Journal of Geophysical Research*, **105**, (A10), 23153-23165.

Galvin, A.B. (1997) 'Minor Ion Composition in CME-related Solar Wind', in Crooker, N., Joselyn, J.A. and Feynman, J. (ed.) *Coronal Mass Ejections*, Washington: AGU.

Galvin, A.B., Kistler, L.M., Popecki, M.A., Farrugia, C.J., Simunac, K.D.C., Ellis, L., Moebius, E., Lee, M.A., Boehm, M., Carroll, J., Cranshaw, A., Conti, M., Demaine, P., Ellis, S., Gaidos, J.A., Googins, J., Granoff, M., Gustafson, A., Heirtzler, D., King, B. et al. (2008) 'The plasma and suprathermal ion composition (PLASTIC) investigation on the STEREO observatories', *Space Science Reviews*, **136**, (1-4), 437-486.

Gonzalez, W.D., Joselyn, J.A., Kamide, Y., Kroehl, H.W., Rostoker, G., Tsurutani, B.T. and Vayliunas, V.M. (1994) 'What is a geomagnetic storm?', *Journal of Geophysical Research*, **99**, (A4), 5771-5792.

Gonzalez, W.D., Tsurutani, B.T. and De Gonzalez, A.L.C. (1999) 'Interplanetary origin of geomagnetic storms', *Space Science Reviews*, **88**, 529-562.

Gopalswamy, N., Lara, A., Lepping, R.P., Kaiser, M.L., Berdichevsky, D. and St Cyr, O.C. (2000) 'Interplanetary acceleration of coronal mass ejections', *Geophysical Research Letters*, **27**, 145-148.

Gosling, J.T. (1997) 'Coronal Mass Ejections: An Overview', in Crooker, N., Joselyn, J.A. and Feynmann, J. (ed.) *Coronal Mass Ejections*, Washington: AGU.

Gosling, J.T., Asbridge, J.R., Bame, S.J. and Feldman, W.C. (1978) 'Solar Wind Stream Interfaces', *Journal of Geophysical Research*, **83**, (A4), 1401-1412.

Gosling, J.T., Hildner, E., MacQueen, R.M., Munro, R.H., Poland, A.I. and Ross, C.L. (1974) 'Mass Ejections from the Sun: A view from Skylab', *Journal of Geophysical Research*, **78**, 2001.

Gosling, J.T. and Pizzo, V.J. (1999) 'Formation and evolution of corotating interaction regions and their three dimensional structure', *Space Science Reviews*, **89**, 21-52.

Hale, G.E. (1931) 'The spectrohelioscope and its work, Part III. Solar eruptions and their apparent terrestrial effects', *Astrophysical Journal*, **73**, 379.

Hanlon, P.G., Dougherty, M.K., Krupp, N., Hansen, K.C., Crary, F.J., Young, D.T. and Toth, G. (2004) 'Dual spacecraft observations of a compression event within the Jovian magnetosphere: Signatures of externally triggered supercorotation?', *Journal of Geophysical Research - Space Physics*, **109**, (A9), A09S09.

Harrison, R.A., Davis, C.J., Eyles, C.J., Bewsher, D., Crothers, S.R., Davies, J.A., Howard, R.A., Moses, D.J., Socker, D.G., Newmark, J.S., Halian, J.-P., Defise, J.-M., Mazy, E., Rochus, P., Webb, D.F. and Simnett, G.M. (2008) 'First imaging of coronal mass ejections in the heliosphere viewed from outside the Sun-Earth line', *Solar Physics*, **247**, 171-193.

Howard, R.A., Brueckner, G.E., St. Cyr, O.C., Biesecker, D.A., Dere, K.P., Koomen, M.J., Korendyke, C.M., Lamy, P.L., Llebaria, A., Bout, M.V., Michels, D.J., Moses, J.D., Paswaters, S.E., Plunkett, S.P., Schwenn, R., Simnett, G.M., Socker, D.G., Tappin, S.J. and Wang, D. (1997) 'Observations of CMEs from SOHO/LASCO', in Crooker, N., Joselyn, J.A. and Feynman, J. (ed.) *Coronal Mass Ejections*, Washington: AGU.

Howard, R.A., Moses, J.D., Vourlidas, A., Newmark, J.S., Socker, D.G., Plunkett, S.P., Korendyke, C.M., Cook, J.W., Hurley, A., Davila, J.M., Thompson, W.T., St Cyr, O.C., Mentzell, E., Mehalick, K., Lemen, J.R., Wuelser, J.P., Duncan, D.W., Tarbell, T.D., Wolfson, C.J., Moore, A. et al. (2008) 'Sun Earth Connection Coronal and Heliospheric Investigation (SECCHI)', *Space Science Reviews*, **136**, (1-4), 67-15.

Hundhausen, A.J. (1972) *Coronal Expansion and Solar Wind*, New York: Springer-Verlag.

- Hundhausen, A.J. (1993) 'Sizes and locations of Coronal Mass Ejections-SMM observations from 1980 and 1984-1989', *Journal of Geophysical Research*, **98**, (A8), 13177-13200.
- Jackman, C.M., Achilleos, N., Bunce, E.J., Cecconi, B., Clarke, J.T., Cowley, S.W.H., Kurth, W.S. and Zarka, P. (2005) 'Interplanetary conditions and magnetospheric dynamics during the Cassini orbit insertion fly-through of Saturn's magnetosphere', *Journal of Geophysical Research*, **110**.
- Jones, R.A., Breen, A.R., Fallows, A.R., Canals, A., Bisi, M.M. and Lawrence, G. (2007) 'Interaction between coronal mass ejections and the solar wind', *Journal of Geophysical Research*, **112**, A08107.
- Kaiser, M.L., Kucera, T.A., Davila, J.M., St. Cyr, O.C., Guhathakurta, M. and Christian, E. (2008) 'The STEREO Mission: An introduction', *Space Science Reviews*, **136**, (1-4), 5-16.
- Krieger, A.S., Timothy, A.F. and Roelof, E.C. (1973) 'A coronal hole and its identification as the source of a high velocity solar wind stream', *Solar Physics*, **29**, (2), 505-525.
- Kulsrud, R.M. (2005) *Plasma Physics for Astrophysics*, Princeton: Princeton University Press.
- Lee, M.A. (2000) 'An analytical theory of the morphology, flows, and shock compressions at corotating interaction regions in the solar wind', *Journal of Geophysical Research*, **105**, (A5), 10491-10500.

- Lin, R.P., Curtis, D.W., Larson, D.E., Luhmann, J.G., McBride, S.E., Maier, M.R., Moreau, T., Tindall, C.S., Turin, P. and Wang, L. (2008) 'The STEREO IMPACT Suprathermal Electron (STE) instrument', *Space Science Reviews*, **136**, (1-4), 241-255.
- Liu, Y., Richardson, J.D. and Belcher, J.W. (2005) 'A statistical study of interplanetary coronal mass ejections from 0.3 to 5.4 AU', *Planetary and Space Science*, **53**, 3-17.
- Lugaz, N., Vourlidas, A., Roussev, I.I. and Morgan, H. (2009) 'Solar-Terrestrial simulation in the STEREO era: The 24-25 January eruptions', *Solar Physics*, **256**, (1-2), 269-284.
- Luhmann, J.G. (1997) 'CMEs and space weather', in Crooker, N., Joselyn, J.A. and Feynman, J. (ed.) *Coronal Mass Ejections*, Washington: AGU.
- Luhmann, J.G., Curtis, D.W., Schroeder, P., McCauley, J., Lin, R.P., Larson, D.E., Bale, S.D., Sauvaud, J.-A., Aoustin, C., Mewaldt, R.A., Cummings, A.C., Stone, E.C., Davis, A.J., Cook, W.R., Kecman, B., Wiedenbeck, M.E., von Roseninge, T., Acuna, M.H., Reichenthal, L.S., Shuman, S. et al. (2008a) 'STEREO IMPACT investigation goals, measurements, and data products overview', *Space Science Reviews*, **136**, (1-4), 117-184.
- Luhmann, J.G., Fedorov, A., Barabash, S., Carlsson, E., Futaana, Y., Zhang, T.L., Russell, C.T., Lyon, J.G., Ledvina, S.A. and Brain, D.A. (2008b) 'Venus Express observations of atmospheric oxygen escape during the passage of several coronal mass ejections', *Journal of Geophysical Research - Planets*, **113**.
- Lundin, R., Barabash, S., Fedorov, A., Holmstrom, M., Nilsson, H., Sauvaud, J.-A. and Yamuchi, M. (2008) 'Solar forcing and planetary ion escape from Mars', *Geophysical Research Letters*, **35**.

Maloney, S.A., Gallagher, P.T. and McAteer, R.T.J. (2009) 'Reconstructing the 3-D trajectories of CMEs in the inner heliosphere', *Solar Physics*, **256**, (1-2), 149-166.

Marubashi, K. (1997) 'Interplanetary magnetic flux ropes and solar filaments', in Crooker, N., Joselyn, J.A. and Feynman, J. (ed.) *Coronal mass ejections*, Washington: AGU.

Mason, G.M., Desai, M.I., Mall, U., Korth, A., Bucik, R., von Rosenvinge, T.T. and Simunac, K.D. (2009) 'In situ Observations of CIRs on STEREO, Wind, and ACE During 2007-2008', *Solar Physics*, **256**, 393-408.

Mason, G.M., Korth, A., Walpole, P.H., Desai, M.I., von Rosenvinge, T.T. and Shuman, S.A. (2008) 'The Suprathermal Ion Telescope (SIT) for the IMPACT/SEP investigation', *Space Science Reviews*, **136**, (1-4), 257-284.

McComas, D., Bame, S., Barker, P., Feldman, W., Philips, J., Riley, P. and Griffee, J. (1998) 'Solar Wind Electron Proton Alpha Monitor (SWEPAM) for the Advanced Composition Explorer', *Space Science Reviews*, **86**, (1-4), 563-612.

Mewaldt, R.A., Cohen, C.M.S., Cook, W.R., Cummings, A.C., Davis, A.J., Geier, S., Kecman, B., Klemic, J., Labrador, A.W., Leske, R.A., Miyasaka, H., Nguyen, V., Ogliore, R.C., Stone, E.C., Radocinski, R.G., Wiedenbeck, M.E., Hawk, J., Shuman, S., von Rosenvinge, T.T. and Wortman, K. (2008) 'The Low-Energy Telescope (LET) and SEP central electronics for the STEREO mission', *Space Science Reviews*, **136**, (1-4), 285-362.

Michalek, G., Gopalswamy, N. and Yashiro, S. (2009) 'Expansion speed of coronal mass ejections', *Solar Physics*, **260**, 401-406.

- Milan, S.E., Hutchinson, J., Boakes, P.D. and Hubert, B. (2009) 'Influences on the radius of the auroral oval', *Annales Geophysicae*, **27**, (7), 2913-2924.
- Mueller-Mellin, R., Boettcher, S., Falenski, J., Rode, E., Duvet, L., Sanderson, T., Butler, B., Johlander, B. and Smit, H. (2008) 'The Solar Electron and Proton telescope for the STEREO mission', *Space Science Reviews*, **136**, (1-4), 363-389.
- Neugebauer, M. and Goldstein, R. (1997) 'Particle and field signatures of coronal mass ejections in the solar wind', in Crooker, N., Joselyn, J.A. and Feynman, J. (ed.) *Coronal Mass Ejections*, Washington: AGU.
- Noyes, R.W. (1982) *The Sun, Our Star*, London: Harvard University Press.
- Parker, E.N. (1958) 'Dynamics of the interplanetary gas and magnetic fields', *Astrophysical Journal*, **128**, 664-676.
- Parker, E.N. (1963) *Interplanetary Dynamical Processes*, New York: John Wiley.
- Pizzo, V. (1978) 'A Three-Dimensional Model of Corotating Streams in the Solar Wind 1. Theoretical Foundations', *Journal of Geophysical Research*, **83**, 5563-5572.
- Richardson, I.G. and Cane, H.V. (1995) 'Regions of abnormally low proton temperature in the solar wind (1965-1991) and their association with ejecta', *Journal of Geophysical Research*, **100**, (A12), 23397-23412.
- Rouillard, A.P., Davies, J.A., Forsyth, R.J., Rees, A., Davis, C.J., Harrison, R.A., Lockwood, M., Bewsher, D., Crothers, S.R., Eyles, C.J., Hapgood, M. and Perry, C.H. (2008) 'First imaging of corotating interaction regions using the STEREO spacecraft', *Geophysical Research Letters*, **35**, (L10110).

Rouillard, A.P., Davies, J.A., Forsyth, R.J., Savani, N.P., Sheeley, N.R., Thernisien, A., Zhang, T.L., Howard, R.A., Anderson, B., Carr, C.M., Tsang, S., Lockwood, M., Davis, C.J., Harrison, R.A., Bewsher, D., Fraenz, M., Crothers, S.R., Eyles, C.J., Brown, D.S., Whittaker, I. et al. (2009b) 'A solar storm observed from the Sun to Venus using the STEREO, Venus Express and MESSENGER spacecraft', *Journal of Geophysical Research*, **114**.

Rouillard, A.P., Davies, J.A., Lavraud, B., Forsyth, R.J., Savani, N.P., Bewsher, D., Brown, D.S., Sheeley, N.R., Davis, C.J., Harrison, R.A., Howard, R.A., Vourlidas, A., Lockwood, M., Crothers, S.R. and Eyles, C.J. (2010a) 'Intermittent release of transients in the slow solar wind: 1. Remote sensing observations', *Journal of Geophysical Research*, **115**, (A04103).

Rouillard, A.P., Lavraud, B., Davies, J.A., Savani, N.P., Burlaga, L.F., Forsyth, R.J., Sauvaud, J.A., Opitz, A., Lockwood, M., Luhmann, J.G., Simunac, K.D.C., Galvin, A.B., Davis, C.J. and Harrison, R.A. (2010b) 'Intermittent release of small-scale transients in the slow solar wind: 2. In-situ evidence', *Journal of Geophysical Research*, **115**, (A04104).

Rouillard, A.P., Lavraud, B., Sheeley, N.R., Davies, J.A., Burlaga, L.F., Savani, N.P., Jacquy, C. and Forsyth, R.F. (2010c) 'White light and in situ comparison of a formed merged interaction region', *The Astrophysical Journal*, **719**, 1385-1392.

Rouillard, A.P., Savani, N.P., Davies, J.A., Lavraud, B., Forsyth, R.J., Morley, S.K., Opitz, A., Sheeley, N.R., Burlaga, L.F., Sauvaud, J.A., Simunac, K.D.C., Luhmann, J.G., Galvin, A.B., Crothers, S.R., Davis, C.J., Harrison, R.A., Lockwood, M., Eyles, C.J., Bewsher, D. and Brown, D.S. (2009a) 'A multispacecraft analysis of a small-scale transient entrained by solar wind streams', *Solar Physics*, **356**, 307-326.

Russell, C.T. (2001) 'Solar Wind and Interplanetary Magnetic Field: A Tutorial', in Song, P., Singer, H.J. and Siscoe, G.L. *Space Weather*, Washington, DC: American Geophysical Union.

Sanderson, T.R., Lin, R.P., Larson, D.E., McCarthy, M.P., Parks, G.K., Bosqued, J.M., Lormant, N., Ogilvie, K., Lepping, R.P., Szabo, A., Lazarus, A.J., Steinberg, J.T. and Hoeksema, J.T. (1998) 'Wind observations of the influence of the Sun's magnetic field on the interplanetary medium at 1 AU', *Journal of Geophysical Research*, **103**, (A8), 17235-17247.

Sauvaud, J.A., Larson, D., Aoustin, C., Curtis, D., Medale, J.L., Fedorov, A., Rouzaud, J., Luhmann, J., Moreau, T., Schroeder, P., Louarn, P., Dandouras, I. and Penou, E. (2008) 'The IMPACT solar wind electron analyzer (SWEA)', *Space Science Reviews*, **136**, (1-4), 227-239.

Savani, N.P., Rouillard, A.P., Davies, J.A., Owens, M.J., Forsyth, R.J., Davis, C.J. and Harrison, R.A. (2009) 'The radial width of a coronal mass ejection between 0.1 and 0.4 AU estimated from the Heliospheric Imager on STEREO', *Annales Geophysicae*, **27**, 4349-4358.

Schwenn, R. and Marsch, E. (1990) *Physics of the inner heliosphere*, Berlin: Springer.

Sheeley, N.R., Herbst, A.D., Palatchi, C.A., Wang, Y.M., Howard, R.A., Moses, J.D., Vourlidas, A., Newmark, J.S., Socker, D.G., Plunkett, S.P., Korendyke, C.M., Burlaga, L.F., Davila, J.M., Thompson, W.T., St Cyr, O.C., Harrison, R.A., Davis, C.J., Eyles, C.J., Halain, J.P., Wang, D. et al. (2008b) 'SECCHI observations of the Sun's garden-hose density spiral', *The Astrophysical Journal*, **674**, L109-L112.

Sheeley, N.R., Herbst, A.D., Palatchi, C.A., Wang, Y.M., Howard, R.A., Moses, J.D., Vourlidas, A., Newmark, J.S., Socker, D.G., Plunkett, S.P., Korendyke, C.M., Burlaga, L.F., Davila, J.M., Thompson, W.T., St Cyr, O.C., Harrison, R.A., Davis, C.J., Eyles, C.J., Halain, J.P., Wang, D. et al. (2008a) 'Heliospheric images of the solar wind at Earth', *The Astrophysical Journal*, **675**, 853-862.

Sheeley, N.R. and Rouillard, A.P. (2010) 'Tracking streamer blobs into the heliosphere', *The Astrophysical Journal*, **715**, 300-309.

Sheeley, N.R., Walters, J.H., Wang, Y.-M. and Howard, R.A. (1999) 'Continuous tracking of coronal outflows: two kinds of coronal mass ejections', *Journal of Geophysical Research*, **104**, (A11), 24739-24767.

Simunac, K.D.C., Kistler, L.M., Galvin, A.B., Popecki, M.A. and Farrugia, C.J. (2009) 'In situ observations from STEREO/PLASTIC: a test for L5 space weather monitors', *Annales Geophysicae*, **27**, 3805-3809.

Smith, C., L'Heureux, J., Ness, N., Acuna, M., Burlaga, L. and Scheifele, J. (1998) 'The ACE magnetic fields experiment', *Space Science Reviews*, **86**, (1-4), 613-632.

Socker, D., Howard, R., Korendyke, C., Simnett, G. and Webb, D. (2000) 'The NASA Solar Terrestrial Relations Observatory (STEREO) mission Heliospheric Imager', *Instrumentation for UV/EUV Astronomy and Solar Missions, Proceedings of the Society of Photo-Optical Instrumentation Engineers (SPIE)*, San Diego, 284-293.

Stix, M. (1989) *The Sun*, 2nd edition, Berlin: Springer.

Tappin, S.J. (2006) 'The deceleration of an interplanetary transient from the sun to 5 AU', *Solar Physics*, **233**, 233-248.

- Tappin, S.J. and Howard, T.A. (2009) 'Direct observation of a corotating interaction region by three spacecraft', *The Astrophysical Journal*, **702**, (2), 862-870.
- Thernisien, A., Vourlidas, A. and Howard, R.A. (2009) 'Forward Modeling of Coronal Mass Ejections using STEREO/SECCHI data', *Solar Physics*, **256**, 111-130.
- Vennerstrom, S., Olson, N., Purucker, M., Acuna, M. and Cain, J. (2003) 'The magnetic field in the pile-up region at Mars, and its variation with the solar wind', *Geophysical Research Letters*, **30**, (7).
- von Rosenvinge, T.T., Reames, D.V., Baker, R., Hawk, J., Nolan, J.T., Ryan, L., Shuman, S., Wortman, K.A., Mewaldt, R.A., Cummings, A.C., Cook, W.R., Labrador, A.W., Leske, R.A. and Wiedenbeck, M.E. (2008) 'The High Energy Telescope for STEREO', *Space Science Reviews*, **136**, (1-4), 391-435.
- Vourlidas, A. and Howard, R.A. (2006) 'The proper treatment of coronal mass ejection brightness: A new methodology and implications for observations', *Astrophysical Journal*, **642**, (2), 1216-1221.
- Wang, C., Du, D. and Richardson, J.D. (2005) 'Characteristics of the interplanetary coronal mass ejections between 0.3 and 5.4 AU', *Journal of Geophysical Research*, **110**, A10107.
- Webb, D.F., Howard, T.A., Fry, C.D., Kuchar, T.A., Odstrcil, D., Jackson, B.V., Bisi, M.M., Harrison, R.A., Morrill, J.S., Howard, R.A. and Johnstone, J.C. (2009) 'Study of CME propagation in the inner heliosphere: SOHO LASCO, SMEI and STEREO HI observations of the January 2007 events', *Solar Physics*, **256**, (1-2), 239-267.

Whittaker, I.C., Dorrian, G.D., Breen, A., Grande, M. and Barabash, S. (2010) 'In-situ Observations of a Co-rotating Interaction Region at Venus Identified by IPS and STEREO', *Solar Physics*, **265**, 197-206.

Wood, B.E., Howard, R.A., Plunkett, S.P. and Socker, D.G. (2009) 'Comprehensive observations of a solar minimum coronal mass ejection with the Solar Terrestrial Relations Observatory', *The Astrophysical Journal*, **694**, 707-717.

Wood, B.E., Howard, R.A., Thernisien, A. and Socker, D.G. (2010) 'The three-dimensional morphology of a corotating interaction region in the inner heliosphere', *Astrophysical Journal Letters*, **708**, (2), L89-L94.

Zurbuchen, T.H. and Richardson, I.G. (2006) 'In-situ solar wind and magnetic field signatures of interplanetary coronal mass ejections', *Space Science Reviews*, **123**, (1-3), 31-43.